

Anomalous Thermodynamics of
Nonideal Gas Physisorption on
Nanostructured Carbons

Thesis by
Maxwell Robert Murialdo

In Partial Fulfillment of the Requirements for
the degree of
Doctor of Philosophy

The Caltech logo, featuring the word "Caltech" in a bold, orange, sans-serif font, centered on a light yellow rectangular background.

CALIFORNIA INSTITUTE OF TECHNOLOGY

Pasadena, California

2017
(Defended July 28, 2016)

© 2017

Maxwell Murialdo
All Rights Reserved

ACKNOWLEDGEMENTS

I am blessed to have been surrounded by the most wonderful people who have guided, supported and generally made this work possible. My advisor, Prof. Brent Fultz, has been a brilliant source of guidance through my years at Caltech and I hold in high esteem his piercing insight and penchant for navigating the obstacles of fundamental science. Dr. Nicholas Stadie has served as a great mentor with dedicated enthusiasm and a wealth of knowledge both hands-on and theoretical. I would like to thank the entire Fultz Group (Dr. David Abrecht, Dr. Channing Ahn, Dr. David Boyd, Dr. Olle Hellman, Dr. Tian Lan, Dr. Jiao Lin, Dr. Lisa Mauger, Dr. Jorge Muñoz, Dr. Hillary Smith, Dr. Hongjin Tan, Dr. Sally Tracy, Dr. Heng Yang, Bryce Edwards, Jane Herriman, Dennis Kim, Claire Saunders, Yang Shen, Xiao Tong, Nick Weadock, and Fred Yang along with summer students Christopher Gardner and Jun-Ren Chen) for their help, guidance, ideas, conversations, and general support. This work would also not have been possible without the generous support of the Energy Frontier Research Center in Extreme Environments (EFree) and the dedication of Dr. Russell Hemley and Dr. Stephen Gramsch. EFree has provided a number of opportunities for collaborations and I am grateful for the contributions of my inter-institutional collaborators (Prof. John Badding, Prof. Nasim Alem, Stephen Juhl, Prof. Kai Landskron and Yiqun Liu). A special thanks to my thesis committee members (Prof. Marco Bernardi, Prof. Katherine Faber, Prof. William Goddard III, and Prof. William Johnson) for their guidance both inside and outside of the classroom. Finally I would like to thank my wonderful family and friends for their endless encouragement and understanding.

ABSTRACT

Mesoporous and microporous adsorbents play critical roles in gas storage and separation applications. This thesis describes previously unexplored anomalous thermodynamics in the field of gas physisorption and their impact on energy relevant gases including methane, ethane, krypton and carbon dioxide. Physisorption occurs when an adsorbent induces gas molecules to form a locally densified layer at its surface due to physical interactions. This increases gas storage capacity over pure compression and its efficacy is dependent on the surface area of the adsorbent and the isosteric heat of adsorption. The isosteric heat of adsorption is the molar change in the enthalpy of the adsorptive species upon adsorption and serves as a measure of adsorbent-adsorbate binding strength.

Unlike conventional adsorbate-adsorbent systems, which have isosteric heats of adsorption that decrease with surface loading, zeolite-templated carbon is shown to have isosteric heats of methane, ethane and krypton adsorption that increase with surface loading. This is a largely beneficial effect that can enhance gas storage and separation. The unique nanostructure and uniform pore periodicity of the zeolite-templated carbon promote lateral interactions among the adsorbed molecules that cause the isosteric heats of adsorption to increase with loading. These results have been tested and corroborated by developing robust fitting techniques and thermodynamics analyses. The anomalous thermodynamics are shown to result from cooperative adsorbate-adsorbate interactions among the nonideal species and are modeled with an Ising-type model.

As a second theme of this thesis, the study of nonideal gas adsorption has enabled the development of a Generalized Law of Corresponding States for Physisorption. A predictive understanding of high-pressure physisorption on a variety of adsorbents would facilitate the

further development of tailored adsorbents and adsorption analysis. Prior attempts at developing a predictive understanding, however, have been hindered by nonideal gas effects.

By approaching physisorption from both empirical and fundamental perspectives, a Generalized Law of Corresponding States for Physisorption was established that accounts for a number of nonideal effects. This new Law of Corresponding States allows one to predict adsorption isotherms for a variety of classical gases from data measured with a single gas. In brief:

“At corresponding conditions on the same adsorbent, classical gases physisorb to the same fractional occupancy.”

Corresponding conditions are met when the reduced variables of each nonideal gas are equivalent, and fractional occupancy gives the fraction of occupied adsorption sites. This Law of Corresponding States for Physisorption is determined using monolayer, BET and Dubinin-Polanyi adsorption theories along with measured adsorption isotherms across a number of conditions and adsorbents. Furthermore, the anomalous cooperative adsorbate-adsorbate interactions discussed in this thesis are shown to be consistent with the Generalized Law of Corresponding States for Physisorption.

PUBLISHED CONTENT AND CONTRIBUTIONS

1. M. Murialdo, N.P. Stadie, C.C. Ahn, and B. Fultz, "A Generalized Law of Corresponding States for the Physisorption of Classical Gases with Cooperative Adsorbate-Adsorbate Interactions," *J. Phys. Chem. C*, 120, 11847 (2016).

DOI: 10.1021/acs.jpcc.6b00289

<http://pubs.acs.org/doi/abs/10.1021/acs.jpcc.6b00289>

M. M. participated in the data collection, analysis, conceptualization and writing of the manuscript.

2. N.P. Stadie, M. Murialdo, C.C. Ahn, and B. Fultz, "Unusual Entropy of Adsorbed Methane on Zeolite-Templated Carbon," *J. Phys. Chem. C*, 119, 26409 (2015).

DOI: 10.1021/acs.jpcc.5b05021

<http://pubs.acs.org/doi/abs/10.1021/acs.jpcc.5b05021?journalCode=jpccck>

M. M. participated in the data collection, analysis, conceptualization and writing of the manuscript.

3. M. Murialdo, N.P. Stadie, C.C. Ahn, and B. Fultz, "Krypton Adsorption on Zeolite-Templated Carbon and Anomalous Surface Thermodynamics," *Langmuir*, 31, 7991 (2015).

DOI: 10.1021/acs.langmuir.5b01497

<http://pubs.acs.org/doi/abs/10.1021/acs.langmuir.5b01497>

M. M. participated in the data collection, analysis, conceptualization and writing of the manuscript.

4. M. Murialdo, N.P. Stadie, C.C. Ahn, and B. Fultz, "Observation and Investigation of Increasing Isothermic Heat of Adsorption of Ethane on Zeolite-Templated Carbon," *J. Phys. Chem. C*, 119, 994 (2015).

DOI: 10.1021/jp510991y

<http://pubs.acs.org/doi/abs/10.1021/jp510991y>

M. M. participated in the data collection, analysis, conceptualization and writing of the manuscript.

5. N.P. Stadie, M. Murialdo, C.C. Ahn, and B. Fultz, "Anomalous Isothermic Enthalpy of Adsorption of Methane on Zeolite-Templated Carbon," *J. Am. Chem. Soc.* 135, 990 (2013).

DOI: 10.1021/ja311415m

<http://pubs.acs.org/doi/abs/10.1021/ja311415m>

M. M. participated in the data collection, analysis, conceptualization and writing of the manuscript.

6. M. Murialdo, C.C. Ahn, and B. Fultz, "A Thermodynamic Investigation of Adsorbate-Adsorbate Interactions of Carbon Dioxide on Nanostructured Carbons," *AIChE J.* (submitted, 2016).

M. M. participated in the data collection, analysis, conceptualization and writing of the manuscript.

TABLE OF CONTENTS

| | |
|--|------|
| Acknowledgements..... | iii |
| Abstract | iv |
| Published Content and Contributions..... | vi |
| Table of Contents..... | vii |
| Nomenclature..... | viii |
| Chapter I: An Introduction to Adsorption | 1 |
| Chapter II: Fundamentals of Adsorption..... | 14 |
| Chapter III: Experimental Methods and Analysis..... | 28 |
| Chapter IV: Materials | 38 |
| Chapter V: Methane on Microporous Carbons | 46 |
| Chapter VI: Observation and Investigation of Increasing Isothermic Heat | |
| Of Adsorption of Ethane on Zeolite-Templated Carbon..... | 59 |
| Chapter VII: Krypton Adsorption on Zeolite-Templated Carbon And Anomalous Surface Thermodynamics | 84 |
| Chapter VIII: A Generalized Law of Corresponding States for the Physisorption of Classical Gases with Cooperative Adsorbate-Adsorbate Interactions | 111 |
| Chapter VIII: Supporting Information..... | 137 |
| Chapter IX: A Thermodynamic Study of Carbon Dioxide Adsorption On Nanostructured Carbons at High Pressures | 158 |
| Conclusions..... | 183 |

NOMENCLATURE

Adsorption. The densification of molecules near an interface due to favorable interactions.

Physisorption. Adsorption resulting from physical (not chemical) interactions.

Adsorbent. Solid surface providing the adsorption interface.

Adsorbate. Molecules that have been adsorbed.

Absolute Adsorption (n_a). A measure of all of the molecules in the adsorbed phase.

Excess Adsorption (n_e). A measure of the molecules in the adsorbed phase in excess of the gas-phase density.

Isotherm. Measured adsorption at a series of pressures and a constant temperature.

Isosteric Enthalpy of Adsorption (ΔH_{ads}). The difference between the adsorbed-phase and gas-phase enthalpy at constant coverage conditions.

Isosteric Heat of Adsorption (q_{st}). The positive value of the isosteric enthalpy of adsorption.

Isosteric Entropy of Adsorption (ΔS_{ads}). The difference between the adsorbed-phase and gas-phase entropy at constant coverage conditions.

Adsorbed-Phase Enthalpy (H_a). The molar enthalpy of the molecules in the adsorbed phase.

Adsorbed-Phase Entropy (S_a). The molar entropy of the molecules in the adsorbed phase.

Adsorbed-Phase Heat Capacity at Constant Pressure (C_p). The constant-pressure heat capacity of the molecules in the adsorbed phase.

Gas-Phase Enthalpy (H_g). The molar enthalpy of the molecules in the gas phase.

Gas-Phase Entropy (S_g). The molar entropy of the molecules in the gas phase.

Chapter 1

An Introduction to Adsorption

1. Overview

Recently, after I finished a talk on the thermodynamics of adsorption, an audience member stood up with a critical comment. “But adsorption has been studied for over a hundred years.” Yes, exactly!

Serious studies of adsorption have been ongoing for over a hundred years now. Qualitative knowledge of adsorption goes back thousands of years. This is not to the detriment of the field. Rather it is a testament to the broad utility of adsorption and the complexity of trying to understand such a diverse array of phenomena.

Adsorption is the densification of a fluid at an interface. The nature of the interface may be solid-liquid, gas-liquid, liquid-liquid or solid-gas. In this work we focus on adsorption between a solid “adsorbent” and a gaseous “adsorptive species” which is denoted the “adsorbate” in the adsorbed phase. Adsorption is strictly an interfacial phenomenon, unlike “absorption” wherein the absorptive species penetrates the absorbent. Each molecule in the adsorbed phase actually has less entropy than in the bulk gas phase; however it also has a reduced enthalpy owing to attractive interactions at the interface. This sets up the basic equilibrium of adsorption: a reduction in entropy compared to the gas phase is balanced by a comparable reduction in enthalpy. Adsorption is thus an exothermic process. The favorable interactions at the interface, which enable all adsorption, may be of chemical or physical nature. When chemical bonds occur between the adsorbent and the adsorbate the phenomenon is called chemisorption. When only physical interactions are present (e.g. van der

Waals forces), it is called physisorption. “Sorption” is a more general term used for the ambiguous case. In general, chemisorption results in much stronger adsorbent-adsorbate interactions and is effective at higher temperatures, but requires specific adsorbate-adsorbent systems and is less reversible. In this work we focus on physisorptive systems.

2. Pores

The uses of physisorption are extremely diverse, the most primary of which is the characterization of the adsorbents themselves. Solid-gas physisorption may occur on any solid, but as an interfacial phenomenon, physisorption is strictly a surface effect. High surface area materials, especially porous materials, therefore lend themselves to adsorptive studies. Often porous materials can only be easily and effectively characterized by physisorption. The pores of a porous material may be broadly lumped into one of three size categories: macropores, mesopores and micropores. Macropores are greater than 50 nanometers in width. Mesopores have widths between 2 and 50 nanometers. Micropores have widths of less than 2 nanometers. Both micropores and mesopores are considered “nanopores”. Pores are typically modeled as either cylinders with unique pore diameters, or slits with unique pore widths. Macropores, mesopores and micropores each physisorb gases in distinct ways and require different modeling.

In macropores the pore walls are sufficiently well separated to have non-overlapping effects. This is because physical interactions like van der Waals forces fall off rapidly with distance. Macropores can thus be treated in the same way as a nonporous material, where only a single surface is considered at a time. In macropores, layer-by-layer adsorption is expected and can be effectively modeled using Brunauer, Emmett and Teller (BET) Theory. BET Theory has proven highly successful in determining the surface area of macroporous

adsorbents. Using subcritical adsorption isotherm measurements of nitrogen, argon, carbon dioxide or krypton (for low surface area adsorbents), up to near-saturation pressures, the monolayer coverage can be solved from BET Theory. This quantitative monolayer coverage is in turn correlated with a specific surface area based on the size of the adsorbate molecule. One caveat is that different results may be obtained with different gases (probe molecules) as different pores and topologies are accessible to different size probe molecules.

Mesopores may be treated in much the same way as macropores, with the additional complication of capillary condensation. In appropriately sized mesopores, surface tension (through capillary action) can cause the adsorptive species to condense into a liquid phase in the mesopores at pressures below the bulk saturation pressure. This phenomenon is unique to mesopores as macropores are too large and micropores are too small. Capillary condensation results in hysteresis between the adsorption and desorption isotherms. However, the presence of capillary condensation can be used to obtain information about the pore-size distribution via the Kelvin Equation and variants.

Micropores are of similar dimensions to the gases adsorbed. Within micropores, opposite pore walls often exhibit overlapping potentials. Thus micropores are more accurately treated with a pore-filling model than a layer-by-layer model for adsorption. In general the adsorptive species will holistically fill the micropore volume, making metrics of specific micropore volume more important than specific surface area. The micropore volume may be determined empirically with the Dubinin-Radushkevich equation and variants. Moreover, of critical importance, the micropore-size distribution may be obtained semi-empirically via nonlocal density functional theory (NLDFT). As such, physisorption may be used to characterize pores varying in size from 0.35 nanometers to greater than 100 nanometers.

3. Applications

Adsorbents are also widely used in industrial scale processes like catalysis and gas separation. Catalysis is an enabling factor in ~90% of chemical and materials manufacturing worldwide and may employ homogeneous or heterogeneous catalysts.¹ Unlike homogeneous catalysts, heterogeneous catalysts are of a different phase than the underlying reaction. Often porous solids are used as heterogeneous catalysts in conjunction with a liquid or gas phase. The fluid phase is first adsorbed onto the catalyst, followed by dissociation of the fluid, surface diffusion, a surface reaction and finally desorption of the product. Adsorption is thus a prerequisite for most heterogeneous catalysis and a fundamental understanding of the adsorption process is vital. Moreover, as adsorbents typically have large accessible surface areas, they may be used as structural supports that keep catalysts well dispersed to maximize efficacy.

Gas separation and purification is a second key industrial use of adsorption. Separating chemically inert gases or otherwise removing gaseous impurities is often done by cryogenic distillation. For gases with similar boiling points this process can be both expensive and energy intensive. Gas separation using physisorption offers an efficient alternative, especially when high levels of purity are not required. In physisorptive separation, gases are flowed through an adsorbent bed where one gas preferentially adsorbs over another, ideally with great selectivity. The adsorbent bed may then be regenerated by reducing the pressure or increasing the temperature to desorb the adsorbate. These cyclic processes are referred to as Pressure Swing Adsorption (PSA) and Temperature Swing Adsorption (TSA), respectively. The selectivity is typically due to differences in the adsorbent-adsorbate physical interactions between each gas and the adsorbent. In some cases steric effects are used to enhance selectivity when the gases

to be separated are of dissimilar size or shape and only small and correctly shaped molecules can penetrate a well-defined pore structure. This is commonly used to dry steam from the cracking process or to dry natural gas using zeolites with well-defined micropore structures. Kinetic separation mechanisms may also be employed in molecular sieves where non-uniform pore size distributions allow different molecules to diffuse at different rates. One common example is the separation of nitrogen from air using molecular sieves. Overall, adsorption offers an efficient means of gas separation, purification and in some cases solvent recovery from both industrial and vented sources.

4. Krypton

In this work we study krypton adsorption in detail as a step towards improving krypton separation from other inert gases. Krypton, the fourth noble gas, is an unreactive monatomic gas that otherwise bears many similarities to methane. The two gases share a similar size (Kr: 3.9 Å, CH₄: 4.0 Å)² and approximately spherical symmetry, as well as similar boiling points (120 K and 112 K, respectively)³ and critical temperatures (209 K and 190 K, respectively). Conveniently, monatomic krypton allows for very simple calculations of thermodynamic properties such as entropy, since rotational and internal vibrational modes do not exist. Krypton has applications in the photography, lighting⁴ and medical industries^{5,6}, and is commonly used as an adsorbate for characterizing low-surface-area materials^{7,8}. There is also significant active interest in finding a cost effective and efficient means of separating krypton from xenon derived from nuclear waste^{9,10}.

Nuclear power plants supply over 10% of the world's electricity and are a valuable source of energy in the United States.¹¹ Unfortunately, the United States is already fraught with over 70,000 tons of nuclear waste and no good storage options^{12,13}. One avenue towards

diminishing the amount of nuclear waste generated in the future is to reprocess spent nuclear fuel. Reprocessing entails chopping up and dissolving spent nuclear fuel to recover fissionable remains. These remains can be used to generate additional electricity often exceeding 25% of the initial generation.¹⁴ While the US does not currently reprocess nuclear fuel, reprocessing is typical in Europe, Russia and Japan, and as a member of the International Framework for Nuclear Energy Cooperation, the US has partnered with other countries to improve and develop closed nuclear fuel cycles with reprocessing. During reprocessing, radioactive krypton-85 and nonradioactive xenon are off-gassed. As a radioactive mixture, these gases should be stored as radioactive waste, often in inefficient mole fraction of ~90% nonradioactive xenon to ~10% radioactive krypton-85.¹⁵ While cryogenic distillation is an energy intensive means of separating krypton from xenon, adsorbents offer a potentially efficient alternative. With properly tuned adsorptive separation, less nonradioactive xenon would need to be stored, putting less stress on current nuclear waste storage options.

5. Natural Gas

Another large and quickly growing application of physisorption is for the densified storage of natural gas, particularly within the transportation sector. This is a major focus of this thesis.

Natural gas powers 22% of the world and 33% of the US, and yet its importance is projected to grow.¹⁶ From 2010 to 2013 worldwide natural gas consumption has grown at a rate of 2% annually from 113,858 to 121,357 billion cubic feet.¹⁶ Over the same time, the proven reserves have grown at a rate of 1% annually, up to 6,972.518 trillion cubic feet.¹⁶

Assuming a 2% annual increase in consumption, but no increase in the proven reserves, our current proven reserves will last into the 23rd century, although estimates vary.¹⁶

Natural gas predominantly originates from two naturally occurring processes. Biogenic methane results when methanogenic archaea break organic matter into simple hydrocarbons like methane. These microorganism live in oxygen depleted regions of the earth's crust and in the intestines of most animals. Collecting the gases emanating from manure and landfills has proven a clean and renewable source of natural gas. Nonetheless, to date these operations are small scale and pale in comparison to the scope of thermogenic natural gas collection. Thermogenic methane is synthesized from ancient organic matter under the high temperatures and pressures found deep in the earth's crust. This process takes millions of years and is thus not considered renewable on a human timescale. These natural gas fossil fuels are often discovered alongside oil, although deeper deposits synthesized at higher temperatures tip the balance towards a higher fraction of natural gas synthesis.

Thermogenic methane is also found alongside coal (coalbed gas) or as a methane hydrate (clathrate). Methane hydrates form under temperatures below 15 °C and pressures greater than 19 bar. These conditions are met in offshore continental shelves and the permafrost of Siberia. Recently Japan Oil, Gas and Metals National Cooperation has recovered commercially viable quantities of natural gas from oceanic methane clathrates.¹⁷ This presents a particularly exciting advancement given estimates of vast quantities of oceanic methane hydrates (estimated at 5×10^{15} cubic meters of methane hydrate).¹⁶

Other unconventional sources of natural gas have been studied and commercialized within the past decade. These sources have historically been economically prohibitive, but this is changing with recent technological advancements. The collection of deep gas, tight gas, and

shale gas are on the rise. Shale gas, in particular has boomed from less than 1% of the US natural gas production in 2000 to 39% in 2012.¹⁶ It is estimated that there may be more than a quadrillion cubic feet of unconventional natural gas reserves in the US alone.¹⁶

At present, 15 countries account for 84% of worldwide natural gas production, with Russia, Iran, Qatar, Turkmenistan and the US at the top of the list.¹⁶ Before transportation or use, the natural gas must be purified. Impurities like water, sand and other gases are separated out. Some of the purified gas byproducts like propane, butane and hydrogen sulfide are sold on secondary markets. Landfill methane is prone to have large quantities of carbon dioxide and hydrogen sulfide, which must be removed before transportation to prevent pipeline corrosion. The gas may be further purified to achieve a high quality gas comprised of almost pure methane and known as “dry” natural gas. In the presence of significant quantities of other hydrocarbons, natural gas is deemed “wet”. The main constituent in natural gas is always methane, followed by ethane. The composition varies significantly but is generally in accordance with Table 1.

Table 1. Typical Composition of Natural Gas¹⁸

| gas | mole fraction (%) |
|----------------|-------------------|
| methane | 87-97 |
| ethane | 1.5-7 |
| propane | 0.1-1.5 |
| butane | 0.02-0.6 |
| alkanes #C > 4 | trace |
| nitrogen | 0.2-5.5 |
| carbon dioxide | 0.1-1.0 |
| oxygen | 0.01-0.1 |
| hydrogen | trace |

The transportation and utilization of natural gas has been employed since 500 B.C. when Chinese in the Ziliujing district of Sichuan developed crude natural gas pipelines from bamboo.¹⁹ This natural gas was harnessed to boil seawater. It wasn't until 1785, however, that natural gas first found widespread commercialization as a fuel for streetlamps and homes in England.¹⁹ This natural gas emanated from fissures above naturally occurring pockets. In 1821 William A. Hart drilled the first intentional natural gas well, in Fredonia, New York.¹⁹ Since then the industry has exploded in the US and abroad. An emerging natural gas industry set to explode is for use in the transportation sector. Worldwide tens of millions of natural gas vehicles dot the roads. Ordinary internal combustion engines can be converted to run on natural gas for less than \$10,000 and commercial vehicles designed specifically to run on natural gas are gaining traction. Starting in 2008 with the Honda Civic natural gas, major auto manufacturers have churned out a number of compressed natural gas commercial vehicles including the Chevrolet Silverado 2500, Dodge Ram 2500, Ford F-250 and Chevrolet Savana.

This surge in natural gas cars proffers environmental benefits. For the same amount of energy, thermogenic methane emits 16% less carbon dioxide than diesel.¹⁶ Landfill biogas can emit a net 88% less carbon dioxide than diesel.¹⁶ In power generation, methane power plants emit almost 50% less carbon dioxide than coal-powered plants.¹⁶ The carbon dioxide released per million BTU, for a variety of common fuels, is listed in Table 2. Methane is the cleanest burning hydrocarbon. Additionally, natural gas emits less trace pollutants including carbon monoxide, nitrogen oxides, sulfur oxides and particular matter than other fuels.

Table 2. Pounds of CO₂ Emissions Per MBTU for Common Fuels¹⁶

| fuel | Lbs. CO ₂ /MBTU |
|---------------------------|----------------------------|
| Coal (anthracite) | 228.6 |
| Coal (bituminous) | 205.7 |
| Coal (lignite) | 215.4 |
| Coal (subbituminous) | 214.3 |
| Diesel fuel & heating oil | 161.3 |
| Gasoline | 157.2 |
| Propane | 139 |
| Natural Gas | 117 |

The main hindrance to wide implementation of natural gas in the transportation sector stems from the onboard storage problem. Natural gas has a high gravimetric energy density of 56 MJ kg⁻¹, competitive with other fuel sources, but an abysmally low volumetric energy density of 37 MJ m⁻³ at standard conditions.³ This is a common problem for gaseous fuels with critical temperatures significantly below room temperature. Three potential solutions have been separately implemented in commercial applications: cryogenic liquefaction, high-pressure compression, and compression in the presence of adsorbent materials.

Cryogenic liquefaction requires cooling natural gas to below the critical temperature of methane, which is 190K. This is typically achieved with liquid nitrogen as a coolant in a cryogenic setup. While cryogenic liquefaction can achieve volumetric energy densities as high as 22 GJ m⁻³, it is an energy intensive process and requires expensive equipment and monitoring³. These drawbacks have thus far prevented the widespread adoption of cryogenic liquefaction as a means for natural gas storage on privately owned vehicles.

At high pressures of 700 bar, natural gas has a volumetric energy density of $\sim 17 \text{ GJ m}^{-3}$.³ However, high-pressure compression requires specialized storage tanks. As pressure requirements are increased, the requisite class of storage tank shifts from Type I (all metal, which is the cheapest and currently makes up 93% of the onboard natural gas storage market) to Type IV, all composite with high associated costs.²⁰ Moreover, high pressures limit potential tank designs (as a necessity of eliminating weak points) and potentially pose a significant threat if ruptured intentionally or unintentionally.

The use of adsorbents and moderate compression allows for significant volumetric energy density improvements over pure compression at moderate pressures and temperatures. At low and moderate pressures the favorable interactions between the adsorbent and the adsorbate densify natural gas under equilibrium conditions. Improved natural gas storage is a significant subject of inquiry in this thesis.

Adsorption also serves a number of other niche purposes in areas such as heat pumps and spacecraft environmental controls.²¹ All told, adsorption spans chemistry, biology, physics and engineering and is an integral part of our world. It demands further fundamental scientific inquiry and expertise in adsorbent engineering.

References:

1. Chorkendorff, I.; Niemantsverdriet, J. W. Concepts of Modern Catalysis and Kinetics, 2nd ed.; Wiley: New York, 2007.
2. Cuadros, F.; Cachadina, I.; Ahumada, W. Determination of Lennard-Jones Interaction Parameters Using a New Procedure. *Mol. Eng.* **1996**, *6*, 319-325.
3. Lemmon, E. W.; Huber, M. L.; McLinden, M. O. *NIST Standard Reference Database 23: Reference Fluid Thermodynamic and Transport Properties-REFPROP*, version 8.0; National Institute of Standards and Technology: Gaithersburg, MD, 2007; CD-ROM.
4. Hwang, H. S.; Baik, H. K.; Park, K. W.; Song, K. M.; Lee, S. J. Excitation Energy Transfer of Metastable Krypton Atoms in Kr-He-Xe Low Pressure Glow Discharge for Mercury-Free Lighting. *Jpn. J. Appl. Phys.* **2010**, *49*, 1-3.
5. Chon, D.; Beck, K. C.; Simon, B. A.; Shikata, H.; Saba, O. I.; Hoffman, E. A. Effect of Low-Xenon and Krypton Supplementation on Signal/Noise of Regional CT-based Ventilation Measurements. *J. Appl. Physiol.* **2007**, *102*, 1535-1544.
6. Pavlovskaya, G. E.; Cleveland, Z. I.; Stupic, K. F.; Basaraba, R. J.; Meersmann, T. Hyperpolarized Krypton-83 as a Contrast Agent for Magnetic Resonance Imaging. *Proc. Natl. Acad. Sci. U.S.A.* **2005**, *102*, 18275-18279.
7. Takei, T.; Chikazawa, M. Measurement of Pore Size Distribution of Low-Surface-Area Materials by Krypton Gas Adsorption Method. *J. Ceram. Soc. Jpn.* **1998**, *106*, 353-357.
8. Youssef, A. M.; Bishay, A. F.; Hammad, F. H. Determination of Small Surface-Areas by Krypton Adsorption. *Surf. Technol.* **1979**, *9*, 365-370.
9. Ryan, P.; Farha, O. K.; Broadbelt, L. J.; Snurr, R. Q. Computational Screening of Metal-Organic Frameworks for Xenon/Krypton Separation. *AIChE J.* **2011**, *57*, 1759-1766.
10. Bae, Y.-S.; Hauser, B. G.; Colon, Y. J.; Hupp, J. T.; Farha, O. K.; Snurr, R. Q. High Xenon/Krypton Selectivity in a Metal-Organic Framework with Small Pores and Strong Adsorption Sites. *Microporous Mesoporous Mater.* **2013**, *169*, 176-179.
11. World Statistics: Nuclear Energy Around the World. *Nuclear Energy Institute*. <http://www.nei.org/Knowledge-Center/Nuclear-Statistics/World-Statistics> (accessed 2016).
12. Stop Dithering on Nuclear Waste-Three Decades After Chernobyl, the US Needs to Tackle its Own Ominous Nuclear Safety Problem. *Sci Am.* **2016**, *314*, 10.
13. Stuckless, J. S.; Levich, R. A. The Road to Yucca Mountain-Evolution of Nuclear Waste Disposal in the United States. *Environ. Eng. Geosci.* **2016**, *22*, 1-25.
14. Processing of Used Nuclear Fuel. <http://www.world-nuclear.org/information-library/nuclear-fuel-cycle/fuel-recycling/processing-of-used-nuclear-fuel.aspx> (accessed 2016).
15. Banerjee, D.; Cairns, A. J.; Liu, J.; Motkuri, R. K.; Nune, S. K.; Fernandez, C. A.; Krishna, R.; Strachan, D. M.; Thallapally, P. K. Potential of Metal-Organic Frameworks for Separation of Xenon and Krypton. *Acc. Chem. Res.* **2015**, *48*, 211-219.
16. Independent Statistics and Analysis. *U.S. Energy Information Administration*. <http://www.eia.gov/> (accessed 2016).

17. Tabuchi, H. An Energy Coup for Japan: 'Flammable Ice'. *New York Times*, Mar. 12, 2013, B1.
18. Chemical Composition of Natural Gas. *Union Gas*, <https://www.uniongas.com> (accessed 2016).
19. A Brief History of Natural Gas. *American Public Gas Association*. <http://www.apga.org/> (accessed 2016).
20. LeGault, M., Pressure Vessel Tank Types. *Composites World*. <http://www.compositesworld.com/> (accessed 2016).
21. Dabrowski, A. Adsorption - From Theory to Practice. *Adv. Colloid Interface Sci.* **2001**, *93*, 135-224.

Chapter 2

Fundamentals of Physisorption

1. Background

Early work into determining a universal equation of state for all gases led to the development of the ideal gas law:

$$PV = nRT \quad (1)$$

This law, derived by Emile Clapeyron in 1834, brings together 3 linear gas relationships: Boyle's Law, Charles's Law and Avogadro's Law. The ideal gas law is simple, functional and fairly accurate at dilute conditions. However, at high pressures or low temperatures, the assumptions of the ideal gas law, namely that gases are composed of non-interacting point particles, break down. This shortcoming was addressed later in the 19th century by introducing nonlinear gas equations of state such as the van der Waals equation:

$$\left(P + \frac{n^2 a}{v^2}\right)(v - nb) = nRT \quad (2)$$

Introduced by Johannes Diderick van der Waals in 1873, this equation of state incorporates two gas-dependent parameters, a , and b , which account for the attractive interactions between gas molecules, and the finite volume of real gas molecules, respectively. Johannes van der Waals adamantly believed that gases collided as hard spheres and did not possess any other repulsive interactions. This is now known to be false.

Real gases exhibit both attractive and repulsive interactions that are strongly correlated with intermolecular spacing. For electrically neutral molecules, these forces (e.g. van der Waals) typically fall into one of 4 categories: Keesom Forces, Debye Forces, London Dispersion forces and Pauli repulsive forces. The first three result from some combination of permanent

and/or induced multipole interactions while the Pauli repulsive force is a purely quantum effect.

The sum of the attractive and repulsive intermolecular interactions forms an “interaction potential.” While early on it was generally agreed upon that van der Waals interactions fall off quickly with increasing intermolecular spacing, the precise function was unknown. A number of pair potentials were proposed including the commonly used Lennard-Jones Potential, V_{LJ} :

$$V_{LJ} = 4\varepsilon \left[\left(\frac{\sigma}{r} \right)^{12} - \left(\frac{\sigma}{r} \right)^6 \right] \quad (3)$$

where r is the intermolecular separation and σ and ε are the Lennard-Jones parameters, specific to each gas. The Lennard-Jones potential balances the longer-range attractive interactions (that fall as r^{-6}) with the very short-range Pauli repulsion forces (arbitrarily modeled as falling with r^{-12}). While the r^{-6} dependence derives from the London dispersion force, the r^{-12} repulsive term has no physical basis. Thus while a useful heuristic, the Lennard-Jones potential is not rigorously accurate in describing potentials between two molecules. In physisorption, gas molecules interact with an adsorbent surface, which is generally considered to be much wider than the molecule itself. Patchwise, these interactions may be modeled as between a flat crystalline material and a small molecule, by generalizing the ideas of the Lennard-Jones potential into a new form called the Steele potential¹:

$$\phi(x) = 2\pi\varepsilon_{sf}\rho_s\sigma^2\Delta \left[\frac{2}{5} \left(\frac{\sigma}{r} \right)^{10} - \left(\frac{\sigma}{r} \right)^4 - \left(\frac{\sigma^4}{3\Delta(r+0.61\Delta)^3} \right) \right] \quad (4)$$

where ε_{sf} is the solid-fluid well-depth given by Berthelot mixing rules², ρ_s is the density of the solid, Δ is interplanar spacing of the crystalline material, and σ is a Lennard-Jones type distance parameter determined by Lorentz mixing rules².

In a dynamic view, gases may collide with a solid interface, either elastically or inelastically. Occasionally a gas molecule that collides inelastically will undergo an interaction with the surface, wherein it is briefly localized by the surface potential. This is the essence of physisorption at the microscale. The surface potential may vary over the surface due to impurities, defects, or overall structural features. In microporous materials, the surface potential heterogeneity is largely dictated by the pore-size distribution. Physisorptive systems typically have only shallow (weak) surface potentials that allow adsorbed molecules to explore multiple sites on the two-dimensional potential surface before reentering the gas phase. This is known as a mobile adsorption, as opposed to localized adsorption, which is typically associated with deeper potential wells and chemisorption.

From a fundamental thermodynamics perspective, adsorption compresses a 3-dimensional gas phase into a 2-dimensional adsorbed phase. This presents a significant drop in the molar entropy of the adsorptive species. The difference in molar entropy between the adsorbed and gas phases (at constant coverage) is called the isosteric entropy of adsorption (ΔS_{ads}). The gas-phase entropy (S_g) may be read from data tables. The adsorbed-phase entropy (S_a) depends on a number of factors including coverage.

In order to establish equilibrium, the isosteric entropy of adsorption must be offset by a comparable decrease in molar enthalpy upon adsorption. The difference between the adsorbed-phase enthalpy (H_a) and the gas-phase enthalpy (H_g) (at constant coverage) is called

the isosteric enthalpy of adsorption (ΔH_{ads}). Physisorption is always exothermic, yielding a negative isosteric enthalpy of adsorption. By convention, the isosteric heat of adsorption (q_{st}) is defined as a positive quantity as follows

$$q_{st} \equiv -(H_a - H_g) \quad (5)$$

The isosteric heat of adsorption may be thought of as a proxy metric of the binding energy between the adsorbent and adsorbate that results from the interaction potential.

Over time an adsorbed molecule may explore many adsorption sites, but due to energetic constraints, the most favorable sites (with the largest isosteric heats) will have the highest average occupation. For conventional adsorbents, the highest isosteric heat values are observed at the lowest coverage. As coverage is increased, the most favorable adsorption sites become saturated. This leads to a decreasing isosteric heat (an average quantity) with increasing coverage.

2. History of Adsorption

Simple adsorptive applications have been employed since at least 1550 BC, when records indicate that the Egyptians made use of charcoals to adsorb putrid gases expelled during human dissection.³ Scientific adsorptive experiments are more recent. Scheele in 1773, followed by Fontana in 1777, were the first scientists to measure the uptake of gases by porous solids.³ Saussure built upon this work, and in 1814 determined that adsorption was exothermic in nature.³ A theoretical understanding of adsorption followed far behind experiments. It wasn't until 1888 that Bemmelen made the first known attempt at fitting adsorption data, introducing a fitting equation now known as the "Freundlich Equation."³ More precise

terminology soon followed when Bois-Reymond and Kayser introduced the term “adsorption” into standard scientific lexiconography.³

By the 20th century, the field of adsorption was full steam ahead. 1903 saw the discovery of selective adsorption (T'wsett)⁴. In 1909 McBain introduced the term “absorption” to differentiate bulk uptake from the surface phenomenon of “adsorption.”⁵ Within the next few decades physisorption had been cast into a number of rigorous theoretical frameworks, namely Eucken-Polanyi Theory (1914)⁶, the Langmuir Isotherm (1918)⁷, BET Theory (1935-1939)^{8,9,10} and Dubinin Theory (1946)¹¹.

3. Adsorption Theory

Apart from limited calorimetric work, the “adsorption isotherm” forms the fundamental basis of adsorption measurement and theory. Constant-temperature isotherms may be measured in a number a ways but ultimately yield the same information: Gibbs excess adsorption as a function of pressure. A simple model for adsorption may be drawn up as follows (Figure 1).

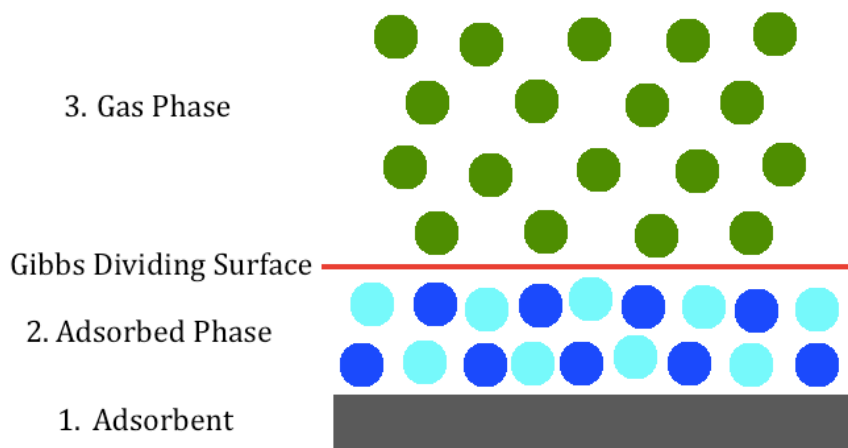


Figure 1. Cartoon depiction of adsorption. The gray rectangle represents the adsorbent

surface. All blue molecules represent absolute adsorption molecules. The dark blue circles represent excess adsorption molecules. The red line indicates a dividing surface. The green circles represent the gas-phase molecules.

Here section 1 represents the solid adsorbent surface, section 2 represents the adsorbed phase (densified molecules near the interface), and section 3 represents the molecules that remain unaffected by the adsorbent and remain free in the gas phase. The quantity of absolute adsorption (n_a) comprises all of the molecules in the adsorbed phase. The volume of the adsorbed phase (V_{ads}), however, is not rigorously established. Thus absolute adsorption cannot be directly measured via experiment. Instead Gibbs worked around this problem by defining excess adsorption (n_e) as follows:

$$n_e = n_a - V_{ads}\rho(P, T) \quad (6)$$

Gibbs excess adsorption differs from absolute adsorption by an amount equal to the volume of the adsorption layer multiplied by the density of the free gas phase ($\rho(P, T)$). Here the volume of the adsorbed phase is defined as the volume between the adsorbent surface and a dividing surface. The quantity of Gibbs excess adsorption measures the amount of adsorbate in the vicinity of the adsorbent surface that is in excess of the free gas phase density. For this reason, the Gibbs excess adsorption is directly measurable by volumetric or gravimetric methods without need for assumptions about the volume of the adsorbed layer. Absolute adsorption, however, cannot be easily and directly measured. Instead it is often crudely assumed that absolute adsorption equals excess adsorption. This assumption is only valid when the gas phase is dilute, and quickly breaks down at high pressures and low temperatures. Thus in this thesis, we instead use a robust fitting method (presented in Chapter 3) to back out

reasonable values of the absolute adsorption.

The first attempts to fit physisorption isotherms came as early as 1888 when Bemmelen introduced what is now known as the “Freundlich Equation”^{12,3}:

$$\frac{n}{m} = KP^{\frac{1}{\eta}} \quad (7)$$

where n is the uptake, m is the mass of the adsorbent, P is equilibrium pressure, and K and η are adsorbent-specific parameters. This equation is only empirical and does not purport to capture or contain the physics of adsorption. Nonetheless, it displays key behaviors that are common to fit functions for type 1 isotherms. At low pressures, uptake increases linearly with pressure per Henry’s Law:

$$n = K_H P \quad (8)$$

where K_H is the Henry’s Law constant. Henry’s Law was first formulated by William Henry in 1803 and can be derived from ideal gas assumptions. If we assume that the adsorbed phase takes the form of a two-dimensional ideal gas following

$$P_a A_a = nRT \quad (9)$$

where P_a and A_a are the spreading pressure and surface area, respectively, and also assume that the equilibrium spreading pressure is proportional to the equilibrium bulk gas pressure, then

$$n = \frac{P_a A_a}{RT} = \frac{c P A_a}{RT} = K_H P \quad (10)$$

Accordingly, the low-pressure regime of an isotherm where uptake is proportional to applied gas pressure is commonly referred to as the Henry’s Law regime. At higher pressures, the adsorption isotherm saturates as all of the available adsorption sites are filled. This correlation, however, is not exact as unlike absolute adsorption, experimentally measured excess adsorption data behaves in a non-monotonic fashion at high pressures. Nonetheless, most type

1 adsorption fit functions subsume both the Henry's Law regime behavior and the saturation regime behavior.

The Langmuir isotherm, derived by Irving Langmuir in 1918⁷, provides a fundamental model for gas adsorption that incorporates both the Henry's Law regime the saturation regime behavior. Here the adsorbed phase is assumed to exist as a monolayer of adsorbate directly above the adsorbent surface. Langmuir's model makes a number of simplifying assumptions as follows:

1. The adsorbent surface is perfectly flat.
2. The gas adsorbs into an immobile state.
3. There is a finite number of adsorption sites that can each be filled by no more than one adsorbate molecule.
4. All adsorption sites are energetically identical.
5. Adsorbate molecules do not interact.

With these simplifying assumptions in hand, the Langmuir adsorption isotherm may be derived from kinetic theory, statistical mechanics, or from a phenomenological perspective, and takes the form:

$$\theta = \frac{KP}{1+KP} \quad (11)$$

where θ is fractional occupancy and K is an equilibrium constant given by an Arrhenius-type equation (Equation 12):

$$K_i = \frac{A_i}{\sqrt{T}} e^{\frac{-E_i}{RT}} \quad (12)$$

where A_i is a prefactor and E_i is an energy of the i^{th} isotherm.

Unfortunately, the five simplifying assumptions above are almost never entirely satisfied and the Langmuir isotherm cannot be applied over broad ranges of conditions. Many of the drawbacks of the Langmuir isotherm may be overcome by fitting excess adsorption data with a weighted superposition of Langmuir isotherms (see Chapter 3).

In particular, the Langmuir model breaks down when multilayer adsorption is possible, as found in larger micropores, mesopores, and macropores. In 1938 Stephen Brunauer, Paul Emmett, and Edward Teller extended the Langmuir model to consider multilayer adsorption.⁸ They realized that in multilayer adsorption, molecules do not successively fill one complete monolayer after another. Rather, fragments of multilayer stacks of varying sizes dot the adsorbent surface. Each layer is in dynamic equilibrium with the layers above and below it, much in the same way that the Langmuir model assumes a dynamic equilibrium between the adsorbed monolayer and the gas phase above it. The Brunauer, Emmett, Teller, or BET method has been elaborated on in detail in literature^{13,14} and will not be rederived here. Rather, the results and key insights are elucidated from the BET equation:

$$\frac{1}{n\left[\left(\frac{P}{P_0}\right)-1\right]} = \frac{C-1}{n_{max}C} \left(\frac{P}{P_0}\right) + \frac{1}{n_{max}C} \quad (13)$$

where n is uptake, P is equilibrium pressure, P_0 is saturation pressure, n_{max} is maximum possible uptake, and C is the BET constant. BET Theory assumes that infinite layers may be adsorbed successively on a surface. Moreover, these layers do not interact with one another and each follow the Langmuir model. Two additional assumptions are made:

1. The E_1 parameter is the isosteric heat between the adsorbent and first adsorbed layer.
2. All higher layers have an E_L parameter equal to the heat of liquefaction of the adsorbate.

BET theory has proven particularly useful at measuring the specific surface areas of porous carbons. For high quality surface area determinations, nitrogen, argon, carbon dioxide, and krypton have been used. In particular, a plot of $\frac{1}{n\left[\left(\frac{P}{P_0}\right)-1\right]}$ vs $\left(\frac{P}{P_0}\right)$ should yield a straight line in the relative pressure range of $0.05 < \left(\frac{P}{P_0}\right) < 0.3$. Using linear regression, the slope and y-intercept of this line are determined. The parameters n_{max} and C are determined by:

$$n_{max} = \frac{1}{(\text{slope} + \text{intercept})} \quad (14)$$

$$C = \left(\frac{\text{slope}}{\text{intercept}}\right) + 1 \quad (15)$$

The surface area may then be determined from n_{max} , using the established cross-sectional area of the probe molecule.

While the Langmuir isotherm rapidly gained popularity and contributed to Irving Langmuir's 1932 Nobel Prize, it competed with Polanyi's theory of adsorption, which has now earned its place in annals of science history. Whereas Langmuir conceptualized adsorption as a monolayer effect localized at the adsorbent surface, Polanyi's approach was more amenable holistic pore filling with longer-range effects. Polanyi reasoned that the density of adsorptive molecules near a surface diminishes with distance from the attractive surface, much the way the atmosphere of a planet thins out at high altitudes. For adsorption this requires a longer-range interaction potential, now called the Polanyi Adsorption Potential⁶.

Polanyi recognized that at equilibrium, the chemical potential (μ) of the adsorbed phase at an arbitrary distance, x , from the interface and a corresponding pressure P_x , must

equal the chemical potential of the gas phase at an infinite distance and corresponding bulk pressure, P .

$$\mu(x, P_x) = \mu(\infty, P) \quad (16)$$

$$\int_{\mu(\infty, P)}^{\mu(x, P_x)} d\mu = \mu(x, P_x) - \mu(\infty, P) = 0 \quad (17)$$

Moreover,

$$d\mu = -SdT + VdP + dU \quad (18)$$

where S is entropy, V is volume and U is the potential energy. Constant temperature (isothermal) conditions yield

$$d\mu = VdP + dU \quad (19)$$

$$\int_{\mu(\infty, P)}^{\mu(x, P_x)} d\mu = \int_P^{P_x} VdP + U(x) - U(\infty) = 0 \quad (20)$$

where $U(x)$ is the potential energy at a distance x from the surface and $U(\infty)$ is the potential energy at an infinite distance, which Polanyi took to be zero:

$$-U(x) = \int_P^{P_x} VdP \quad (21)$$

By substituting in the ideal gas law

$$-U(x) = \int_P^{P_x} \frac{RT}{P} dP \quad (22)$$

or

$$U(x) = RT \ln \left(\frac{P_x}{P} \right) \equiv A \quad (23)$$

where A is the Polanyi potential. While the Polanyi potential went unappreciated for many years, it was given new life in 1946 when Dubinin and Radushkevich introduced the “theory of the volume filling of micropores (TVFM)”^{11,15,16} In this theory the Polanyi potential is the negative of the work done by the sorption system:

$$A = -\Delta G \quad (24)$$

This insight extended the Polanyi potential to broad thermodynamic analysis, codified in the Dubinin-Radushkevich equation:

$$n = n_{max} e^{\left(\frac{A}{\beta E_0}\right)^2} \quad (25)$$

where n is the uptake, n_{max} is the maximum possible uptake, β is the affinity coefficient, and E_0 is the standard characteristic energy. Other modified and more generalized forms were later introduced, such as the Dubinin-Astakhov equation¹⁷

$$n = n_{max} e^{\left(\frac{A}{\beta E_0}\right)^\chi} \quad (26)$$

where χ is an adsorbent-specific heterogeneity parameter.

If uptake is plotted as a function of the Polanyi potential, the Dubinin-Radushkevich equation¹⁵ yields a single characteristic curve for each gas-adsorbent system. In theory the characteristic curve may be used to predict uptake over a wide range of temperatures and pressures, and its accuracy has been generally confirmed by experiment.^{18,19} Moreover, plotting $\ln(n)$ as a function of $-\left(\frac{A}{\beta E_0}\right)^2$ yields a linear trend, wherein the y-intercept gives the maximal uptake (n_{max}) and the slope gives the characteristic energy (E_0). The parameter n_{max} may be used to determine the total micropore volume of the adsorbent by multiplying by the established molecular volume of the adsorbate. The parameter E_0 may be used to estimate an average micropore width.

References:

1. Siderius, D. W.; Gelb, L. D. Extension of the Steele 10-4-3 Potential for Adsorption Calculations in Cylindrical, Spherical, and Other Pore Geometries. *J. Chem. Phys.* **2011**, *135*, 084703-1-7.
2. Boda, D.; Henderson, D. The Effects of Deviations from Lorentz-Berthelot Rules on the Properties of a Simple Mixture. *Mol. Phys.* **2008**, *106*, 2367-2370.
3. Dabrowski, A. Adsorption-From Theory to Practice. *Adv. Colloid Interface Sci.* **2001**, *93*, 135-224.
4. Berezkin, V.G. (Compiler). Chromatographic Adsorption Analysis: Selected Works of M.S. Tswett. *Elis Horwood*: New York, 1990.
5. McBain, J. W. The Mechanism of the Adsorption ("Sorption") of Hydrogen by Carbon. *Philos. Mag.* **1909**, *18*, 916-935.
6. Polanyi, M., Potential Theory of Adsorption. *Science.* **1963**, *141*, 1010-1013.
7. Langmuir, I. The Adsorption of Gases on Plane Surfaces of Glass, Mica and Platinum. *J. Am. Chem. Soc.* **1918**, *40*, 1361-1403.
8. Brunauer, S.; Emmett, P. H.; Teller, E. Adsorption of Gases in Multimolecular Layers. *J. Am. Chem. Soc.* **1938**, *60*, 309-319.
9. Brunauer, S.; Emmett, P. H. The Use of Low Temperature van der Waals Adsorption Isotherms in Determining the Surface Areas of Various Adsorbents. *J. Am. Chem. Soc.* **1937**, *59*, 2682-2689.
10. Brunauer, S.; Emmett, P. H. The Use of van der Waals Adsorption Isotherms in Determining the Surface Area of Iron Synthetic Ammonia Catalysts. *J. Am. Chem. Soc.* **1935**, *57*, 1754-1755.
11. Dubinin, M. M.; Radushkevich, L. V. Equation of the Characteristic Curve of Activated Charcoal. *Proc. Acad. Sci. USSR Phys. Chem.* **1947**, *55*, 331-337.
12. Skopp, J. Derivation of the Freundlich Adsorption Isotherm from Kinetics. *J. Chem. Educ.* **2009**, *86*, 1341-1343.
13. Gregg, S. J.; Jacobs, J. An Examination of the Adsorption Theory of Brunauer, Emmett, and Teller, and Brunauer, Deming, Deming and Teller. *T. Faraday Soc.* **1948**, *44*, 574-588.
14. Legras, A.; Kondor, A.; Heitzmann, M. T.; Truss, R. W. Inverse Gas Chromatography for Natural Fibre Characterisation: Identification of the Critical Parameters to Determine the Brunauer-Emmett-Teller Specific Surface Area. *J. Chromatogr. A.* **2015**, *1425*, 273-279.
15. Nguyen, C.; Do, D. D. The Dubinin-Radushkevich Equation and the Underlying Microscopic Adsorption Description. *Carbon.* **2001**, *39*, 1327-1336.
16. Dubinin, M. M. Generalization of the Theory of Volume Filling of Micropores to Nonhomogeneous Microporous Structures. *Carbon.* **1985**, *23*, 373-380.
17. Burevski, D. The Application of the Dubinin-Astakhov Equation to the Characterization of Microporous Carbons. *Colloid Polym. Sci.* **1982**, *260*, 623-627.
18. Saeidi, N.; Parvini, M. Accuracy of Dubinin-Astakhov and Dubinin-Radushkevich Adsorption Isotherm Models in Evaluating Micropore Volume of Bentonite. *Period. Polytech. Chem.* **2016**, *60*, 123-129.

19. Do, D. D.; Nicholson, D.; Do, H. D. Adsorption in Micropores (Nanopores): A Computer Appraisal of the Dubinin Equations. *Mol. Simul.* **2009**, *35*, 122-137.

Chapter 3

Experimental Methods and Analysis

1. Equipment

The fundamental basis of quantitative adsorption analysis is the measurement of excess adsorption isotherms. Each isotherm comprises a series of excess adsorption uptake values, measured stepwise at increasing pressures and a constant temperature. At high pressure, the excess adsorption becomes non-monotonic as a function of pressure, after reaching an excess adsorption maximum. A desorption isotherm may be measured in reverse, by starting with a preloaded adsorbent at high pressures and reducing the pressure stepwise. Observed hysteresis between pairs of adsorption and desorption isotherms yields valuable information about the adsorptive system, often indicating the presence of capillary condensation in mesopores.

In this thesis, excess adsorption isotherms were measured by the volumetric method also known as the Sieverts' method using a custom Sieverts apparatus designed and tested for accuracy up to 10 MPa (Figure 1).¹ The Sieverts apparatus comprises a number of rigid, stainless steel, and leak-proof compartments, each interconnected with controllable on-off valves (either hand-turned or pneumatic). The volume of each compartment is known with high precision (± 0.01 mL). For standard adsorption measurements, only two of the compartments are of interest: the manifold and the reactor. The manifold is equipped with a midrange (3000 PSI) MKS Baratron (Model 833) pressure transducer for high-pressure measurements and an MKS Baratron (Model 120AA) for low-pressure measurements of higher resolution. The temperature of the gas in the manifold was measured with platinum

resistance thermometers. The temperature of the reactor was monitored with K-type thermocouples. In a preparatory step the adsorbent sample of interest was weighed and sealed within the reactor, which seals by the tightening of a conflat flange with a copper gasket. Additional nickel filter gaskets with a 0.5-micron mesh size prevented the adsorbent from escaping from the reactor. After sealing the reactor, each sample was degassed at ~ 520 K under a vacuum of less than 10^{-3} Pa prior to testing. The Sieverts apparatus is equipped with a molecular drag pump capable of achieving a vacuum of 10^{-4} Pa and vacuum pressures were verified using a digital cold cathode pressure sensor (I-MAG, Series 423). To obtain low temperature isotherms, the reactor was submerged in a circulated chiller bath or cryogenic bath with temperature fluctuations no larger than ± 0.1 K. High temperature isotherms were obtained by encasing the reactor in a copper heat conductor wrapped with insulating fiberglass heating tape. Using a proportional integral derivative (PID) controller, the reactor temperature was maintained with fluctuations no larger than ± 0.4 K. Prior to measurements, the entire Sieverts was purged multiple times with the gas of interest to eliminate any impurity residues. On each sample, multiple adsorption/desorption isotherms were taken to ensure complete reversibility and identical measurements were found to be reproducible to within 1% error.

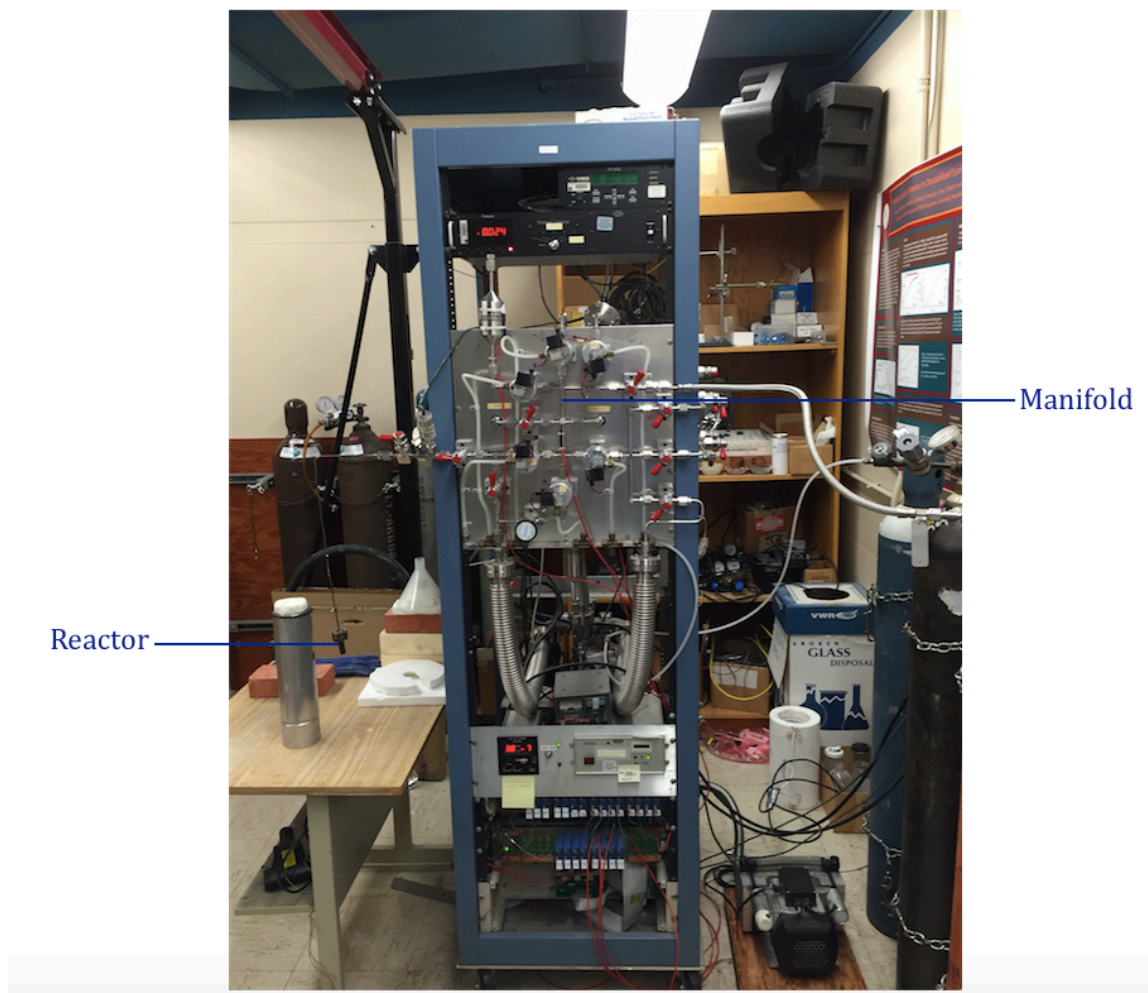


Figure 1. Sieverts Apparatus

2. Methodology

For each isotherm data point, a predetermined pressure of research-grade gas was introduced into and cached in the manifold. Upon reaching equilibrium, the temperature and pressure of this gas were measured with high precision and the gas density was determined from REFPROP data tables². Given that the manifold volume is known, the moles of gas in the manifold were thus determined. Next, a valve was opened to allow the gas to occupy both the manifold and reactor volumes. The reactor housed the porous sample of known mass. Upon opening the valve, the gas was allowed to occupy a volume given by the sum of the

manifold and reactor volumes minus the volume of the sample. The volume of the sample was given by the product of the sample mass and the sample skeletal density (obtained by helium pycnometry). Once equilibrium was reestablished, pressure and temperature measurements were taken and a final gas-phase density determined for the step. The moles of gas left in the gas phase were thus calculated. Any quantity of gas introduced into the manifold, but no longer contributing to the gas-phase pressure was considered to be in the adsorbed phase. The sample within the reactor was held at a constant temperature over the course of a successive set of pressure measurements, resulting in an excess adsorption isotherm. Upon completion of an isotherm, the temperature was adjusted for the next isotherm, in order to measure a multitude of isotherms over a wide temperature range.

At equilibrium the chemical potential of the gas phase (μ_g) and the adsorbed phase (μ_a) are equal

$$\mu_a = \mu_g \quad (1)$$

By taking the total differential of both sides of Equation 1:

$$-s_a dT + v_a dP = -s_g dT + v_g dP \quad (2)$$

$$\frac{dP}{dT} = \frac{(s_g - s_a)}{(v_g - v_a)} \quad (3)$$

Thus the derivative of pressure with respect to temperature is related to the change in entropy (upon adsorption) divided by the change in volume (upon adsorption). At constant coverage, the difference between the entropy of the adsorbed phase (S_a) and the entropy of the gas phase (S_g) is the isosteric entropy of adsorption (ΔS_{ads}) and is given by Equation 4.

$$\Delta S_{ads} = S_a - S_g \quad (4)$$

$$\Delta S_{ads} = (v_g - v_a) \frac{dP}{dT} \quad (5)$$

The isosteric entropy of adsorption is in turn related to isosteric enthalpy of adsorption (ΔH_{ads})

by Equation 6

$$\frac{\Delta H_{ads}}{T} = \Delta S_{ads} \quad (6)$$

At constant coverage, the difference between the adsorbed and gas-phase enthalpies is thus given by Equation 7

$$\Delta H_{ads} = T(v_g - v_a) \frac{dP}{dT} \quad (7)$$

This is the Clapeyron equation, and is fundamental to the calculation of the isosteric enthalpy of adsorption. A number of simplifying assumptions may be made in dealing with the Clapeyron equation. The two most common are as follows:

1. That the volume of the gas phase is significantly larger than that of the adsorbed phase such that the overall change in volume is well approximated as the gas-phase volume.
2. That the gas follows the ideal gas law.

Together these assumptions transform the Clapeyron equation into Equation 8

$$\Delta H_{ads}(n_a) = -\frac{RT^2}{P} \left(\frac{dP}{dT} \right)_{n_a} \quad (8)$$

This may in turn be rearranged into the Van't Hoff form:

$$\Delta H_{ads}(n_a) = R \left(\frac{d \ln P}{d \left(\frac{1}{T} \right)} \right)_{n_a} \quad (9)$$

By plotting $\ln(P)$ vs $(1/T)$, a Van't Hoff plot is formed. The slope of the Van't Hoff plot multiplied by R gives the isosteric heat. In common practice, adsorption measurements directly determine excess adsorption (n_e), not absolute adsorption (n_a). It is thus common to hold excess adsorption, not absolute adsorption, constant in Equation 9. This results in an isoexcess

enthalpy of adsorption that approximates the isosteric enthalpy of adsorption, but only at low gas densities. The previously mentioned assumptions fail when applied broadly to gas data. Thus we must consider alternatives to these oversimplifying assumptions.

First, the ideal gas assumption may be avoided by inserting values from gas data tables directly into the Clapeyron equation. This is the course of action followed in this thesis. Using gas data tables enables thermodynamic calculations outside of the ideal gas regime. Second, the simplified Clausius-Clapeyron equation assumes that the adsorbed phase has virtually zero volume and that the net difference between the molar volume of the gas phase and the adsorbed phase equals the molar volume of the gas phase. In reality, the adsorbed phase has a finite molar volume that approaches that of the liquid phase of the adsorbed species. Thus the assumption of a zero molar volume adsorbed phase may be replaced with one of two options. Either the adsorbed-phase molar volume is assumed to be equal to that of the liquid phase molar volume, or, fit functions are used to approximate the adsorbed-phase molar volume.

In applying the Clapeyron equation, it is necessary to take the derivative of pressure with respect to temperature at constant coverage conditions. Where absolute adsorption is held constant, this determines the isosteric enthalpy of adsorption and where the excess adsorption is held constant, this determines the isoexcess enthalpy of adsorption. In practice, however, neither absolute nor excess adsorption is an experimentally tunable variable. The uptake quantity is never directly selected, rather the pressure is roughly selected. Thus obtaining data points at constant coverage conditions is not simple. In some cases, with sufficient data, constant coverage conditions across a number of temperatures may be achieved for select data points by pure coincidence. This can be thought of as “analysis without fitting”. Fortuitously positioned data points, however, are sparse and unreliable.

In general it is necessary to establish an interpolation function to interpolate between the measured data points. Interpolation functions of a variety of forms have been employed in literature. The simplest entails linear interpolation between data points.

While simple, this approach fails to accurately capture the adsorption behavior, leading to scatter and errors. In this thesis research I employ a superposition of Langmuir isotherms as the fitting function of choice. Specifically, starting from the definition of excess adsorption (n_e):

$$n_e = n_a - V_a \rho(P, T) \quad (10)$$

I fit the absolute adsorption (n_a) and the volume of the adsorption layer (V_a) with superpositions of Langmuir isotherms with appropriate prefactors:

$$n_a(P, T) = n_{max} \sum_i a_i \left(\frac{K_i P}{1 + K_i P} \right) \quad (11)$$

$$V_a(P, T) = V_{max} \sum_i a_i \left(\frac{K_i P}{1 + K_i P} \right) \quad (12)$$

where a_i is the respective weight of the i^{th} isotherm ($\sum_i a_i = 1$), P is the pressure, and K_i is an equilibrium constant given by an Arrhenius-type equation such that:

$$K_i = \frac{A_i}{\sqrt{T}} e^{\frac{-E_i}{RT}} \quad (13)$$

where A_i is a prefactor and E_i is an energy of the i^{th} isotherm. Altogether the fit function becomes:

$$n_e(P, T) = (n_a - V_{max} \rho(P, T)) \sum_i a_i \left(\frac{K_i P}{1 + K_i P} \right) \quad (14)$$

One particular advantage of this fitting procedure is that the absolute adsorption is easily accessible. It is one of the quantities that is directly fitted and given by Equation 11.

Absolute adsorption is a more fundamental quantity than excess adsorption, and its determination is critical for in-depth analysis of the adsorption physics.

In addition to producing high quality fits, the dual-Langmuir fitting method used in this thesis gives physically realistic fitting parameters. In particular the n_{max} and v_{max} parameters have been found to be in reasonable agreement with independently determined physical data (See Chapter 9). The n_{max} parameter gives the maximum possible absolute adsorption as determined by fits. This is directly comparable to an estimate of the maximum possible adsorption as obtained by multiplying the measured micropore volume by the liquid density of the adsorptive species². Here we assume that the entirety of the micropores is filled with adsorbate at a density equal to the liquid density (upon maximal adsorption). Furthermore, the v_{max} parameter indicates the maximum possible volume of the adsorbed phase, which may be directly compared to the measured micropore volume of the adsorbent.

While the isosteric enthalpy of adsorption (ΔH_{ads}) is a popularly cited proxy metric of binding site energy, a more fundamental metric exists in the adsorbed-phase molar enthalpy (H_a) given by Equation 15. The isosteric enthalpy of adsorption is the difference between the adsorbed-phase and gas-phase (H_g) molar enthalpies and thus retains a dependence on gas-phase properties.

$$H_a = H_g + \Delta H_{ads} \quad (15)$$

For nonideal gas conditions, this dependence can obscure interesting phenomenon occurring strictly within the adsorbed phase. The gas-phase enthalpy is obtained from reference tables². The adsorbed-phase enthalpy gives critical insight into the nature of the adsorbent-adsorbate

binding-site energy. Moreover, the constant pressure molar heat capacity of the adsorbed phase (C_p) follows directly from the adsorbed-phase enthalpy (Equation 16):

$$C_p = \left. \frac{dH_a}{dT} \right|_p \quad (16)$$

The adsorbed-phase molar heat capacities provide critical qualitative insight into the adsorbed-phase layer. For a monatomic gas like krypton, comparison to theoretical estimates of the heat capacity provides further means to peer into the underpinnings of the adsorbed-phase thermodynamics. Furthermore, the isosteric entropy of adsorption (ΔS_{ads}) is directly accessible from the isosteric enthalpy of adsorption:

$$\Delta S_{ads} = \frac{\Delta H_{ads}}{T} \quad (17)$$

By adding the isosteric entropy of adsorption to the gas-phase molar entropy (from REFPROP²), we obtain the adsorbed-phase molar entropy (S_a).

$$S_a = S_g + \Delta S_{ads} \quad (18)$$

References:

1. Bowman, R. C.; Luo, C. H.; Ahn, C. C.; Witham, C. K.; Fultz, B. The Effect of Tin on the Degradation of LaNi₅-YsNy Metal-Hydrides During Thermal Cycling. *J. Alloys and Compd.* **1995**, *217*, 185-192.
2. Lemmon, E. W.; Huber, M. L.; McLinden, M. O. *NIST Standard Reference Database 23: Reference Fluid Thermodynamic and Transport Properties-REFPROP*, version 8.0; National Institute of Standards and Technology: Gaithersburg, MD, 2007; CD-ROM.

Chapter 4

Materials

Three carbonaceous materials, MSC-30, CNS-201, and zeolite-templated carbon (ZTC) were studied repeatedly with different gases and under differing conditions in this work. These materials were obtained and characterized in varied ways described herein.

1. MSC-30

MSC-30 (Maxsorb) is a microporous superactivated carbon obtained from Kansai Coke & Chemicals Company Ltd. (Japan) and is an “AX21-type” superactivated carbon. MSC-30 is synthesized by activating petroleum coke with molten KOH in a process patented by Standard Oil Company (later Amoco Corporation).

Nitrogen adsorption isotherms were carried out at 77K in a Micromeritics ASAP 2420. The specific surface area was determined by applying BET theory to the data as implemented by Micromeritics ASAP 2420 version 2.02 software. The BET surface area of MSC-30 was determined to be $3244 \pm 28 \text{ m}^2 \text{ g}^{-1}$. Using nonlocal density functional theory (NLDFT)¹ and a slit-pore model, the MSC-30 pore-size distribution was determined as shown in Figure 1. MSC-30 has a broad range of pore sizes (from 6 to 35 Å). Over 40% of the micropore volume is contained in pores of greater than 21 Å (width). The micropore volume was found to be $1.54 \text{ cm}^3 \text{ g}^{-1}$ by the Dubinin-Radushkevich method^{2,3}. The skeletal density was measured by helium pycnometry and the skeletal density determined to be 2.1 g cm^{-3} .

Cu K α X-ray diffraction of MSC-30 on a PANalytic Pro powder diffractometer gave a broad peak at $2\theta = 34$ degrees, in accordance with that reported for AX21. The elemental composition (CHN) was determined by the Dumas method⁴ in triplicate combustion experiments, indicating that 1.16 wt% of MSC-30 is hydrogen. X-Ray Photospectroscopy (XPS) measurements were made on a Kratos AXIS Ultra DLD spectrometer and the results are summarized in Table 1. Electron Energy Loss Spectroscopy (EELS) measurements were made on a FEI Technai F20 with a Gatan Imaging Filter system. MSC-30 has an sp^3 hybridized carbon content of 16%. Transmission electron microscope (TEM) images were taken with a Tecnai TF30 with a LaB₆ filament and 80 keV electrons (Figure 2).

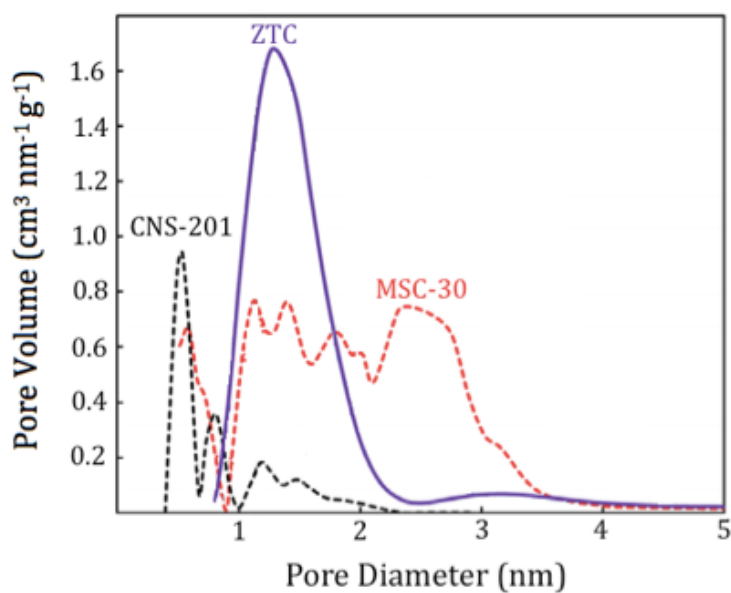


Figure 1. The pore-size distribution (left) of MSC-30 (red), CNS-201 (black), and ZTC (purple) as calculated by the NLDFIT method.

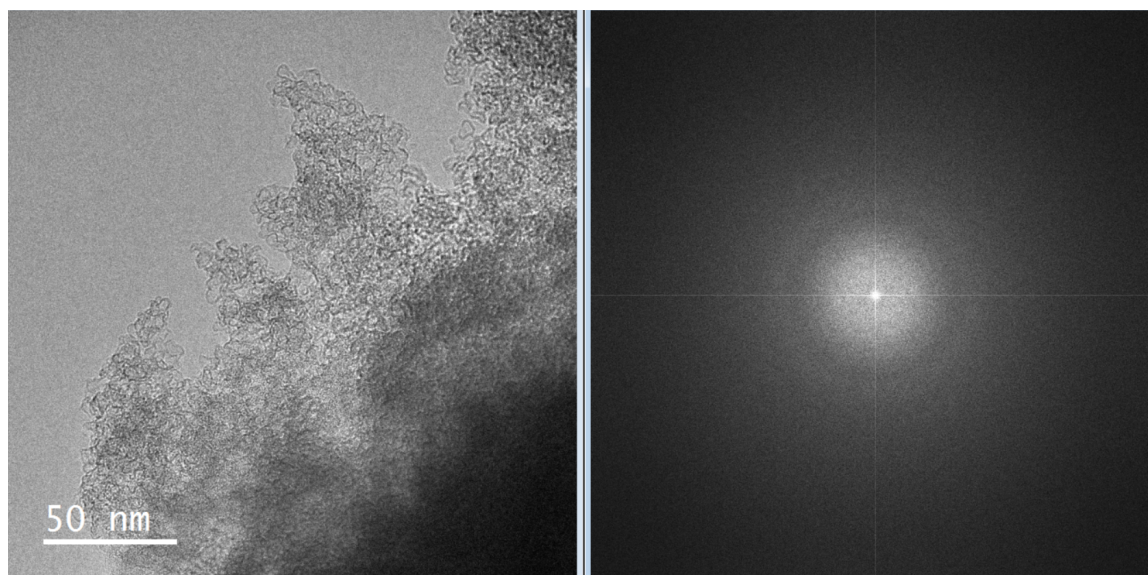


Figure 2. TEM image of MSC-30 and an accompanying fast Fourier transform of the image.

Table 1. Summary of XPS data on MSC-30 and ZTC

| peak position (eV) | 285.0 | 285.7 | 286.4 | 287.3 | 288.1 | 289.4 | 290.2 | 291.5 |
|--------------------|---------------------|---------------------|-------|-------|-------|-------|-------|-------|
| component | C-C sp ² | C-C sp ³ | C-OR | C-O-C | C=O | COOR | - | - |
| ZTC | 53.4 | 18.0 | 8.6 | 6.0 | 1.1 | 4.2 | 1.0 | 7.7 |
| MSC-30 | 48.0 | 18.8 | 6.8 | 4.8 | 6.1 | 4.2 | 3.6 | 7.7 |

2. CNS-201

CNS-201 is a microporous activated carbon obtained from A. C. Carbone Inc. (Canada). It is synthesized by pyrolysis of coconut shells. Nitrogen adsorption isotherms were carried out at 77K in a Micromeritics ASAP 2420. The specific surface area was determined by applying BET theory to the data as implemented by Micromeritics ASAP 2420 version 2.02 software. As determined by nitrogen adsorption and BET analysis, CNS-201 has a surface area of $1095 \pm 8 \text{ m}^2 \text{ g}^{-1}$. Using the nitrogen adsorption data and a slit pore model, NLDFT¹ pore-

size analysis was conducted to determine the pore size distribution (Figure 1). CNS-201 has a three dominant pore widths of 5.4, 8.0, and 11.8 Å, containing roughly 50%, 20%, and 15% of the total micropore volume respectively. The micropore volume was found to be 0.45 cm³ g⁻¹ by the Dubinin-Radushkevich method^{2,3}. The skeletal density was measured by helium pycnometry and the skeletal density determined to be 2.1 g cm⁻³. Transmission electron microscope (TEM) images were taken with a Tecnai TF30 with a LaB₆ filament and 80 keV electrons (Figure 3).

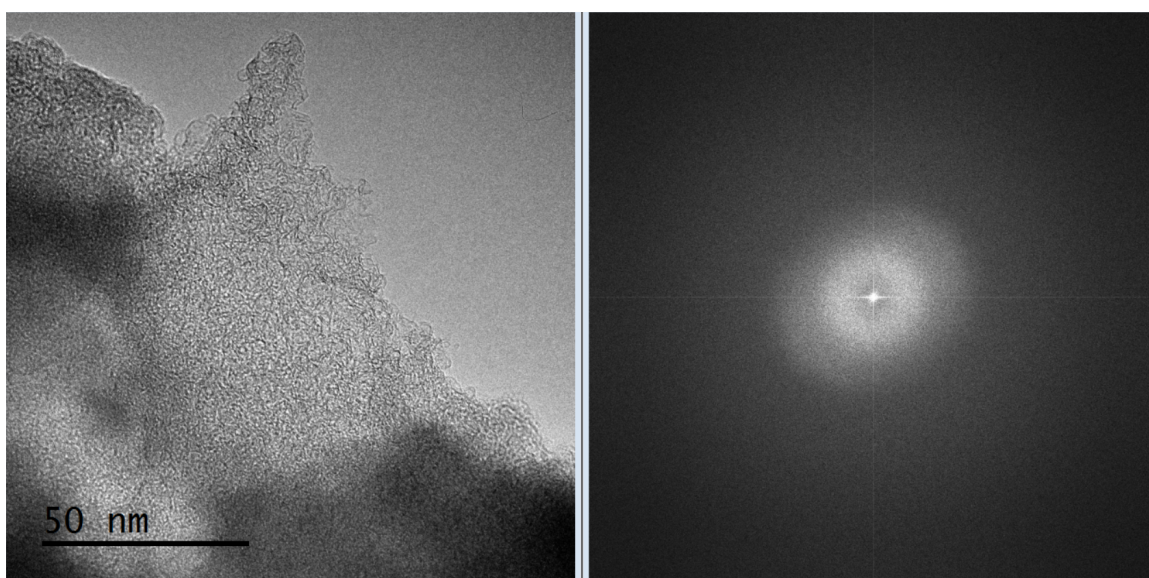


Figure 3. TEM image of CNS-201 and an accompanying fast Fourier transform of the image.

3. Zeolite-Templated Carbon

Zeolite-Templated Carbon (ZTC) is a microporous templated carbon synthesized in multi-gram quantities with the following procedure at HRL Laboratories.

3.1 ZTC Synthesis

Faujasite-type Zeolum® zeolite NaY, HSZ-320NAA (faujasite structure, Na cation, $\text{SiO}_2/\text{Al}_2\text{O}_3 = 5.5$ mol/mol) (NaY) was obtained from Tosoh Corporation. 6.0 grams of zeolite NaY were dried under vacuum at 450 °C for 8 hours. This powder was cooled and mixed with 12 mL of furfuryl alcohol (98% Sigma Aldrich) and stirred under Argon for 24 hours. The resulting zeolite-furfuryl alcohol mixture was separated by vacuum filtration and rinsed four times in 100 mL aliquots of xylenes.

Next the powder was loaded in a quartz boat and placed in quartz tube-furnace/CVD reactor. The tube furnace was purged with argon and held under argon at 80 °C for 24 hours. The reactor was heated to 150 °C (under argon) for 8 hours to induce polymerization. Next the temperature was ramped up at a rate of 5 degrees °C per minute to a final temperature of 700 °C whereupon the gas flow was switched to a 7% propylene/ 93% nitrogen mixture for 4 hours. After 4 hours, the reactor was purged with argon at 700 °C for 10 minutes. Next the temperature was increased to 900 °C and held for 3 hours under argon.

This product was then cooled and transferred to a PTFE beaker. 200 milliliters of aqueous hydrofluoric acid (48% Sigma Aldrich) were added. The solution was left for 16 hours before collecting the ZTC by vacuum filtration and rinsing 10 times with 50 mL aliquots of water. Finally the ZTC product was dried at 150 °C under vacuum. Careful control of the

inert atmosphere and thorough drying were found to be critical to obtaining high surface area product.

3.2 ZTC Characterization

Nitrogen adsorption isotherms at 77K were measured on a BELSORP-max volumetric instrument (BEL-Japan Inc.). This data was analyzed with BET theory to determine a specific surface area of $3591 \pm 60 \text{ m}^2 \text{ g}^{-1}$ (among the highest to date for carbonaceous materials)⁵. Using nitrogen adsorption data and a slit-pore model, NLDFIT¹ pore-size analysis was conducted to determine the pore-size distribution (Figure 1). Other geometrical models including a cylindrical pore model were also tried, but none fit the data better than the slit-pore model. ZTC has a narrow pore-size distribution centered at 12 Å. Over 90% of the micropore volume is contained in pores of widths between 8.5 and 20 Å. The micropore volume was found to be $1.66 \text{ cm}^3 \text{ g}^{-1}$ by the Dubinin-Radushkevich method^{2,3}. The skeletal density was measured by helium pycnometry and determined to be 1.8 g cm^{-3} . This is lower than most carbonaceous adsorbents (2.1 g cm^{-3}), likely owing to a higher percent of hydrogen terminations. The elemental composition (CHN) was determined via the Dumas method⁴ in triplicate combustion experiments, indicating that 2.44 wt% of ZTC is hydrogen. This higher percentage of hydrogen terminations may result from the hydrofluoric acid treatment during synthesis.

Cu K α X-ray diffraction of ZTC was measured with a PANalytic X'Pert Pro powder diffractometer and produced a single sharp peak at $2\theta = 6$ degrees, indicative of the template periodicity (14 Å). No signal from the original zeolite material was registered in the final product. The absence of other peaks suggests that the product is (as expected) amorphous

carbon without any remnant zeolite. Applying the Scherrer equation⁶ to the peak (with a Scherrer constant $K=0.83$ for spherical particles) suggests an ordering length scale of 24 nm.

X-Ray Photospectroscopy (XPS) measurements were made on a Kratos AXIS Ultra DLD spectrometer and the results are summarized in Table 1. No significant differences were noted as compared to MSC-30. Electron Energy Loss Spectroscopy (EELS) measurements were made on a FEI Technai F20 with a Gatan Imaging Filter system. Similar to MSC-30, ZTC has an sp^3 -hybridized carbon content of 18%. Transmission electron microscope (TEM) images were taken with a Tecnai TF30 with a LaB_6 filament and 80 keV electrons (Figure 4). The samples were prepared by placing the powder on an aluminum foil square and putting a lacey carbon copper TEM grid on top to pick up some particles. Unlike MSC-30 and CNS-201, ZTC shows nongraphitic crystalline order in the Fourier transform of the TEM images. In the fast Fourier transform of the images (Figure 4), ZTC shows spots indicative of a spacing of 1.2 to 1.3 nanometers, in agreement with other measurements of the periodicity of the pores. The spots also suggest hexagonal symmetry in the pore arrangement.

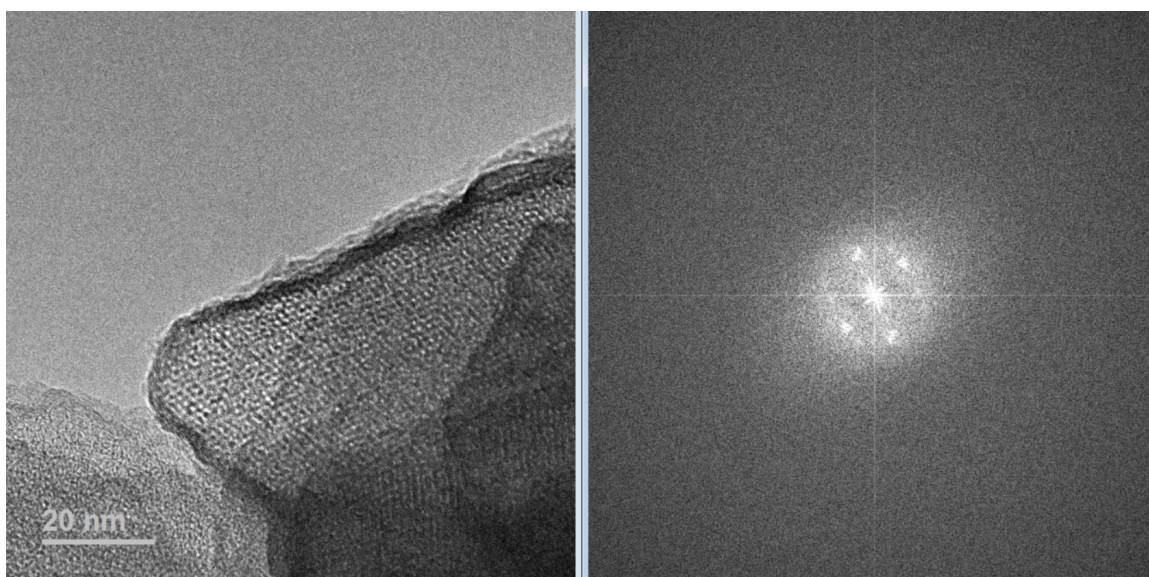


Figure 4. TEM image of ZTC and an accompanying fast Fourier transform of the image.

References:

1. Tarazona, P.; Marconi, U. M. B.; Evans, R. Phase-Equilibria of Fluid Interfaces and Confined Fluids - Nonlocal Versus Local Density Functionals. *Mol. Phys.* **1987**, *60*, 573-595.
2. Dubinin, M. M.; Radushkevich, L. V. Equation of the Characteristic Curve of Activated Charcoal. *Proc. Acad. Sci. USSR Phys. Chem.* **1947**, *55*, 331-337.
3. Burevski, D. The Application of the Dubinin-Astakhov Equation to the Characterization of Microporous Carbons. *Colloid Polym. Sci.* **1982**, *260*, 623-627.
4. Dumas, J. B. A Method of Estimating Nitrogen in Organic Material. *Ann. Chim. Phys.* **1833**, *58*, 171-173.
5. Yang, Z. X.; Xia, Y. D.; Mokaya, R. Enhanced Hydrogen Storage Capacity of High Surface Area Zeolite-Like Carbon Materials. *J. Am. Chem. Soc.* **2007**, *129*, 1673-1679.
6. Langford, J. I.; Wilson, A. J. C. Scherrer After 60 Years - Survey and Some New Results in Determination of Crystallite Size. *J. Appl. Crystallogr.* **1978**, *11*, 102-113.

Chapter 5

Methane on Microporous Carbons

N.P. Stadie, M. Murialdo, C.C. Ahn, and B. Fultz, “Unusual Entropy of Adsorbed Methane on Zeolite-Templated Carbon,” *J. Phys. Chem. C*, 119, 26409 (2015).

DOI: 10.1021/acs.jpcc.5b05021

<http://pubs.acs.org/doi/abs/10.1021/acs.jpcc.5b05021?journalCode=jpcck>

N.P. Stadie, M. Murialdo, C.C. Ahn, and B. Fultz, “Anomalous Isothermic Enthalpy of Adsorption of Methane on Zeolite-Templated Carbon,” *J. Am. Chem. Soc.* 135, 990 (2013).

DOI: 10.1021/ja311415m

<http://pubs.acs.org/doi/abs/10.1021/ja311415m>

1. Adsorptive Uptake

The ability to store the necessary quantities of natural gas in inexpensive and moderately sized onboard tanks remains a significant challenge to the wide-spread adoption of natural gas as a fuel in the transportation sector. By filling the onboard tanks with specially designed physisorptive materials, the storage capacity can be significantly improved and the volumetric energy density significantly increased. Here we study high-pressure methane adsorption on three microporous carbons (ZTC, MSC-30, and CNS-201). The zeolite-templated carbon (ZTC) is of particular interest due to its unique synthesis and morphology (a narrow pore-size distribution centered at 1.2 nm).

Methane isotherms were measured at 13 temperatures from 238 to 526K and up to pressures of ~10 MPa in a volumetric Sieverts apparatus, commission and verified for accurate measurements up to 10 MPa¹. Multiple adsorption runs were completed at each temperature

with research-grade methane (99.999%) and errors between cycles were less than 1%. Adsorption/desorption cycles demonstrated full reversibility of the isotherms. The excess adsorption isotherms are plotted in Figure 1. Unlike absolute adsorption, excess adsorption reaches a maximum at high pressures. This maximum is a readily accessible figure of merit for the gravimetric performance of a material at a fixed temperature. The excess maximum is similar for ZTC-3 and MSC-30 at room temperature, but slightly higher for MSC-30 at 14.5 mmol g⁻¹ at 8 MPa. While excess adsorption increases faster for MSC-30 at pressures between 0 and 0.8 MPa, uptake in ZTC-3 increases fastest between 0.8 and 5.7 MPa. CNS-201 has much lower maxima due to its significantly smaller surface area. The highest measured excess uptake of this study is for ZTC-3 at 238 K: 22.1 mmol g⁻¹ (26.2 wt%) at 4.7 MPa, despite a gentler initial increase at low pressure. Interestingly, the excess uptake in ZTC-3 is also greater than for MSC-30 at high temperatures, although neither reaches a maximum between 0 and 9 MPa. At all temperatures, methane uptake in ZTC-3 is characterized by a gradual initial rise and delayed increase at pressures between 0.2 and 2 MPa, leading to higher eventual methane capacity than MSC-30, a material of comparable specific surface area. The measured excess adsorption maxima (at a sample temperature of 298K) scale linearly with specific surface area and are consistent with the reported linear trend for methane uptake at 3.5 MPa and 298 K.²

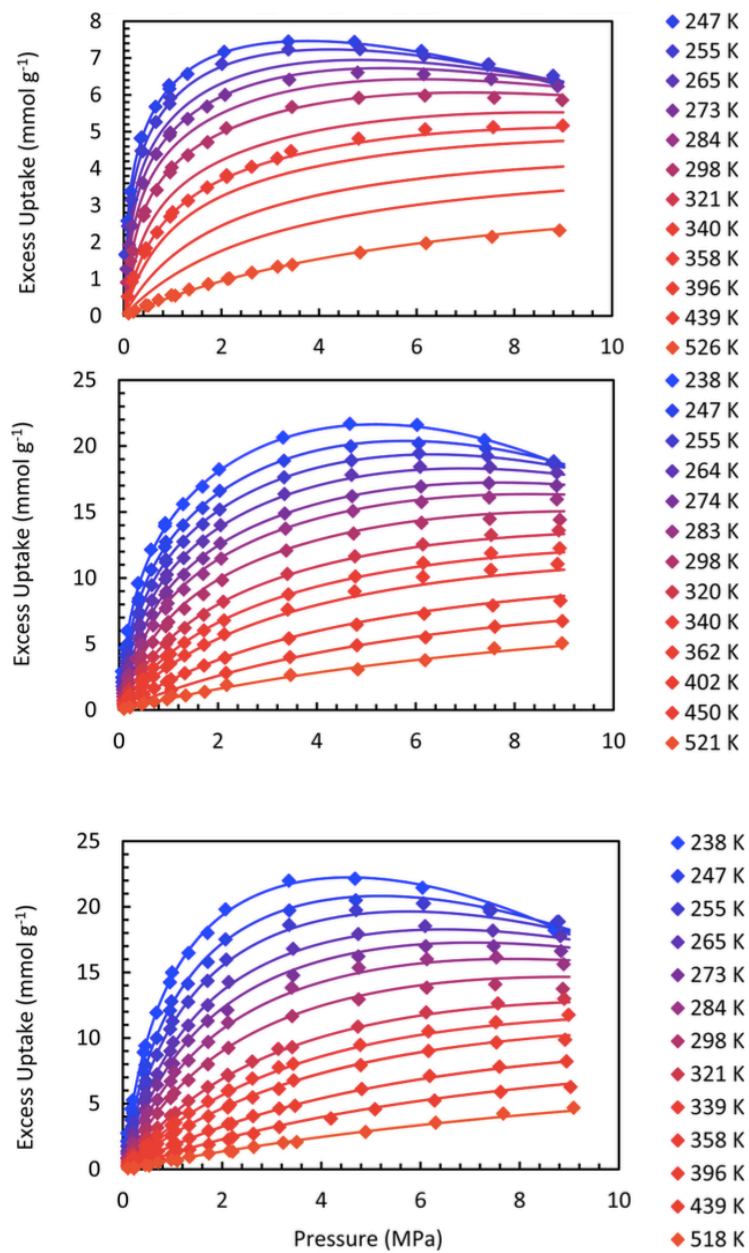


Figure 1. Measured methane excess adsorption as a function of temperature and pressure on CNS-201 (top), MSC-30 (middle), and ZTC (bottom). The curves indicate the best fit obtained with a dual-Langmuir fitting function.

2. Analysis

The excess adsorption data were fitted with a superposition of two Langmuir isotherms, as detailed in Chapter 3. In general, the best-fit parameters obtained correlate with physical properties of the materials studied. For example, the parameter indicative of the maximum volume of the adsorbed layer, V_{max} can be independently verified through comparison to the micropore volume of the adsorbent as measured with the Dubinin-Radushkevich method^{3,4}. In ZTC, if taken to be proportional to surface area, the V_{max} parameter corresponds to half of the mean pore width of the material: a thickness of 0.6 nm. Likewise, the maximum possible adsorption quantity, given by parameter n_{max} correlates well with an estimate determined by the product of the micropore volume and the molar liquid density of the adsorbate (methane)⁵.

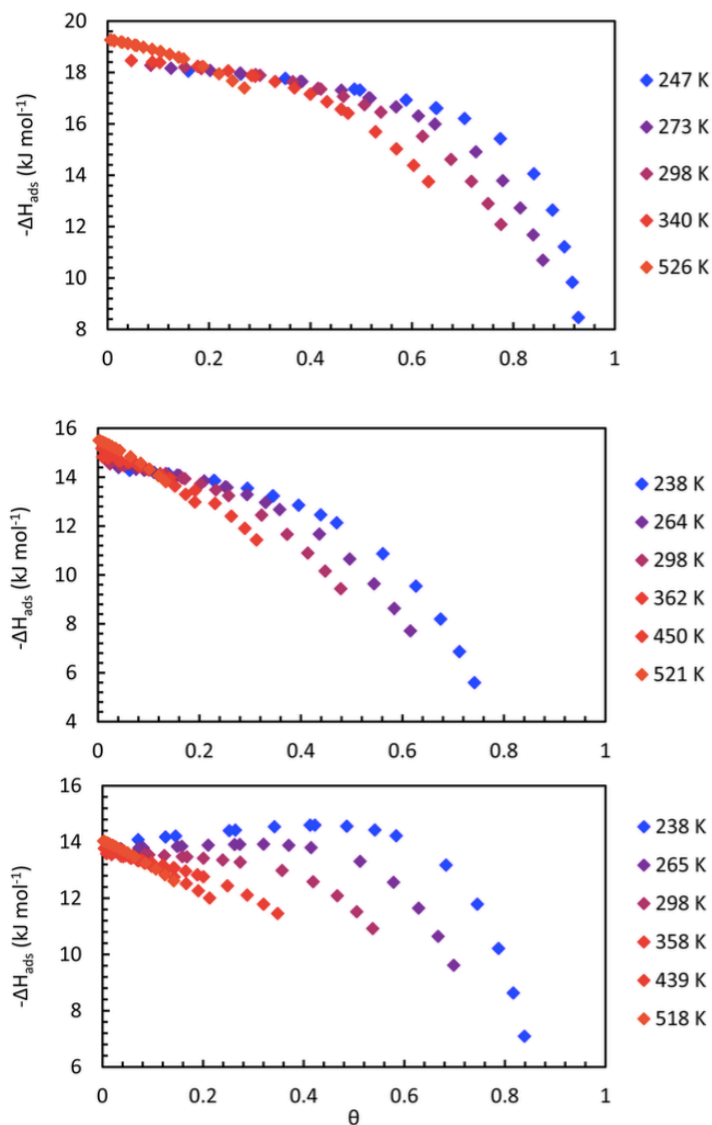


Figure 2. The isosteric heats of methane adsorption on CNS-201 (top), MSC-30 (middle), and ZTC (bottom) as a function of temperature and fractional site occupancy (θ).

The isosteric enthalpy of adsorption is the molar change in enthalpy of the adsorptive species upon adsorption. While adsorption is an exothermic process, the isosteric heat of adsorption is reported as a positive quantity by convention, as shown in Figure 2. These curves were obtained by applying the Clapeyron relationship to the dual-Langmuir fits. It is necessary to use the general form of the Clapeyron relationship for methane adsorption at high pressure

because of the significant nonideality of methane gas-state properties. Its derivation and explanation with respect to the ideal-gas form of the equation are given in Chapter 3.

The Henry's Law value of adsorption heat, $-AH_\theta$, is calculated by extrapolating the heat of adsorption to zero pressure. The Henry's law values for CNS-201, MSC-30, and ZTC-3 are 18.1-19.3, 14.4-15.5, and 13.5-14.2 kJ mol⁻¹, respectively. The isosteric heats of methane adsorption as a function of fractional occupancy, θ , in the activated carbons (CNS-201 and MSC-30) are typical of other carbon materials, with the isosteric heats decreasing with θ . In the range $0 < \theta < 0.6$, the more graphitic CNS-201 shows a more gradual decrease of isosteric heat than MSC-30, indicative of more heterogeneous site energies in MSC-30. Surprisingly, the isosteric heat of adsorption in ZTC increases to a maximum at $\theta = 0.5-0.6$ at temperatures from 238 to 273 K. This increase is anomalous compared to previous experimental reports of methane adsorption on carbon.

This anomalous effect results from adsorbate-adsorbate intermolecular interactions, as suggested by theoretical work.^{6,7,8} We have reported similar effects for ethane (Chapter 6) and krypton (Chapter 7). Accurately assessing the contribution of intermolecular interactions to the isosteric heat requires knowledge of the adsorption binding-site energies. A heterogeneous distribution of site energies, as in MSC-30, is reflected in the relatively rapid decrease of the isosteric heat with θ . This behavior is common as the most favorable sites are filled first (on average). The material properties of ZTC, including a narrow distribution of pore width, periodic pore spacing, and high content of sp²-hybridized carbon, suggest a high degree of homogeneity of the binding-site energies. We expect that the measured increase of 0.5 kJ mol⁻¹ in the isosteric heat at 238K reflects most of the contribution from favorable intermolecular

interactions, and this increase is in good agreement with calculations of lateral interactions of methane molecules on a surface.^{6,7} An increasing isosteric heat, as seen with methane on ZTC, is highly desirable as it enhances deliverable storage capacity. This effect enables a larger fraction of the adsorption capacity at pressures above the lower bound of useful storage. Indeed, the deliverable gravimetric methane capacities of ZTC at temperatures near ambient are the highest of any reported carbonaceous material.

A clearer picture of adsorption thermodynamics can be achieved by evaluating the specific enthalpy of the adsorbed phase, as shown in Figure 3. This removes the gas-phase dependency of the isosteric heat and focuses solely on adsorbed-phase thermodynamics. This is particularly useful because at a constant temperature, it is a reasonable approximation that the specific properties of the adsorbed phase as a function of increasing site occupancy do not depend on contributions from internal (intramolecular) phenomena. Here, a decreasing enthalpy of the adsorbed phase as a function of uptake, as seen on ZTC, corresponds to an “increasing” (or, decreasing negative) isosteric heat of adsorption.

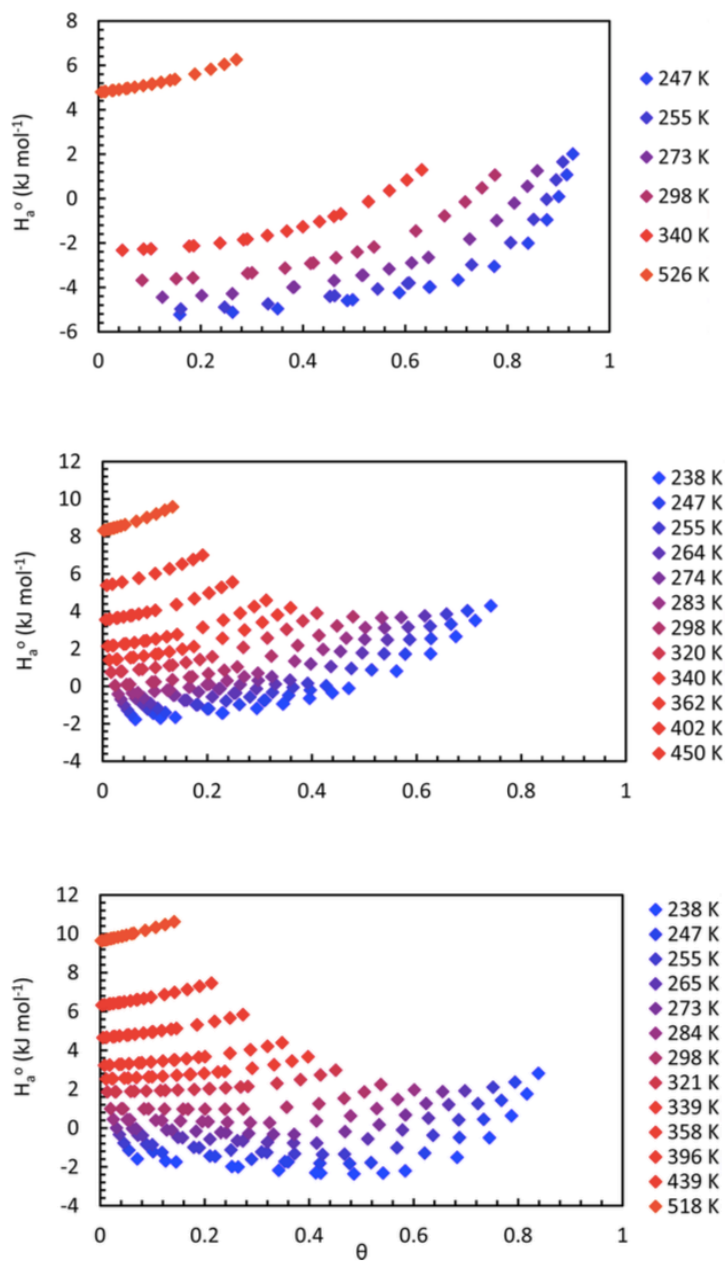


Figure 3. Adsorbed-phase enthalpy of CNS-201 (top), MSC-30 (middle), and ZTC (bottom) as a function of temperature and fractional occupancy (θ).

The adsorbed-phase entropy was determined in a similar manner that is described in more detail in Chapter 3. Adsorbed-phase entropy isotherms are shown in Figure 4. While all

three adsorbed phases show qualitatively similar entropies, a notable difference is seen between the smaller pore materials (CNS-201 and ZTC) and MSC-30, which has a significant fraction of pores of widths >2 nm. The molar entropy of methane adsorbed on CNS-201 and ZTC at 238 K approaches the value of the liquid reference state rather closely (within $12 \text{ J K}^{-1} \text{ mol}^{-1}$), indicating a liquid-like character of the adsorbed layer, unlike on MSC-30 (reaching a minimum of $22 \text{ J K}^{-1} \text{ mol}^{-1}$ at 238 K). We must note, however, the relatively arbitrary nature of the reference state; the entropy of saturated liquid CH_4 varies by $\sim 45 \text{ J K}^{-1} \text{ mol}^{-1}$ along its liquidus phase boundary.

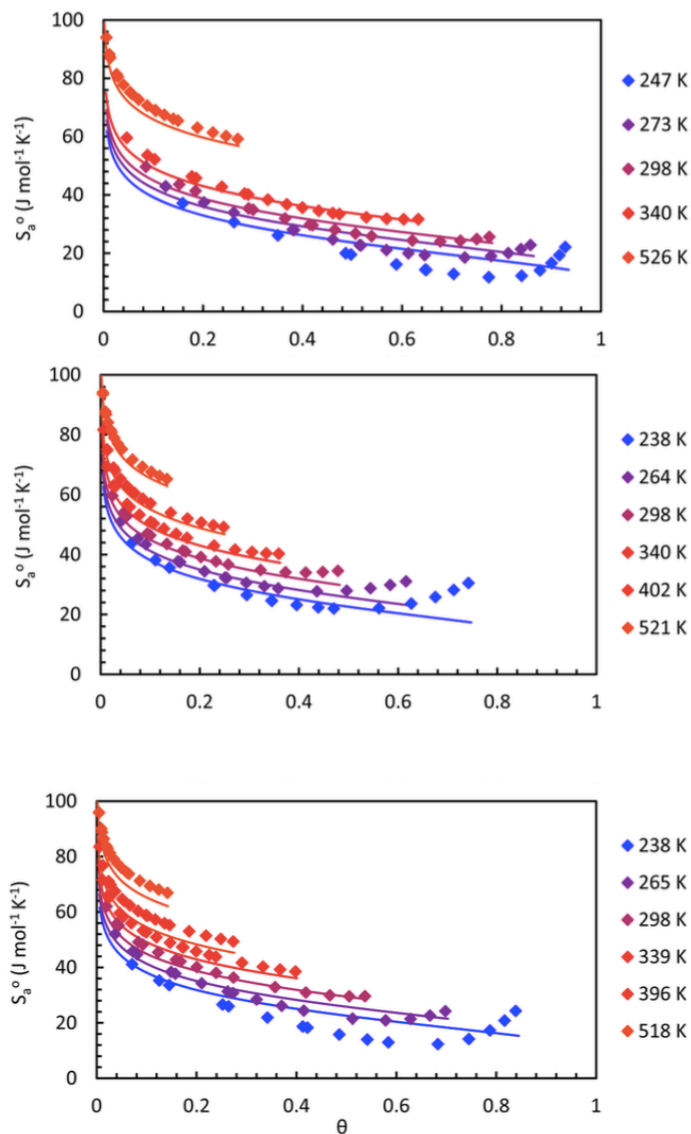


Figure 4. Adsorbed-Phase Entropy of methane on CNS-201 (top), MSC-30 (middle), and ZTC (bottom) as a function of temperature and fractional occupancy. Curves indicate corresponding statistical mechanics estimates.

For comparison, statistical mechanics calculations were carried out to independently estimate the adsorbed-phase entropy. The only experimental parameter used in the theoretical calculations was the material's specific surface area. A remarkable consistency between theory

and experiment is observed across all three adsorbents, especially in the limit of high temperature and low pressure where the approximations in the theoretical model are most justified⁹. Of particular note, the theoretical calculations very closely reproduce the measured molar entropies of the adsorbed phase on MSC-30, where the largest errors between $\theta = 0-0.2$ are $<3.5\%$ at all temperatures measured (see Figure 4). The agreement between experimental data and the statistical mechanical calculations for the adsorbed phase on CNS-201 is similarly close in the dilute limit, but strays significantly beyond $\theta = 0.35$. On ZTC, however, the estimated adsorbed-phase entropy exceeds measured values, especially at low temperatures and moderate coverage. This suggests the mechanism by which enhanced adsorbate-adsorbate interactions are promoted in the adsorbed phase on ZTC, namely clustered configurations.

For ZTC, confinement of an adsorbed phase in narrow pores is likely to lead to clustering as a result of enhanced lateral interactions. The formation of such clusters, or adsorbate “islands”, on an adsorbent surface due to attractive intermolecular interactions, is a well-known feature of physisorption of strongly interacting molecular species (e.g., methanol on indium-tin-oxide glass¹⁰) and moderately interacting molecular species (e.g., subcritical CO₂ on several MOFs and zeolites^{11, 12}) and also of chemisorption of fairly weakly interacting atomic species (e.g., oxygen on Pt(111)¹³). This clustering behavior results in a reduction in entropy due to the reduced number of accessible configurations of the cluster(s) in the same total number of sites. This is consistent with the reduced entropy measured for methane on ZTC as compared to the statistical mechanics estimate. The topic of clustering accounting for enhanced adsorbate-adsorbate interactions is investigated in more detail in Chapter 8.

As a general note, the entropies of methane adsorbed between 238 and 526 K on the

various carbon materials measured in this work are very high as compared to some historical theoretical estimates, approaching values of bulk gaseous methane in the dilute limit. In fact, this observation has recently been made across many materials and adsorbed molecular species.¹⁴ The ratio of adsorbed-phase entropy to the gas-phase entropy for CH₄ on MSC-30, for example, spans from 0.3 (at 238 K and 2 MPa) to 0.8 (at 0.1 MPa and 521 K), similar to the value reported for methane on graphite(0001) in the dilute limit: 0.76 at 55 K.^{14,15}

References:

1. Bowman, R. C.; Luo, C. H.; Ahn, C. C.; Witham, C. K.; Fultz, B. The Effect of Tin on the Degradation of LaNi₅-ySn Metal-Hydrides During Thermal Cycling. *J. Alloys Compd.* **1995**, *217*, 185-192.
2. Sun, Y.; Liu, C. M.; Su, W.; Zhou, Y. P.; Zhou, L. Principles of Methane Adsorption and Natural Gas Storage. *Adsorption.* **2009**, *15*, 133-137.
3. Dubinin, M. M.; Radushkevich, L. V. Equation of the Characteristic Curve of Activated Charcoal. *Proc. Acad. Sci. USSR Phys. Chem. Sect.* **1947**, *55*, 331-337.
4. Burevski, D. The Application of the Dubinin-Astakhov Equation to the Characterization of Microporous Carbons. *Colloid Polym. Sci.* **1982**, *260*, 623-627.
5. Lemmon, E. W.; Huber, M. L.; McLinden, M. O. *NIST Standard Reference Database 23: Reference Fluid Thermodynamic and Transport Properties-REFPROP*, Version 8.0 [CD-ROM], 2007.
6. Salem, M. M. K.; Braeuer, P.; von Szombathely, M.; Heuchel, M.; Harting, P.; Quitzsch, K.; Jaroniec, M. Thermodynamics of High-Pressure Adsorption of Argon, Nitrogen, and Methane on Microporous Adsorbents. *Langmuir.* **1998**, *14*, 3376-3389.
7. Sillar, K.; Sauer, J. Ab Initio Prediction of Adsorption Isotherms for Small Molecules in Metal-Organic Frameworks: The Effect of Lateral Interactions for Methane/CPO-27-Mg. *J. Am. Chem. Soc.* **2012**, *134*, 18354-18365.
8. Al-Muhtaseb, S. A.; Ritter, J. A. Roles of Surface Heterogeneity and Lateral Interactions on the Isothermic Heat of Adsorption and Adsorbed Phase Heat Capacity. *J. Phys. Chem. B.* **1999**, *103*, 2467-2479.
9. Stadie, N. P.; Murialdo, M.; Ahn, C. C.; Fultz, B. Unusual Entropy of Adsorbed Methane on Zeolite-Templated Carbon. *J. Phys. Chem. C* **2015**, *119*, 26409-26421.
10. Wang, L.; Song, Y. H.; Wu, A. G.; Li, Z.; Zhang, B. L.; Wang, E. K. Study of Methanol Adsorption on Mica, Graphite and ITO Glass by Using Tapping Mode Atomic Force Microscopy. *Appl. Surf. Sci.* **2002**, *199*, 67-73.
11. Krishna, R.; van Baten, J. A. Investigating Cluster Formation in Adsorption of CO₂, CH₄, and Ar in Zeolites and Metal Organic Frameworks at Subcritical Temperatures. *Langmuir.* **2010**, *26*, 3981-3992.
12. Krishna, R.; van Baten, J. M., Highlighting a Variety of Unusual Characteristics of Adsorption and Diffusion in Microporous Materials Induced by Clustering of Guest Molecules. *Langmuir.* **2010**, *26*, 8450-8463.
13. Parker, D. H.; Bartram, M. E.; Koel, B. E. Study of High Coverages of Atomic Oxygen on the Pt(111) Surface. *Surf. Sci.* **1989**, *217*, 489-510.
14. Campbell, C. T.; Sellers, J. R. V. The Entropies of Adsorbed Molecules. *J. Am. Chem. Soc.* **2012**, *134*, 18109-18115.
15. Tait, S. L.; Dohnalek, Z.; Campbell, C. T.; Kay, B. D. N-Alkanes on Pt(111) and on C(0001)/Pt(111): Chain Length Dependence of Kinetic Desorption Parameters. *J. Chem. Phys.* **2006**, *125*, 234308-1-15.

Chapter 6

Observation and Investigation of Increasing Isothermic Heat of Adsorption of Ethane on Zeolite-Templated Carbon

M. Murialdo, N.P. Stadie, C.C. Ahn, and B. Fultz, "Observation and Investigation of Increasing Isothermic Heat of Adsorption of Ethane on Zeolite-Templated Carbon," *J. Phys. Chem. C*, 119, 994 (2015).

DOI: 10.1021/jp510991y

<http://pubs.acs.org/doi/abs/10.1021/jp510991y>

Abstract

Ethane adsorption was measured on zeolite-templated carbon (ZTC) and compared to superactivated carbon MSC-30. Isotherms measured at temperatures between 252 and 423 K were fitted using a superposition of two Langmuir isotherms and thermodynamic properties were assessed. Unlike typical carbon adsorbents, the isothermic heat of adsorption on ZTC increases by up to 4.6 kJ mol^{-1} with surface coverage. This increase is attributed to strong adsorbate-adsorbate intermolecular interactions, a hypothesis that is shown to be consistent with fundamental estimates of intermolecular interactions. Furthermore, the molar entropy of the adsorbed phase was measured and compared to an estimate derived from statistical mechanics. While the measured and estimated entropies of the adsorbed phase of ethane on MSC-30 are in agreement, they differ significantly on ZTC at high coverage, indicative of the atypical properties of ethane adsorption on ZTC.

1. Introduction

Ethane is the second most abundant component in natural gas and an important petrochemical feedstock. It is a common reactant for the synthesis of ethylene, and its separation from natural gas has been an important process for many years. Currently, the separation of ethane from natural gas is predominantly carried out via cryogenic distillation, an energy intensive process.¹ Physisorption materials have been proposed as a more efficient separation solution.^{2,3,4} Physisorption materials also hold promise in improving the volumetric energy density of stored ethane.^{5,6} An understanding of ethane adsorption is thus essential for natural gas storage and separation processes.

Physisorption occurs when weak physical interactions between a solid adsorbent and a gas induce the formation of a locally densified adsorbate layer at the solid surface. This interaction depends sensitively on the surface chemistry and surface structure of the adsorbent.^{7,8,9,10} The isosteric heat of adsorption, q_{st} is often reported as a critical figure of merit for physisorption. This proxy measure of binding energy determines the equilibrium uptake quantity at finite temperatures and pressures.

Microporous carbons have gained significant attention as potential adsorbents due their light weight, low cost, and wide variability.^{11,12,13} However, these materials often exhibit binding energies that are below desired optimal values.^{14,15} Furthermore, the isosteric heat of adsorption typically decreases with surface coverage due to binding site heterogeneity, further reducing the deliverable gas storage capacity in the range of practicality for applications. We recently reported the observation of increasing isosteric heat of adsorption of methane on zeolite-templated carbon,¹⁶ a unique and anomalous behavior with respect to methane which typically has very weak intermolecular interactions. Recently, Yuan et al. reported the synthesis

of a mesoporous carbon wherein the isosteric heat of ethane adsorption increases as a function of coverage.¹⁷ This was attributed to favorable ethane-ethane intermolecular interactions and a relatively homogeneous adsorbent surface. While intriguing, the latter results have limited applications for gas storage and separation due to limitations of the mesoporous carbon in question. With an average pore width of 48 Å and a specific surface area of 599 m² g⁻¹, this mesoporous carbon has only a small total excess uptake capacity of ~2.5 mmol g⁻¹ at 278 K. This effect has not been investigated or observed for ethane adsorption on a *microporous* carbon with a large specific surface area, a system that would have superior potential for advanced applications. In this work, we report that a zeolite-templated carbon (ZTC) with a narrow distribution of pore widths centered at 12 Å and a large specific surface area of 3591 m² g⁻¹ exhibits an increasing isosteric heat of ethane adsorption as a function of coverage. This material has an exceptional uptake capacity of 22.8 mmol g⁻¹ (at 252K), owing to its very large surface area and optimized structural properties. Furthermore, several novel analysis methods including comparisons to methane adsorption, Lennard-Jones parameters and statistical mechanics calculations are implemented to corroborate and assist in the understanding of the phenomenon of increasing isosteric heat of adsorption.

2. Experimental Methods

2.1 Materials Synthesis

Two materials were chosen for comparison in this study: MSC-30 and ZTC. The superactivated carbon “Maxsorb” MSC-30 was obtained from Kansai Coke & Chemicals Company Ltd. (Japan). The zeolite-templated carbon (ZTC) was synthesized in a multistep process that was optimized to achieve high template fidelity of the product.¹⁸ The faujasite-

type zeolite NaY (obtained from Tosoh Corp., Japan) was impregnated with furfuryl alcohol which was subsequently polymerized at 150 °C, augmented by a propylene CVD step at 700 °C, and carbonized at 900 °C. The ZTC product was freed by dissolution of the zeolite template in HF. ZTC was confirmed to exhibit very high fidelity with the zeolite template and outstanding microporous periodicity by X-ray diffraction and transmission electron microscopy, described in detail elsewhere.¹⁶

2.2 Materials Characterization

Equilibrium nitrogen adsorption isotherms were measured at 77 K using a BELSORP-max volumetric instrument from BEL-Japan Inc. The Dubinin-Radushkevich (DR) method^{19,20} was employed to calculate micropore volumes and the Brunauer-Emmett-Teller (BET) method²¹ was used to calculate specific surface areas. Pore-size distributions were determined by non-local density functional theory (NLDFT) analysis implemented by software provided by Micromeritics Instrument Corp., and a carbon slit-pore model was utilized.²² Skeletal densities of the materials were determined by helium pycnometry. Finally, the Dumas method²³ was employed to determine the elemental composition (CHN) of MSC-30 and ZTC.²⁴

2.3 Measurements

Equilibrium ethane adsorption isotherms were measured on ZTC and MSC-30 at 9 temperatures between 252 and 423 K. Research grade ethane (99.999%) obtained from Matheson Tri-Gas Inc. was used in a custom Sieverts apparatus that was tested for accuracy up to 10 MPa.²⁵ The reactor containing the sample was held at a constant set temperature while the remaining gas manifold always remained at room temperature. For low temperature isotherms, the reactor was submerged in a circulated chiller bath leading to temperature

deviations no larger than ± 0.1 K. For high temperature isotherms, the reactor was encased in a copper heat exchanger and wrapped with insulating fiberglass-heating tape. A PID controller was used to maintain a constant temperature with fluctuations of less than ± 0.4 K. In both setups, the temperature was measured by K-type thermocouples placed in direct contact with the reactor. The manifold temperature was measured with a platinum resistance thermometer in contact with the outer wall of the manifold.

High-pressure measurements were made with an MKS Baratron (Model 833) pressure transducer. For degassing, vacuum pressures were ensured with a digital cold cathode pressure sensor (I-MAG, Series 423). The Sieverts apparatus is equipped with a molecular drag pump capable of achieving vacuum of 10^{-4} Pa. Each sample was degassed at 520 K under vacuum of less than 10^{-3} Pa prior to measurements. Multiple adsorption/desorption isotherms were measured to ensure reversibility, and errors between identical runs were less than 1%. Gas densities were determined using the REFPROP Standard Reference Database.²⁶

3. Results

3.1 Adsorbent Characterization

BET specific surface areas of ZTC and MSC-30 were found to be 3591 ± 60 and 3244 ± 28 m² g⁻¹, respectively. Likewise, both materials have similar DR micropore volumes: 1.66 mL g⁻¹ (ZTC) and 1.54 mL g⁻¹ (MSC-30). The distribution of the pore sizes, however, differs significantly between the two materials. ZTC was determined to have a uniform pore-size distribution centered at 12 Å (see Figure 1). Over 90% of the micropore volume of ZTC is contained in pores with widths between 8.5 and 20 Angstroms. MSC-30 exhibits a wide range of pore sizes from 6 to 35 Å. 40% of the pore volume of MSC-30 is contained in pore widths

greater than 21 Angstroms. Furthermore, while MSC-30, like most activated carbons, has a skeletal density of 2.1 g mL^{-1} , ZTC has an unusually low skeletal density of 1.8 g mL^{-1} (in agreement with other ZTCs).²⁴ This discrepancy can be explained by the significantly higher hydrogen content found in ZTC by elemental analysis experiments. Hydrogen was found to account for 2.4% (by weight) of ZTC but only 1.2% of MSC-30.²⁴

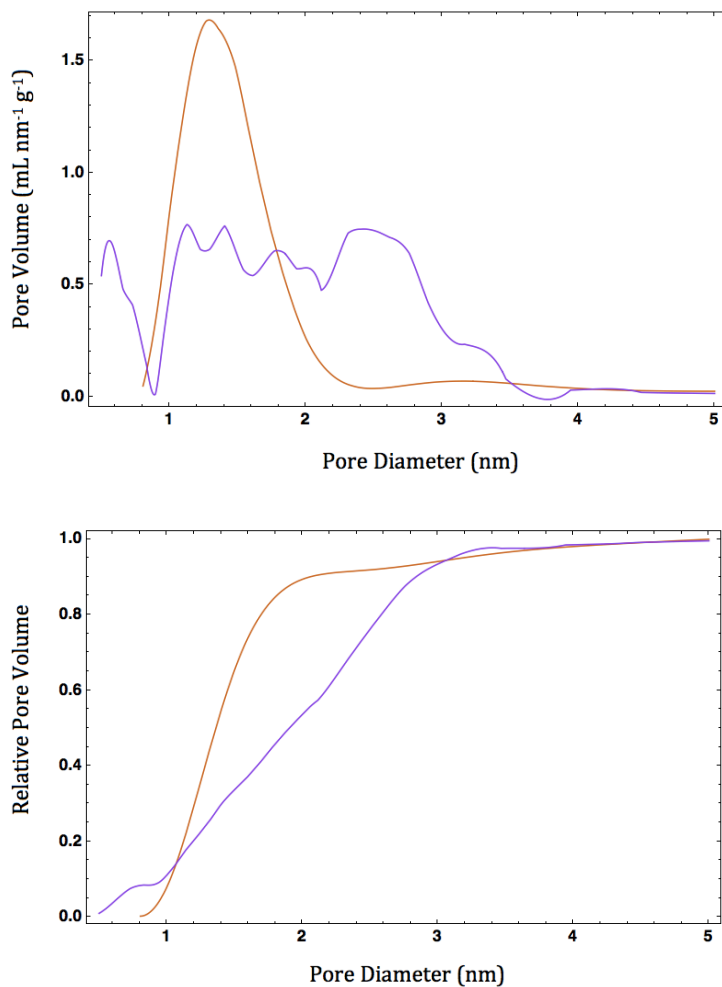


Figure 1. Pore-size distribution and relative pore volume of ZTC (orange) and MSC-30 (purple).

3.2 Adsorption Measurements:

Equilibrium ethane adsorption isotherms were measured at 9 temperatures between 252 and 423K and at pressures of up to 32 bar (see Figure 2). The maximum excess adsorption quantities measured on ZTC and MSC-30 (at ~253K) were 22.8 and 26.8 mmol g⁻¹, respectively. At room temperature (297K), the maximum uptake quantities measured on ZTC and MSC-30 were 19.2 and 22.1 mmol g⁻¹, respectively. Thus at both temperatures, MSC-30 exhibits greater excess adsorption capacities, with differences between the maximums being less than 15%. This is in contrast to methane adsorption on the same two materials, where ZTC exhibited higher excess adsorption capacities than MSC-30 at low temperatures.¹⁶ Moreover, the differences in excess adsorption capacities between the two materials are smaller (less than 5%) for methane adsorption.

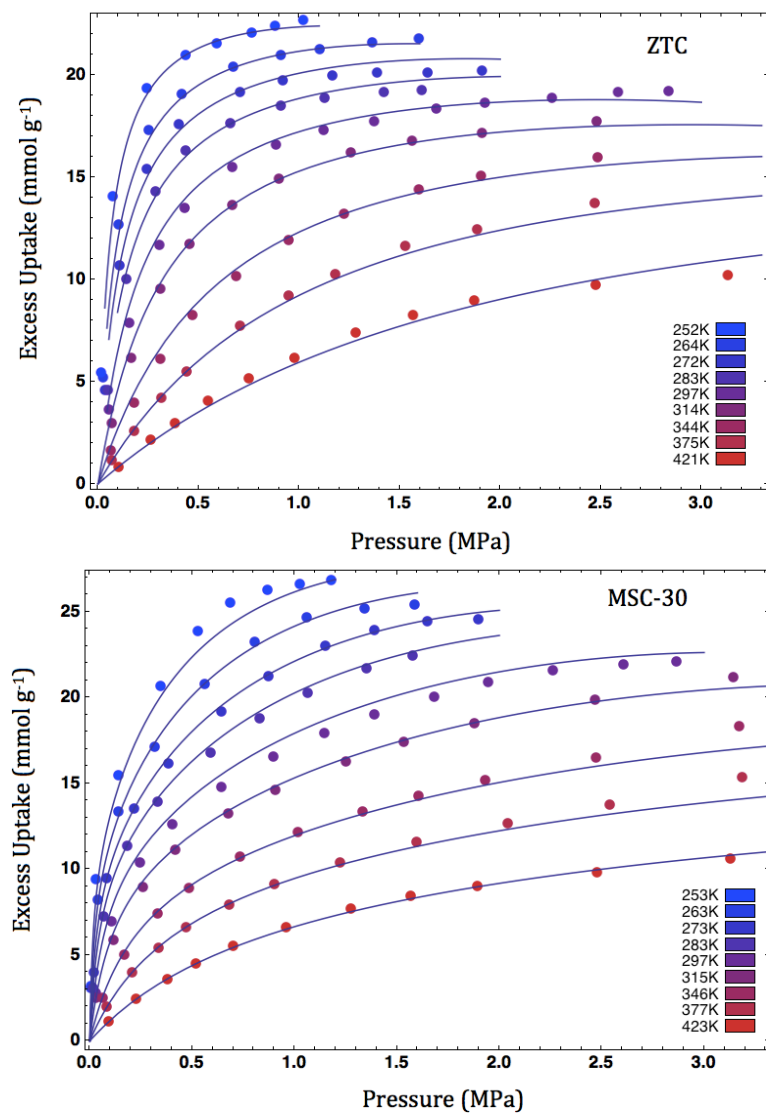


Figure 2. Equilibrium excess adsorption isotherms of ethane on ZTC and MSC-30. The lines indicate the best-fit analysis using a superposition of two Langmuir isotherms.

4. Discussion

4.1 Fitting Methodology

Thermodynamic analysis of adsorption requires interpolation of the adsorption data points, generally with a fitting function. It is common in literature to assume that the excess

adsorption well approximates the absolute adsorption. This assumption, while valid at low pressures and high temperatures, is invalid at temperatures near the critical point, particularly in high-pressure studies. To determine the absolute adsorption quantities and avoid the well-documented errors associated with equating excess adsorption and absolute adsorption, we follow a method initially described by Mertens.²⁷ We extend this method by modifications for the nonideal gas regime.¹⁶

The Gibbs excess adsorption²⁸ (n_e) is a function of the bulk gas density (ρ):

$$n_e = n_a - V_a \rho \quad (1)$$

Determining the absolute adsorption quantity (n_a) is simplest when the volume of the adsorption layer (V_a) is known. We left V_a as an independent fitting parameter, and assessed it later. The measured excess adsorption quantities were fitted with a generalized (multi-site) Langmuir isotherm:

$$n_e(P, T) = (n_{max} - V_{max}\rho(P, T)) \left[\sum_i \alpha_i \frac{K_i P}{1 + K_i P} \right] \quad (2)$$

Excess adsorption and density are functions of pressure (P) and temperature (T). The independent fitting parameters in this fitting model are n_{max} , a scaling factor indicative of the maximum absolute adsorption, α_i , a weighting factor for the i^{th} Langmuir isotherm ($\sum_i \alpha_i = 1$), V_a which scales with coverage up to V_{max} (the maximum volume of the adsorption layer), and K_i , an equilibrium constant for the i^{th} Langmuir isotherm. The parameter K_i is defined by an Arrhenius-type equation:

$$K_i = \frac{A_i}{\sqrt{T}} e^{-E_i/RT} \quad (3)$$

Here, A_i is a prefactor and E_i is a binding energy associated with the i^{th} Langmuir isotherm. Using two superimposed isotherms ($i=2$), we obtained satisfactory results while limiting the number of independent fitting parameters to 7: n_{max} , V_{max} , α_1 , A_1 , A_2 , E_1 , and E_2 . For ZTC and MSC-30, accurate fits were obtained with residual mean square values of 0.21 and 0.13 (mmol g⁻¹)². These fits are shown in Figure 2 and the best-fit values of the fitting parameters are given in Table 1. For comparison, fitting parameters for methane adsorption on ZTC and MSC-30 were obtained using the same fitting procedure¹⁶, and are also shown in Table 1.

Table 1. Least-squares minimized fitting parameters of the excess adsorption isotherms of ethane on MSC-30 and ZTC described by a two-site Langmuir isotherm.

| | n_{max} | V_{max} | α_1 | A_1 | A_2 | E_1 | E_2 |
|-------------------|-----------|-----------|------------|------------------------------|-------------------------------|-----------|-----------|
| Ethane on ZTC | 25 mmol/g | 1.6 mL/g | 0.82 | 2.1E-7 K ^{1/2} /MPa | 0.044 K ^{1/2} /MPa | 41 kJ/mol | 18 kJ/mol |
| Ethane on MSC-30 | 36 mmol/g | 2.6 mL/g | 0.71 | 0.086 K ^{1/2} /MPa | 0.0065 K ^{1/2} /MPa | 20 kJ/mol | 18 kJ/mol |
| Methane on ZTC | 36 mmol/g | 2.0 mL/g | 0.46 | 0.059 K ^{1/2} /MPa | 0.00018 K ^{1/2} /MPa | 12 kJ/mol | 20 kJ/mol |
| Methane on MSC-30 | 41 mmol/g | 2.3 mL/g | 0.70 | 0.068 K ^{1/2} /MPa | 0.0046 K ^{1/2} /MPa | 13 kJ/mol | 13 kJ/mol |

Many of the independent fitting parameters in this method have physical significance. For example, n_{max} represents the maximum specific absolute adsorption of the system. If the entire micropore volume of the material is assumed to be completely filled at this condition, then it follows that it should be approximately comparable to the value obtained by multiplying the density of the liquid phase of the adsorbate by the total micropore volume.

Using the density of liquid ethane and liquid methane near the triple point,²⁶ the maximum possible adsorption quantities estimated in this simplified way for ethane and methane on MSC-30 are 33 and 43 mmol g⁻¹, respectively. These values are within 10% of the n_{max} values determined through fitting. For ethane and methane adsorption on ZTC, the estimated and fitted values of n_{max} both deviate more significantly, with estimated values greater by 44% and 32% respectively.

The V_{max} parameter approximates the maximum volume of the adsorbed layer. Dividing by surface area, this gives an average width for the adsorbed layer. For ethane and methane adsorption on ZTC, this gives average adsorbed layer widths of 4.5 and 5.5 Å, both of which are in agreement with the measured ZTC micropore half-width of 6 Å. This suggests fairly effective filling of the ZTC micropores. Likewise, the ethane and methane V_{max} parameters on MSC-30 give adsorbed layer widths of 8 and 7 Å, which are in agreement with the average measured micropore half-width, 7 Å. Furthermore, for ethane on ZTC, V_{max} equals 1.6 mL g⁻¹, which is in good agreement with the micropore volume measured using the DR method and nitrogen isotherms, 1.66 mL g⁻¹. The V_{max} values for ethane on MSC-30 and methane on both materials deviate more significantly from measured DR micropore volumes with discrepancies of up to 41%. This, however, is not unexpected as different adsorbates with differing size and shape are confined and adsorbed in micropores distinctly.

4.2 Isothermic Enthalpy of Adsorption

The isothermic enthalpy of adsorption (ΔH_{adv}) is a widely used figure of merit that is indicative of the strength of binding interactions at a fixed temperature, pressure, and coverage. Typically it is determined using the isothermic method and reported as a positive value,

q_{st} the so-called isosteric heat (a convention that is followed herein), defined according to the Clapeyron equation:

$$q_{st} = -\Delta H_{ads} = -T \left(\frac{\partial P}{\partial T} \right)_{n_a} (\Delta v_{ads}) \quad (4)$$

The molar change in volume of the adsorbate upon adsorption (Δv_{ads}) is given by the difference between the gas-phase molar volume and $\frac{V_{max}}{n_{max}}$. The fitting method used in this work is especially convenient for thermodynamic calculations with the Clapeyron equation because the generalized Langmuir equation with $i=2$ can be analytically differentiated.²⁷ The isosteric heats of adsorption of ethane on ZTC and MSC-30 calculated in this way are shown in Figure 3.

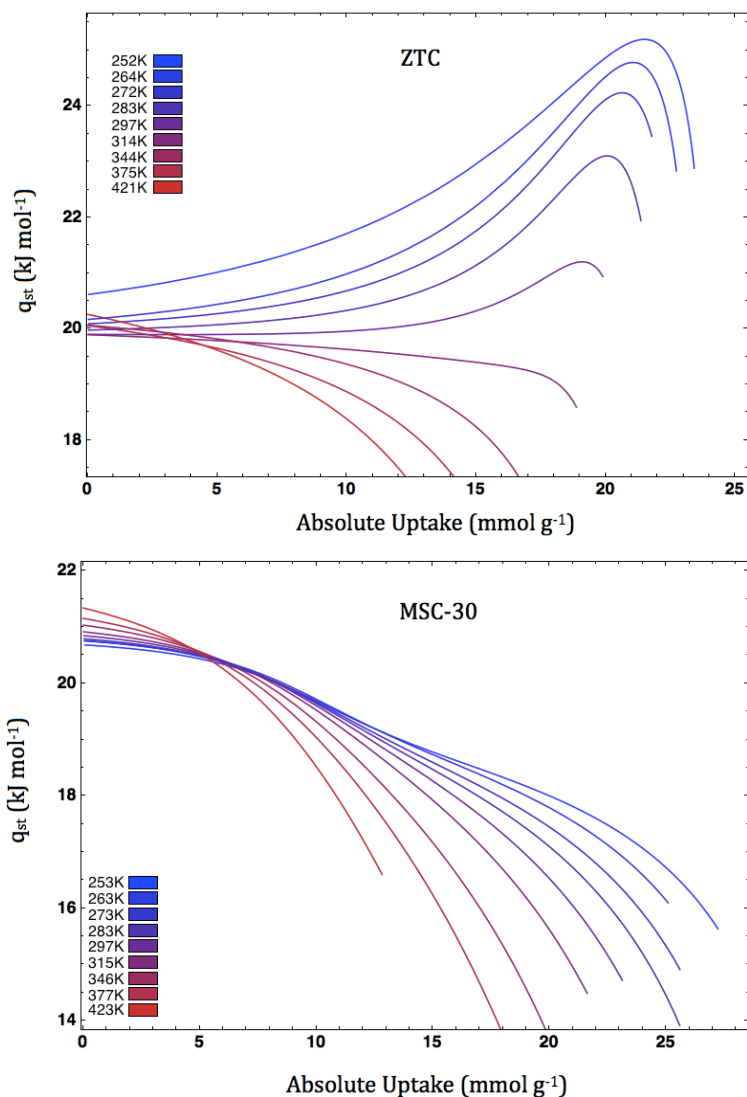


Figure 3. Isosteric heats of ethane adsorption on ZTC and MSC-30.

It can be observed that the isosteric heat of adsorption of ethane on ZTC increases as a function of coverage while MSC-30 (and a majority of other known systems) exhibits the typical decreasing isosteric heat with coverage (in this case represented as the absolute uptake quantity). This effect is most pronounced at low temperatures where the isosteric heat rises by 4.6 kJ mol^{-1} above its Henry's Law value of 20.6 kJ mol^{-1} (at 252 K). This effect (an increasing isosteric heat of adsorption) has also been observed for methane adsorption on the same material (ZTC)¹⁶ and is dependent on gas properties as well as structural and surface properties

of the adsorbent. In particular, the effect is expected to increase with the strength of intermolecular interactions of the adsorbate when adsorbate molecules are on nanostructured surfaces that promote intermolecular interactions. ZTC is an ideal candidate adsorbent for observing such a phenomenon due to its uniform pore-size distribution with pore widths centered at 12 Å and homogeneous chemical nature²⁴.

In the absence of intermolecular interactions and binding site heterogeneity, the isosteric heat should be constant at all coverages and temperatures. The increase in isosteric heat (as a function of coverage) reported in this work is hypothesized to result from attractive intermolecular interactions between ethane molecules. Assuming random site occupancy in the low coverage regime (e.g. less than 50% of the available sites filled), the probability of any site being occupied is equal to the fractional site occupancy, θ . If z is the number of nearest neighbor adsorption sites, on average an adsorbate molecule will have $z\theta$ occupied nearest neighbor adsorption sites. By assuming that nearest neighbor interactions have a binding energy of ε and higher order neighbors have a negligible binding energy, the average adsorbate-adsorbate binding energy per molecule, ξ , is given:

$$\xi = \frac{z\theta\varepsilon}{2} \quad (5)$$

Taking the derivative of ξ with respect to θ gives the estimated slope of the isosteric heat as a function of coverage (resulting from adsorbate-adsorbate interactions):

$$\frac{\partial(\xi)}{\partial\theta} = \frac{z\varepsilon}{2} \quad (6)$$

The Lennard-Jones parameter ε (which describes the well depth of the Lennard-Jones 12-6 interaction potential) is 1.7 kJ mol⁻¹ for ethane-ethane interactions²⁹. For adsorbed molecules on a two-dimensional surface the number of nearest neighbor adsorption sites, z , is posited to

be 4. This results in an estimated slope for ethane on ZTC of 3.4 kJ mol^{-1} . The average slope of the measured isosteric heat of adsorption of ethane on ZTC (Figure 3) has a similar value of 3.3 kJ mol^{-1} (at the lowest measured temperature 252K, up to 50% coverage). Interestingly, these measured and estimated slopes are of a similar magnitude to the slope of the isosteric heat of ethane adsorption on the mesoporous carbon of Yuan et al. ($\sim 4\text{-}5 \text{ kJ mol}^{-1}$ at $\sim 298\text{K}$).¹⁷

This very simple model (Equation 6) also gives a reasonable estimate for the increase in the isosteric heat of methane adsorption on ZTC. Here, ϵ for methane-methane interactions is 1.2 kJ mol^{-1} ,²⁹ giving a predicted slope of 2.4 kJ mol^{-1} . This is in agreement with the measured slope of 2.2 kJ mol^{-1} (up to 50% coverage at 255K).¹⁶ It is important to note that $z=4$, while intuitively reasonable, is a posited value. The true value of z is difficult, if not impossible, to obtain, and likely varies for different gases.

A number of metrics suggest that ethane has stronger attractive intermolecular interactions than methane by a factor of ~ 1.4 to 1.6 . These metrics include Lennard-Jones potential (adsorbate-adsorbate) well depth, boiling point, and critical temperature, and are shown in Table 2.

Table 2. Gas properties of ethane and methane and their ratios.

| | ethane | methane | ratio |
|----------------------------|---------------------------|---------------------------|--------|
| ϵ (Lennard-Jones) | 1.7 kJ/mol^{29} | 1.2 kJ/mol^{29} | 1.4 |
| Boiling Point (1 atm) | 184.57 K^{26} | 111.67 K^{26} | 1.6528 |
| Critical Temperature | 305.32 K^{26} | 190.56 K^{26} | 1.6022 |

In agreement with the ratios in Table 2, the ratio of the slopes of the ethane and methane heats of adsorption (as a function of coverage) on ZTC is 1.5. Stronger

intermolecular interactions within ethane correspond to an isosteric heat that increases more steeply than methane on the same material. Furthermore, the average Henry's Law values (zero coverage limit) of the isosteric heat were determined to be 20 and 21 kJ mol⁻¹ for ethane on ZTC and MSC-30, respectively, and 14 and 15 kJ mol⁻¹ for methane. For both ZTC and MSC-30, these ratios of Henry's law values are 1.4 for ethane and methane.

4.3 Entropy

At equilibrium, the Gibbs free energy of the adsorbed phase (G_a) equals the Gibbs free energy of the gas phase (G_g). The isosteric entropy of adsorption (ΔS_{ads}) is

$$\Delta G_{ads} = G_a - G_g = \Delta H_{ads} - T\Delta S_{ads} = 0 \quad (7)$$

$$\Delta S_{ads} = \frac{\Delta H_{ads}}{T} \quad (8)$$

The isosteric entropy of adsorption is the change in entropy of the adsorbate upon adsorption and the measured values for ethane adsorption on MSC-30 and ZTC are shown in Figure 4 (reported as positive values).

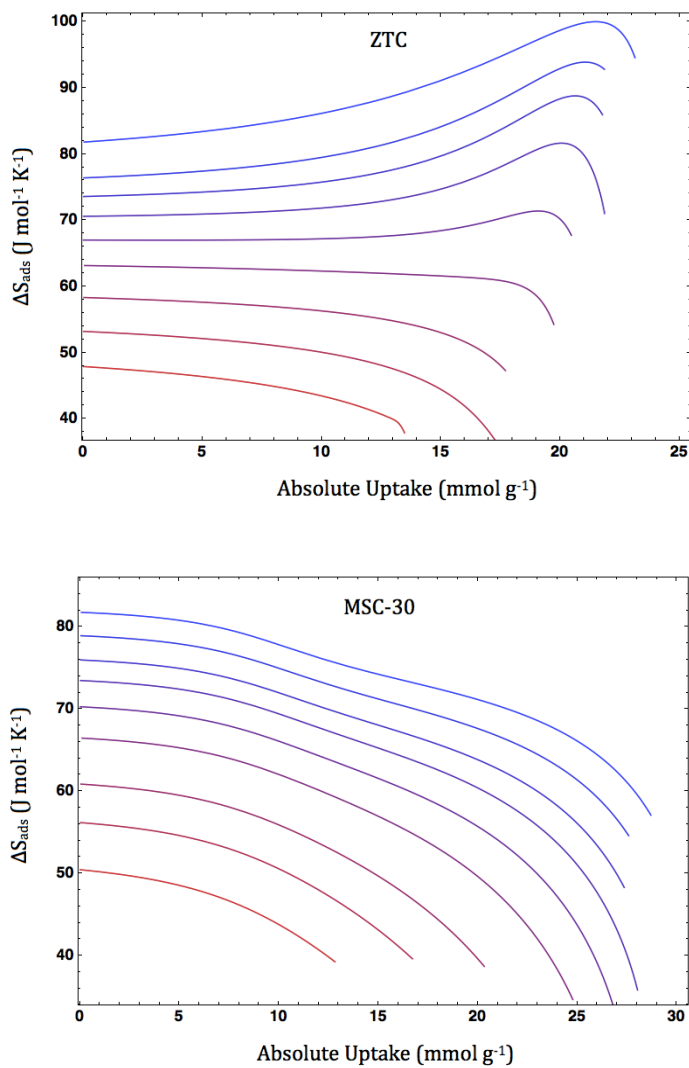


Figure 4. The isosteric entropy of ethane adsorption on ZTC and MSC-30 between 252 and 423 K.

By adding the isosteric entropy of adsorption to the gas-phase entropy (from Refprop²⁶) we obtain the molar entropy of the adsorbed phase (Figure 5).

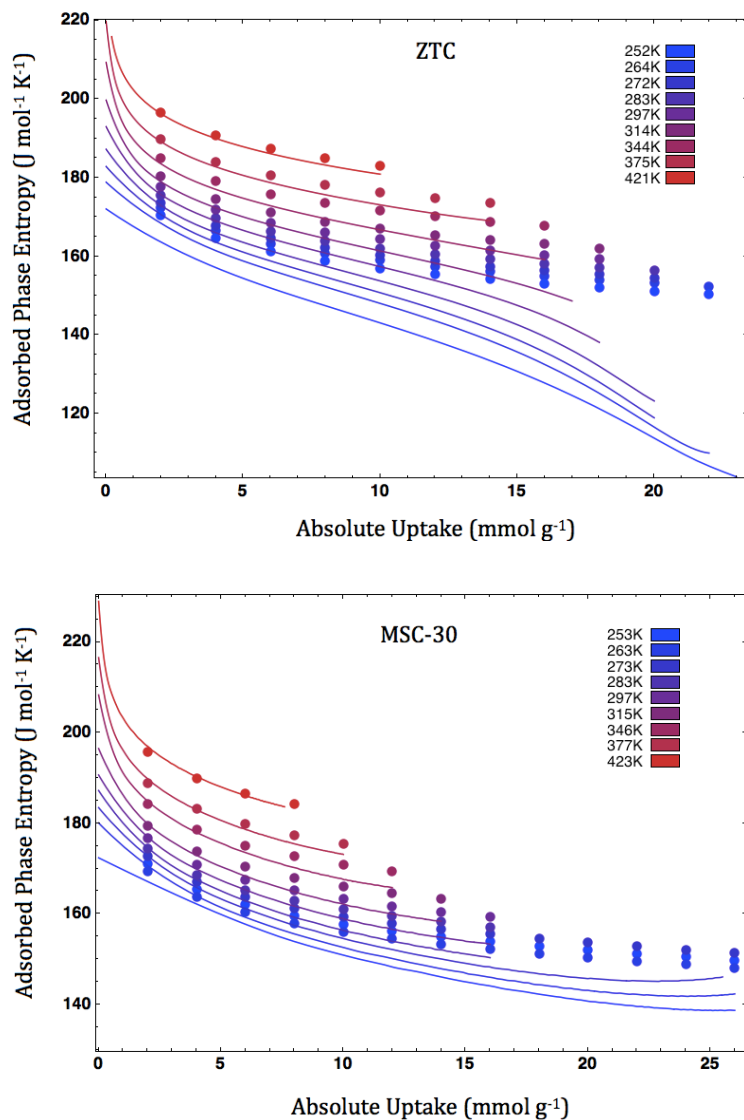


Figure 5. The molar adsorbed-phase entropies of ethane on ZTC and MSC-30. The curves indicate measured data and the points are calculated values (from statistical mechanics).

4.4 Statistical Mechanics

For comparison, the adsorbed-phase molar entropies were also calculated using statistical mechanics. Adsorbed ethane has numerous entropic contributions including vibrational, rotational, and configurational components. Each contribution was accounted for

as follows using standard partition functions and established values for characteristic frequencies. The effects of intermolecular interactions between the adsorbed molecules were not included, and the resulting discrepancies are discussed following the analysis.

Ethane in the gas phase has 12 internal vibrational modes with well-known characteristic vibrational frequencies and degeneracies,³⁰ and minimal changes in these frequencies are expected upon adsorption. Near ambient temperature, these vibrational modes are of little significance to the adsorbed-phase entropy, but their influence increases with temperature (see Figure 6). The partition function for vibrational modes ($q_{vib\ i}$) is:

$$q_{vib\ i}(T) = \frac{e^{-\Theta_{vib\ i}/2T}}{1 - e^{-\Theta_{vib\ i}/T}} \quad (9)$$

Here, $\Theta_{vib\ i}$ is the characteristic vibrational temperature of the i^{th} vibrational mode.

Adsorbed gases also vibrate with respect to the adsorbent surface. While the partition function for these vibrations is also given by Equation 9, the characteristic frequency is not readily accessible. Instead we have estimated these characteristic harmonic frequencies by

$$\nu = \left(\frac{1}{2\pi}\right) \sqrt{\frac{K}{m}} \quad (10)$$

Here K is the force constant and m is the molecular mass (of ethane). For simplicity (in the absence of detailed knowledge of the adsorbent surface geometry) the adsorbate-adsorbent potential was modeled as a Lennard-Jones potential with ϵ given by the average Henry's law value of the isosteric heat per molecule. For a Lennard-Jones potential, the force constant and frequency are:

$$K = \frac{72\epsilon}{r_m^2} \quad (11)$$

$$\nu = \left(\frac{1}{2\pi}\right) \sqrt{\frac{72\varepsilon}{m(r_m)^2}} \quad (12)$$

Here r_m is the distance wherein the potential reaches its minimum. Rotationally, ethane is a symmetric top with characteristic frequencies $\Theta_{\text{rota}} = \Theta_{\text{rotb}} = 0.953\text{K}$, $\Theta_{\text{rotc}} = 3.85\text{K}$.³¹ For ethane, the high temperature approximation of the partition function for the rotational modes (q_{rot}) is:

$$q_{\text{rot}} = \frac{\pi^2}{6} \left(\frac{T}{\Theta_{\text{rota}}}\right) \left(\frac{T}{\Theta_{\text{rotc}}}\right)^{\frac{1}{2}} \quad (13)$$

The configurational entropy of the adsorbed phase was determined using the partition function:

$$q_{\text{con}} = \left(\frac{\lambda}{\Lambda^2}\right)^{n_a} \quad (14)$$

Here λ is specific surface area divided by specific absolute uptake, and Λ is the thermal de Broglie wavelength. Using the partition functions above, individual entropy contributions were calculated by taking the negative temperature derivative of the Helmholtz free energy. These individual contributions were summed to obtain the total molar entropy of the adsorbed phase (shown in Figure 5). The relative contributions from each component to the total entropy at a representative fixed adsorption quantity are shown in Figure 6.

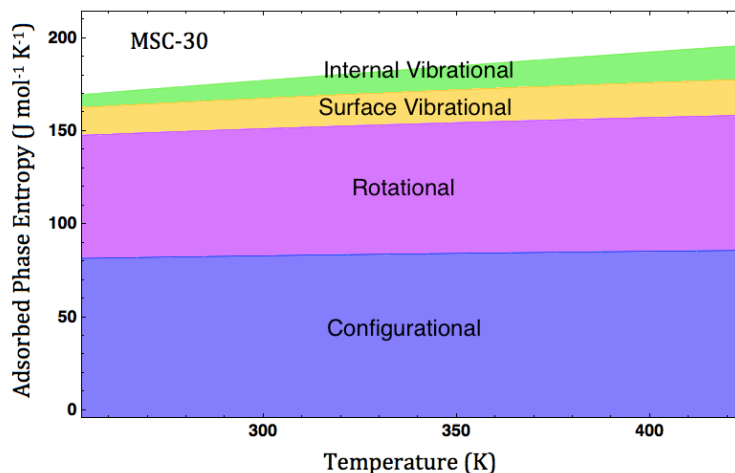


Figure 6. Relative contributions of each component to the total adsorbed-phase entropy of ethane on MSC-30 at the absolute uptake value of 2 mmol g^{-1} .

As shown in Figure 5, there is good agreement between the measured and calculated values of the adsorbed-phase entropy of ethane on MSC-30. Errors are less than 10% (without applying any fitting or offset) throughout the measured regime, and are especially low at high temperatures. At high coverages the measured entropy of ethane on MSC-30 gradually levels out, but maintains positive concavity. In contrast, the measured entropy of ethane adsorbed on ZTC deviates significantly from calculated values. At high temperatures, the measured entropy is in agreement with the calculation from statistical mechanics, as in MSC-30. However, at low temperatures and high coverages, the measured entropy is well below the calculated value (with discrepancies of up to 42%). This is associated with the increase in isosteric heat in this regime; ethane adsorption on ZTC has an anomalously increasing isosteric heat, and likewise an anomalously decreasing entropy in the adsorbed phase. This is expected to be caused by enhanced adsorbate-adsorbate interactions on the surface of ZTC. Stronger intermolecular interactions correspond to stiffer vibrational modes, hindered rotational motion, and inhibited

molecular motion/rearrangement, all of which can lead to a decrease in the entropy of the adsorbed phase.

The increase in isosteric heat above the Henry's Law value is largest at low temperatures. We expect that temperature will disrupt the adsorbate-adsorbate lateral interactions, suppressing the increase in isosteric heat. The thermal behavior may be a cooperative one, where the loss of lateral interactions makes other lateral interactions less favorable. There appears to be a critical temperature around 300 K where the effect of lateral interactions between ethane molecules is lost.

5. Conclusions

Ethane adsorption was measured on a zeolite-templated carbon material (ZTC) that has an exceptionally high surface area and narrow and uniform microporosity. An increasing isosteric heat of adsorption as a function of coverage was observed. The isosteric heat rises by 4.6 kJ mol^{-1} from a Henry's law value of 20.6 kJ mol^{-1} at low coverage to a peak of 25.2 kJ mol^{-1} at a coverage of 21.4 mmol g^{-1} . By comparing ethane adsorption on ZTC to methane adsorption on the same material, it was found that the slope of the isosteric heat of adsorption with coverage approximately scales with the strength of the adsorbate-adsorbate intermolecular interactions. A control material, superactivated carbon MSC-30, behaved as a normal microporous carbon adsorbent, exhibiting a monotonically decreasing isosteric heat with coverage. The measured adsorbed-phase entropy of ethane on MSC-30 was also successfully estimated with a statistical mechanics based approach (without intermolecular interactions), exhibiting discrepancies of less than 10%. The measured entropy of ethane adsorbed on ZTC deviated significantly from this standard model prediction at high coverage

and low temperature, indicating atypical adsorption properties in this system. The behavior of both the adsorbed-phase entropy and the isosteric heat of ethane on ZTC can be explained by attractive adsorbate-adsorbate interactions promoted by the nanostructured surface of ZTC.

References:

1. Magnowski, N. B. K.; Avila, A. M.; Lin, C. C. H.; Shi, M.; Kuznicki, S. M. Extraction of Ethane from Natural Gas by Adsorption on Modified ETS-10. *Chem. Eng. Sci.* **2011**, *66*, 1697-1701.
2. Sircar, S. Pressure Swing Adsorption. *Ind. Eng. Chem. Res.* **2002**, *41*, 1389-1392.
3. Sircar, S. Basic Research Needs for Design of Adsorptive Gas Separation Processes. *Ind. Eng. Chem. Res.* **2006**, *45*, 5435-5448.
4. Tan, Z.; Gubbins, K. E. Selective Adsorption of Simple Mixtures in Slit Pores - A Model of Methane Ethane Mixtures in Carbon. *J. Phys. Chem.* **1992**, *96*, 845-854.
5. Jiang, S. Y.; Zollweg, J. A.; Gubbins, K. E. High-Pressure Adsorption of Methane and Ethane in Activated Carbon and Carbon-Fibers. *J. Phys. Chem.* **1994**, *98*, 5709-5713.
6. Amora, M. R., Jr.; Canabrava, D. V.; Bastos-Neto, M.; Torres, A. E. B.; Cavalcante, C. L., Jr.; Azevedo, D. C. S. Equilibrium Adsorption of Binary Mixtures of Light Hydrocarbons in Activated Carbon. *Lat. Am. Appl. Res.* **2009**, *39*, 153-156.
7. Xia, Y.; Walker, G. S.; Grant, D. M.; Mokaya, R. Hydrogen Storage in High Surface Area Carbons: Experimental Demonstration of the Effects of Nitrogen Doping. *J. Am. Chem. Soc.* **2009**, *131*, 16493-16499.
8. Goj, A.; Sholl, D. S.; Akten, E. D.; Kohen, D. Atomistic Simulations of CO₂ and N₂ Adsorption in Silica Zeolites: The Impact of Pore Size and Shape. *J. Phys. Chem. B* **2002**, *106*, 8367-8375.
9. Coasne, B.; Pellenq, R. J. M. Grand Canonical Monte Carlo Simulation of Argon Adsorption at the Surface of Silica Nanopores: Effect of Pore Size, Pore Morphology, and Surface Roughness. *J. Chem. Phys.* **2004**, *120*, 2913-2922.
10. Lozano-Castello, D.; Cazorla-Amoros, D.; Linares-Solano, A.; Quinn, D. F. Influence of Pore Size Distribution on Methane Storage at Relatively Low Pressure: Preparation of Activated Carbon with Optimum Pore Size. *Carbon* **2002**, *40*, 989-1002.
11. Alcaniz-Monge, J.; Lozano-Castello, D.; Cazorla-Amoros, D.; Linares-Solano, A. Fundamentals of Methane Adsorption in Microporous Carbons. *Micropor. Mesopor. Mat.* **2009**, *124*, 110-116.
12. Panella, B.; Hirscher, M.; Roth, S. Hydrogen Adsorption in Different Carbon Nanostructures. *Carbon* **2005**, *43*, 2209-2214.
13. Poirier, E.; Chahine, R.; Bose, T. K. Hydrogen Adsorption in Carbon Nanostructures. *Int. J. Hydrogen Energ.* **2001**, *26*, 831-835.
14. Bhatia, S. K.; Myers, A. L. Optimum Conditions for Adsorptive Storage. *Langmuir* **2006**, *22*, 1688-1700.
15. Mason, J. A.; Veenstra, M.; Long, J. R. Evaluating Metal-Organic Frameworks for Natural Gas Storage. *Chem. Sci.* **2014**, *5*, 32-51.
16. Stadie, N. P.; Murialdo, M.; Ahn, C. C.; Fultz, B. Anomalous Isosteric Enthalpy of Adsorption of Methane on Zeolite-Templated Carbon. *J. Am. Chem. Soc.* **2013**, *135*, 990-993.

17. Yuan, B.; Wu, X.; Chen, Y.; Huang, J.; Luo, H.; Deng, S. Adsorptive Separation Studies of Ethane-Methane and Methane-Nitrogen Systems Using Mesoporous Carbon. *J. Colloid Interface Sci.* **2013**, *394*, 445-450.
18. Nishihara, H.; Hou, P.-X.; Li, L.-X.; Ito, M.; Uchiyama, M.; Kaburagi, T.; Ikura, A.; Katamura, J.; Kawarada, T.; Mizuuchi, K.; Kyotani, T. High-Pressure Hydrogen Storage in Zeolite-Templated Carbon. *J. Phys. Chem. C* **2009**, *113*, 3189-3196.
19. Dubinin, M. M.; Radushkevich, L. V. Equation of the Characteristic Curve of Activated Charcoal. *Proc. Acad. Sci. USSR Phys. Chem. Sect.* **1947**, *55*, 331-337.
20. Nguyen, C.; Do, D. D. The Dubinin-Radushkevich Equation and the Underlying Microscopic Adsorption Description. *Carbon* **2001**, *39*, 1327-1336.
21. Brunauer, S.; Emmett, P. H.; Teller, E. Adsorption of Gases in Multimolecular Layers. *J. Am. Chem. Soc.* **1938**, *60*, 309-319.
22. Tarazona, P.; Marconi, U. M. B.; Evans, R. Phase-Equilibria of Fluid Interfaces and Confined Fluids - Nonlocal Versus Local Density Functionals. *Mol. Phys.* **1987**, *60*, 573-595.
23. Dumas, J. B. A Method of Estimating Nitrogen in Organic Material. *Ann. Chim. Phys.* **1833**, *58*, 171-173.
24. Stadie, N. P.; Vajo, J. J.; Cumberland, R. W.; Wilson, A. A.; Ahn, C. C.; Fultz, B. Zeolite-Templated Carbon Materials for High-Pressure Hydrogen Storage. *Langmuir* **2012**, *28*, 10057-10063.
25. Bowman, R. C.; Luo, C. H.; Ahn, C. C.; Witham, C. K.; Fultz, B. The Effect of Tin on the Degradation of LANI5-YSNY Metal-Hydrides During Thermal Cycling. *J. Alloys Compd.* **1995**, *217*, 185-192.
26. Lemmon, E. W.; Huber, M. L.; McLinden, M. O. *NIST Standard Reference Database 23: Reference Fluid Thermodynamic and Transport Properties-REFPROP*, Version 8.0 [CD-ROM], 2007.
27. Mertens, F. O. Determination of Absolute Adsorption in Highly Ordered Porous Media. *Surf. Sci.* **2009**, *603*, 1979-1984.
28. Sircar, S. Gibbsian Surface Excess for Gas Adsorption - Revisited. *Ind. Eng. Chem. Res.* **1999**, *38*, 3670-3682.
29. Tee, L. S.; Gotoh, S.; Stewart, W. E. Molecular Parameters for Normal Fluids - Lennard-Jones 12-6 Potential. *Ind. Eng. Chem. Fundam.* **1966**, *5*, 356-363.
30. Shimanouchi, T. Tables of Molecular Vibrational Frequencies Consolidated Volume 2. *J. Phys. Chem. Ref. Data* **1977**, *6*, 993-1102.
31. Chao, J.; Wilhoit, R. C.; Zwolinski, B. J. Ideal Gas Thermodynamic Properties of Ethane and Propane. *J. Phys. Chem. Ref. Data* **1973**, *2*, 427-437.

Chapter 7

Krypton Adsorption on Zeolite-Templated Carbon and Anomalous Surface Thermodynamics

M. Murialdo, N.P. Stadie, C.C. Ahn, and B. Fultz, “Krypton Adsorption on Zeolite-Templated Carbon and Anomalous Surface Thermodynamics,” *Langmuir*, 31, 7991 (2015).

DOI: 10.1021/acs.langmuir.5b01497

<http://pubs.acs.org/doi/abs/10.1021/acs.langmuir.5b01497>

Abstract

Krypton adsorption was measured at 8 temperatures between 253 and 433 K on a zeolite-templated carbon and two commercial carbons. The data were fitted using a generalized Langmuir isotherm model and thermodynamic properties were extracted. Differing from that on commercial carbons, krypton adsorption on the zeolite-templated carbon is accompanied by an increasing isosteric heat of adsorption, rising by up to 1.4 kJ mol^{-1} as a function of coverage. This increase is a result of enhanced adsorbate-adsorbate interactions promoted by the ordered, nanostructured surface of the adsorbent. An assessment of the strength and nature of these adsorbate-adsorbate interactions is made by comparing the measured isosteric heats of adsorption (and other thermodynamic quantities) to fundamental metrics of intermolecular interactions of krypton and other common gases.

1. Introduction

High surface area carbon materials have garnered interest for a variety of adsorptive applications^{1,2,3,4} ranging from hydrogen storage^{5,6} to carbon capture^{7,8} and many others. The recently emerged class of templated carbon materials^{9,10,11} exhibiting controlled pore-size distributions that depend on the template, have shown exceptional performance in many adsorptive applications owing to their uniquely ordered structure. Zeolite-templated carbon (ZTC) is one of the highest surface area carbonaceous materials known¹², and therefore exhibits a high specific adsorptive capacity toward small molecular species including hydrogen^{13,14} nitrogen¹⁵, carbon dioxide¹⁶, methane¹⁷, and water¹⁸. Further, our recent work has shown that ZTC exhibits not only a high specific adsorptive capacity, but also hosts an adsorbed phase with highly unusual properties; both ethane¹⁹ and methane²⁰ exhibit isosteric heats of adsorption on ZTC that *increase* with increasing surface coverage, a particularly rare and advantageous property for deliverable storage capacity. Due to its chemical homogeneity²⁰ and narrow pore-size distribution centered at a width of 12 Å, the surface of ZTC is optimized for promoting lateral interactions between adsorbed molecules, even when these interactions are exceedingly weak (e.g., as for methane).

Krypton, the fourth noble gas, is an unreactive monatomic gas that otherwise bears many similarities to methane. The two gases share a similar size (Kr: 3.9 Å, CH₄: 4.0 Å)²¹ and approximately spherical symmetry, as well as similar boiling points (120 K and 112 K, respectively)²² and critical temperatures (209 K and 190 K, respectively)²². Conveniently, monatomic krypton allows for very simple calculations of thermodynamic properties such as entropy, since rotational and internal vibrational modes do not exist. Krypton has applications in the photography, lighting²³, and medical industries,^{24,25} and is commonly used as an

adsorbate for characterizing low-surface-area materials^{26,27}. There is also active interest in finding adsorbent materials that can effectively separate krypton from xenon, especially the radioactive isotope ^{85}Kr .^{28,29} These gases are off-gassed from spent nuclear fuel and their separation is crucial to the development of “closed” nuclear fuel cycles³⁰. Nevertheless, krypton adsorption across a wide range of temperatures and pressures is a relatively unexplored topic, and the results can have relevant implications for many other more complex adsorptive systems.

2. Experimental

2.1 Materials Synthesis

Three microporous carbons were chosen for this study: MSC-30, CNS-201 and ZTC. MSC-30 was obtained from Kansai Coke & Chemicals Company Ltd. (Japan) and CNS-201 was obtained from A. C. Carbone Inc. (Canada). ZTC is a zeolite-templated carbon that was synthesized in a multistep process³¹ based on a previously reported approach designed to achieve high template fidelity of the product¹³. The template used was a NaY zeolite (faujasite) obtained from Tosoh Corp. (Japan). Briefly, the zeolite was first impregnated with furfuryl alcohol, which was polymerized at 423 K, before undergoing a 973 K propylene chemical vapor deposition step, and finally carbonization at 1173 K. The zeolite template was removed by dissolution in 48% hydrofluoric acid. The synthesis is described in detail elsewhere³¹.

2.2 Materials Characterization

Nitrogen adsorption isotherms were measured at 77 K using a BELSORP-max instrument (BEL-Japan Inc.). From these measurements, micropore volumes (Dubinin-

Radushkevich (DR) method^{32,33}) and specific surface areas (Brunauer-Emmett-Teller (BET) method³⁴) were determined. Pore-size distributions were obtained using non-local density functional theory (NLDFIT) analysis^{35,36} with a carbon slit-pore model and software from Micromeritics Instrument Corp. The skeletal density of each material was determined by helium pycnometry.

2.3 Measurements

Equilibrium adsorption isotherms of krypton on the three carbon adsorbents were measured at 8 temperatures between 253 and 433 K. Research-grade krypton (99.998%) was obtained from Air Liquide America Corp. and used in a custom Sieverts apparatus designed and tested for accuracy up to 10 MPa.³⁷ Measurements were made up to high pressures using an MKS Baratron (Model 833) pressure transducer. Each of the samples was degassed at 520 K under a vacuum of less than 10^{-9} MPa prior to testing. The Sieverts was equipped with a molecular drag pump capable of achieving a vacuum of 10^{-10} MPa and vacuum pressures were verified using a digital cold cathode pressure sensor (I-MAG, Series 423). The adsorbent was loaded into a stainless steel reactor, sealed with a copper gasket, and held at a constant temperature. To obtain low temperature isotherms, the reactor was submerged in a circulated chiller bath with temperature fluctuations no larger than ± 0.1 K. High temperature isotherms were obtained by encasing the reactor in a copper heat exchanger wrapped with insulating fiberglass heating tape. Using a PID controller, the reactor temperature was maintained with fluctuations no larger than ± 0.4 K. The temperature of the reactor was monitored with K-type thermocouples while the temperature of the gas manifold was measured with platinum resistance thermometers. For calculations of excess uptake, bulk phase gas densities were obtained from the REFPROP Standard Reference Database²². Multiple adsorption/desorption

isotherms were taken to ensure complete reversibility and identical measurements were found to be reproducible to within 1% error.

3. Results

3.1 Adsorbent Characterization

The BET surface areas of ZTC, MSC-30, and CNS-201 were determined to be 3591 ± 60 , 3244 ± 28 , and 1095 ± 8 m² g⁻¹, respectively. ZTC and MSC-30 also have similar micropore volumes of 1.66 and 1.54 cm³ g⁻¹ while CNS-201 has a much smaller micropore volume of 0.45 cm³ g⁻¹. Despite their similarities, ZTC and MSC-30 have very different pore-size distributions (Figure 1). Due to its templated nature, ZTC exhibits a single, sharp peak in its pore-size distribution, corresponding to a pore width of 12 Å. This has been determined by NLDFT pore-size analysis and further evidence is given by X-ray diffraction and transmission electron microscopy (TEM) investigations²⁰. Based on NLDFT pore-size analysis, over 90% of the micropore volume of ZTC is contained in pores with widths between 8.5 and 20 Å. MSC-30 on the other hand has a broad pore-size distribution with micropore widths ranging from 6 to 35 Å and over 40% of its micropore volume is in pores of widths greater than 21 Å. CNS-201, has three prominent pore widths at approximately 5.4, 8.0, and 11.8 Å, which contain roughly 50%, 20%, and 15% of the micropore volume respectively. The skeletal density of both activated carbons (MSC-30 and CNS-201) was found to be 2.1 g cm⁻³, which is close to the ideal density of graphite (~2.2 g cm⁻³). The templated carbon ZTC, however, was found to have a skeletal density of 1.8 g cm⁻³, which is in agreement with other zeolite-templated carbons.^{20,31}

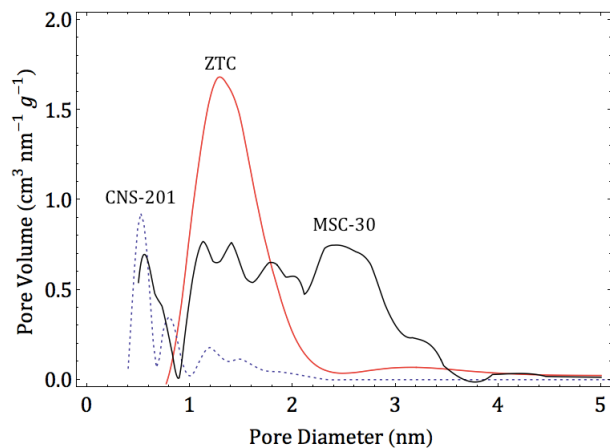


Figure 1. Pore-size distributions of the three carbon materials (CNS-201, MSC-30, and ZTC) derived from NLDFT analysis of nitrogen adsorption measurements at 77 K.

3.2 Adsorption Measurements

Equilibrium excess adsorption isotherms of krypton on ZTC, MSC-30 and CNS-201 are presented in Figure 2. At high pressures and low temperatures, excess adsorption reaches a maximum, a well-known phenomenon for Gibbs excess adsorption³⁸. At 253 K, ZTC, MSC-30, and CNS-201 have excess adsorption maxima of 22.6, 23.3, and 7.9 mmol g⁻¹, respectively. At 298 K, the excess adsorption maxima are 16.3, 17.7, and 6.6 mmol g⁻¹, respectively. MSC-30 exhibits a greater excess adsorption maximum than ZTC at all temperatures measured. This is in contrast to methane adsorption on the same materials where excess adsorption quantities on ZTC exceeded those on MSC-30 at low temperatures (238-265 K). CNS-201 exhibits the smallest excess adsorption uptake of the three materials due to its lower surface area.

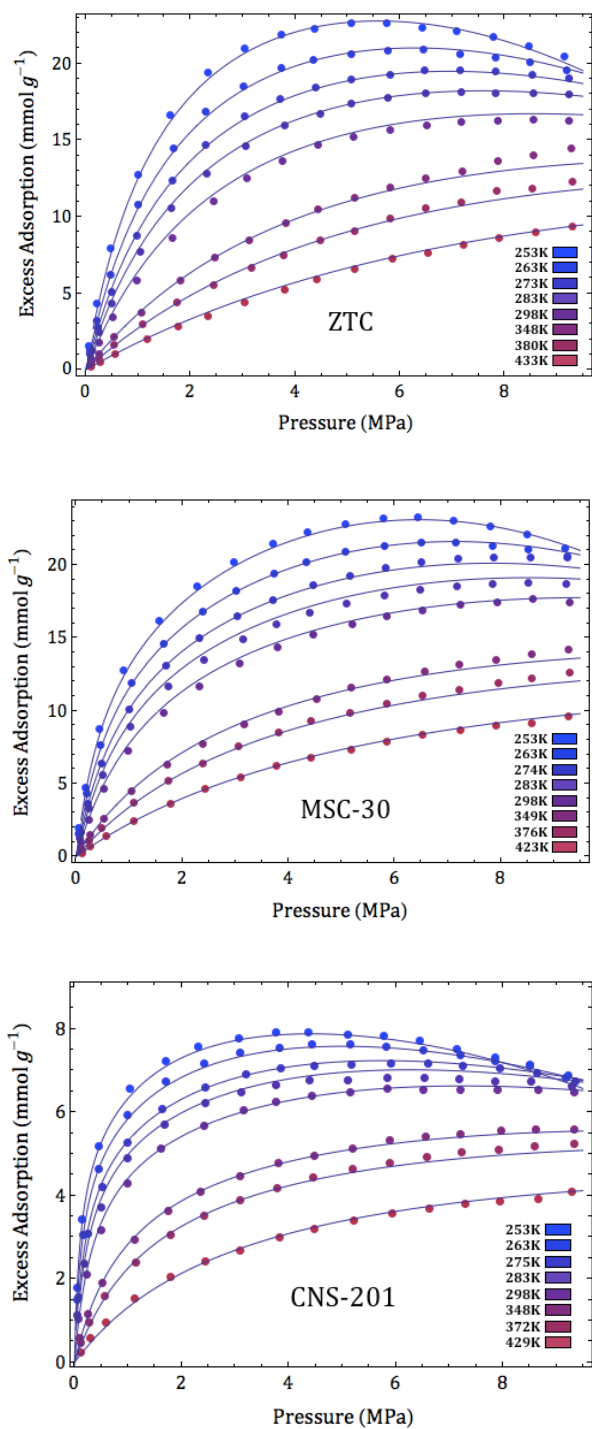


Figure 2. Equilibrium excess adsorption isotherms of krypton on ZTC, MSC-30, and CNS-201. The lines indicate the best fit as determined using a generalized (two-site) Langmuir isotherm model.

4. Data Analysis

4.1 Fitting Methodology

Thermodynamic analysis requires fitting the adsorption data points to a continuous function. While it is common to assume that excess adsorption is equivalent to absolute adsorption at low pressures, this assumption becomes invalid at high pressures and low temperatures. Our method for both fitting and determining the absolute quantity of adsorption from experimental data is based on a generalized-Langmuir model. Briefly, a previously described method³⁹ has been further modified to account for phenomena that are relevant to the nonideal gas regime; the complete details of this methodology are described elsewhere.⁴⁰

Gibbs excess adsorption (n_e) is a function of both the absolute adsorption (n_a) and the gas density in the bulk phase (ρ):

$$n_e = n_a - V_a \rho \quad (1)$$

If the volume of the adsorption layer (V_a) is known, determining absolute adsorption is trivial (given excess adsorption). However, as there is no generally accurate method for determining V_a we have left it as an independent fitting parameter. Excess adsorption quantities were fitted with the following generalized (multisite) Langmuir isotherm:

$$n_e(P, T) = (n_{max} - V_{max} \rho(P, T)) \left[\sum_i \alpha_i \frac{K_i P}{1 + K_i P} \right] \quad (2)$$

Here the independent fitting parameters are n_{max} , the maximum absolute adsorption which serves as a scaling factor, V_{max} which scales with coverage up to the maximum volume of the adsorption layer (V_{max}), α_i which weights the i^{th} Langmuir isotherm ($\sum_i \alpha_i = 1$), and K_i the

equilibrium constant of the i^{th} Langmuir isotherm. K_i is given by an Arrhenius-type equation

where A_i is a prefactor and E_i is the binding energy of the i th Langmuir isotherm:

$$K_i = \frac{A_i}{\sqrt{T}} e^{-E_i/RT} \quad (3)$$

Pressure and temperature are denoted by P and T respectively. By setting the number of Langmuir isotherms equal to two ($i=2$) we limit the number of independent fitting parameters to seven while still obtaining highly accurate fits. The residual mean square values of the fits on ZTC, MSC-30, and CNS-201 are 0.067, 0.070, and 0.0078 (mmol g^{-1})² respectively. Individual fitting parameters for adsorption on the three materials are given in Table 1.

Table 1. Least Squares Minimized Fitting Parameters of Krypton Excess Adsorption

| | n_{max} (mmol g ⁻¹) | V_{max} (cm ³ g ⁻¹) | α_1 | A_1 (K ^{1/2} MPa ⁻¹) | A_2 (K ^{1/2} MPa ⁻¹) | E_1 (kJ mol ⁻¹) | E_2 (kJ mol ⁻¹) |
|---------|--------------------------------------|---|------------|---|---|----------------------------------|----------------------------------|
| ZTC | 39 | 2.0 | 0.31 | 0.092 | 1.8E-6 | 10 | 30 |
| MSC-30 | 58 | 3.0 | 0.73 | 0.11 | 0.0031 | 12 | 13 |
| CNS-201 | 11 | 0.49 | 0.46 | 0.0059 | 0.069 | 15 | 16 |

The optimized fit parameters were found to be in reasonable agreement with independent estimates of physical quantities. For example, V_{max} corresponds to the maximum micropore filling volume. Dividing V_{max} by the BET surface area of the adsorbent gives an average maximum adsorption layer width. For ZTC, CNS-201, and MSC-30, the maximum adsorption layer widths determined from V_{max} are 5.6, 4.5, and 9.2 Å. These are in reasonable agreement with the average micropore half-widths for ZTC, CNS-201, and MSC-30 as determined by NLDFT analysis of the nitrogen adsorption uptake at 77K, which are 6, 4, and

7 Å, respectively. Additionally, estimates of the maximum possible absolute adsorption can be made by multiplying the measured micropore volume by the density of liquid krypton (28.9 mmol cm⁻³)²². For each material, n_{max} was within 30% of the estimated maximum possible absolute adsorption.

4.2 Determination of Isothermic Enthalpy of Adsorption

The isothermic enthalpy of adsorption (ΔH_{ads}) is a commonly used metric for assessing the strength of adsorbent-adsorbate interactions at constant coverage conditions. Here it is evaluated via the isothermic method and reported as a positive value, q_{st} the isothermic heat defined by the Clapeyron equation:

$$q_{st} = -\Delta H_{ads} = -T \left(\frac{\partial P}{\partial T} \right)_{n_a} (\Delta v_{ads}) \quad (4)$$

The molar change in volume of the adsorbate upon adsorption (Δv_{ads}) is determined by taking the difference between the gas-phase molar volume and the average adsorbed-phase molar volume (the average is approximated as $\frac{V_{max}}{n_{max}}$). The isothermic heats of krypton adsorption on

ZTC, MSC-30, and CNS-201 calculated in this way are shown in Figure 3.

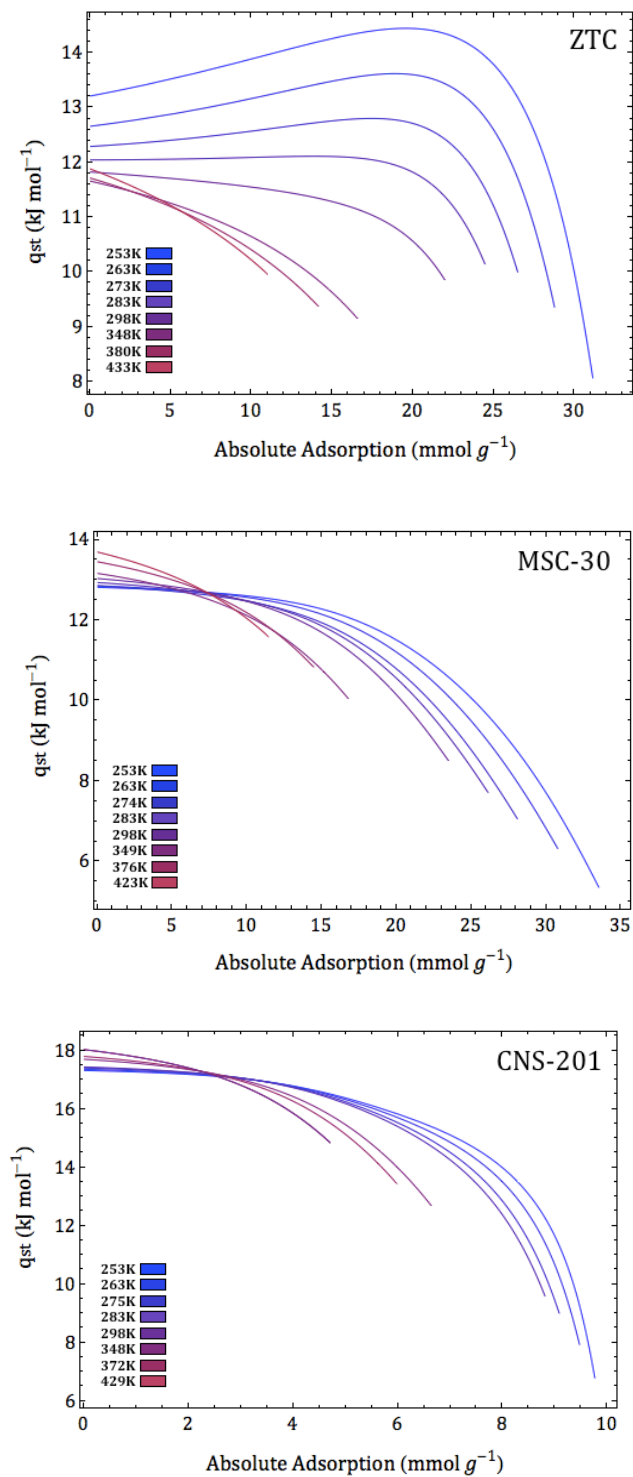


Figure 3. Isosteric heats of krypton adsorption on ZTC, MSC-30, and CNS-201.

5. Discussion

5.1 Isotheric Heat of Adsorption

The isotheric heats of krypton adsorption on MSC-30 and CNS-201 decrease as a function of absolute adsorption, or equivalently surface coverage, as shown in Figure 3. This is the typical behavior of gas adsorption on a heterogeneous surface, where binding sites are filled according to energetic favorability. CNS-201 has significantly higher isotheric heat of adsorption Henry's Law (zero coverage) values due to its small average pore width (8 Å). Krypton adsorption on ZTC, however, is accompanied by an initially increasing isotheric heat with coverage. At 253 K the isotheric heat rises to 14.6 kJ mol^{-1} , 1.4 kJ mol^{-1} above its Henry's Law value of 13.2 kJ mol^{-1} (an 11% increase). This effect has also been observed in both ethane and methane adsorption investigations on ZTC.^{19,20} The increasing isotheric heat is a result of adsorbate-adsorbate interactions promoted by the nanostructured surface of ZTC, an effect that becomes larger at low temperatures. As temperature is increased, the effect is severely diminished. At temperatures above 300 K no increase in the isotheric heat is observed. This suggests that the adsorbate-adsorbate interactions responsible for the increasing isotheric heat of adsorption have cooperative behavior that can be thermally disrupted.

5.2 Slope of Increasing Isotheric Heat of Adsorption

The slope of the increasing isotheric heat as a function of fractional coverage roughly scales with the strength of the intermolecular interactions, as determined by fundamental metrics such as the critical temperature (CT), boiling point (BP), and the Lennard-Jones well depth (ϵ). For krypton, methane, and ethane on ZTC, the average slopes of the isotheric heat

up to 50% surface coverage are reported alongside the CT, BP, and ϵ parameters for each gas (see Table 2).

Table 2. Slopes of Isothermic Heats of Adsorption as a Function of Fractional Coverage on ZTC at the Lowest Measured Temperature and Gas Properties of Krypton, Methane, and Ethane.

| | Slope (kJ mol ⁻¹) | CT (K) | BP (K) | ϵ (kJ mol ⁻¹) |
|---------|-------------------------------|-------------------|-------------------|------------------------------------|
| Krypton | 2.7 | 209 ²² | 120 ²² | 1.3 ²¹ |
| Methane | 2.2 | 190 ²² | 112 ²² | 1.2 ²¹ |
| Ethane | 3.3 | 305 ²² | 185 ²² | 1.7 ⁴¹ |

The ratios of the krypton/methane and krypton/ethane slopes are 1.2 and 0.82 respectively. These ratios are similar to the krypton/methane and krypton/ethane ratios of CT, BP, and ϵ . Furthermore, the slopes of the isothermic heat are in good agreement with a simplistic model that we have previously proposed¹⁹:

$$\frac{\partial(\xi)}{\partial\theta} = \frac{z\epsilon}{2} \quad (5)$$

The left hand side of Equation 5 ($\frac{\delta(\xi)}{\delta\theta}$) is the slope of the isothermic heat as a function of fractional coverage while z represents the number of nearest neighbors (posited to be 4) and ϵ is the Lennard-Jones potential well depth of the gas. Using Equation 5 the slopes of the krypton, methane and ethane isothermic heats on ZTC are estimated to be 2.6, 2.4, and 3.4 kJ mol⁻¹ (all within 10 percent of the average measured slope for each gas).

5.3 Isothermic Heat of Adsorption Maxima

At high coverage the isothermic heat of krypton adsorption on ZTC reaches a maximum and decreases with further coverage. In this regime the adsorbed-phase interatomic interactions are dominated by short-range repulsion due to the high density of adsorbates. The

optimal density for promoting adsorbate-adsorbate interactions is the adsorbate density at the maximum of the isosteric heat (for a given temperature). Here we label this optimal adsorbate density “ $\rho\Delta H_{max}$ ” and make comparisons to the bulk gas phase via the compressibility factor (Z). The compressibility factor provides a good metric of the nonideality of a gas under specific conditions.

$$Z = \frac{PV}{nRT} \quad (6)$$

While an ideal gas has a compressibility factor of 1, attractive intermolecular interactions decrease Z and repulsive interactions increase Z . For a van der Waals gas, the compressibility factor can be recast in terms of the coefficients of the van der Waals equation of state (a and b):

$$Z = \frac{V}{V-nb} - \frac{an}{RTV} \quad (7)$$

In this representation the minimum of the compressibility factor (where attractive interactions are most dominant) occurs at:

$$n = \frac{V - \left(\frac{V^2 b R T}{a}\right)^{\frac{1}{2}}}{b} \quad (8)$$

As temperature is increased at a fixed volume (V), the minimum point of the compressibility factor shifts to a lower number of particles (n) and hence to a lower density. The actual compressibility factor of krypton²² shows similar behavior (see Figure 4).

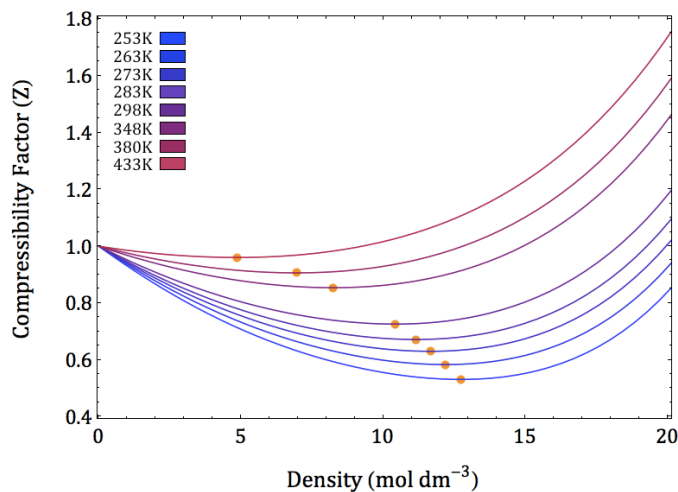


Figure 4. Compressibility factor of krypton between 253-433 K, as calculated by REFPROP²². The minima are indicated by orange circles.

The importance of the minimum in the compressibility factor is that it represents a critical point after which repulsive interactions begin to dominate over attractive interactions in the gas. The density at the compressibility factor minimum (ρZ_{min}), shown in Figure 4, can therefore be expected to correlate with the density of the adsorbed phase at the maximum in isosteric heat of adsorption ($\rho \Delta H_{max}$). Low temperature values (253-273 K) of $\rho \Delta H_{max}$ (for krypton on ZTC) were determined by dividing the absolute adsorption quantity at the isosteric heat maximum by the ZTC micropore volume ($1.66 \text{ cm}^3 \text{ g}^{-1}$). There is reasonable agreement between ρZ_{min} and $\rho \Delta H_{max}$ at low temperatures (less than 12% discrepancy) (see Figure 5).

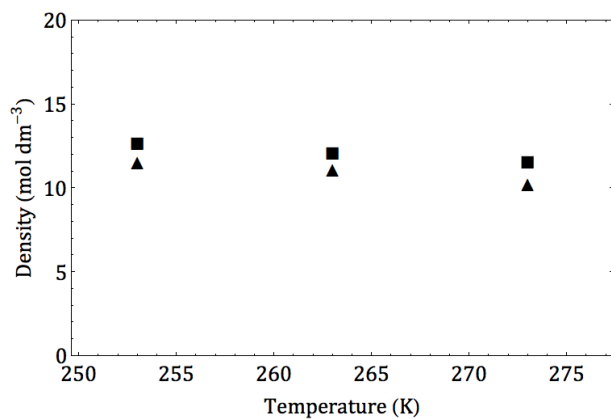


Figure 5. Comparison of ρZ_{min} (squares) and $\rho \Delta H_{max}$ (triangles).

5.4 Adsorbed-Phase Enthalpy

The adsorbed-phase enthalpy (H_a) of krypton on ZTC, MSC-30, and CNS-201 was determined as a function of coverage by adding the isosteric enthalpy of adsorption to the gas-phase enthalpy (H_g) (determined by REFPROP²²) (see Figure 6).

$$H_a = H_g + \Delta H_{ads} \quad (9)$$

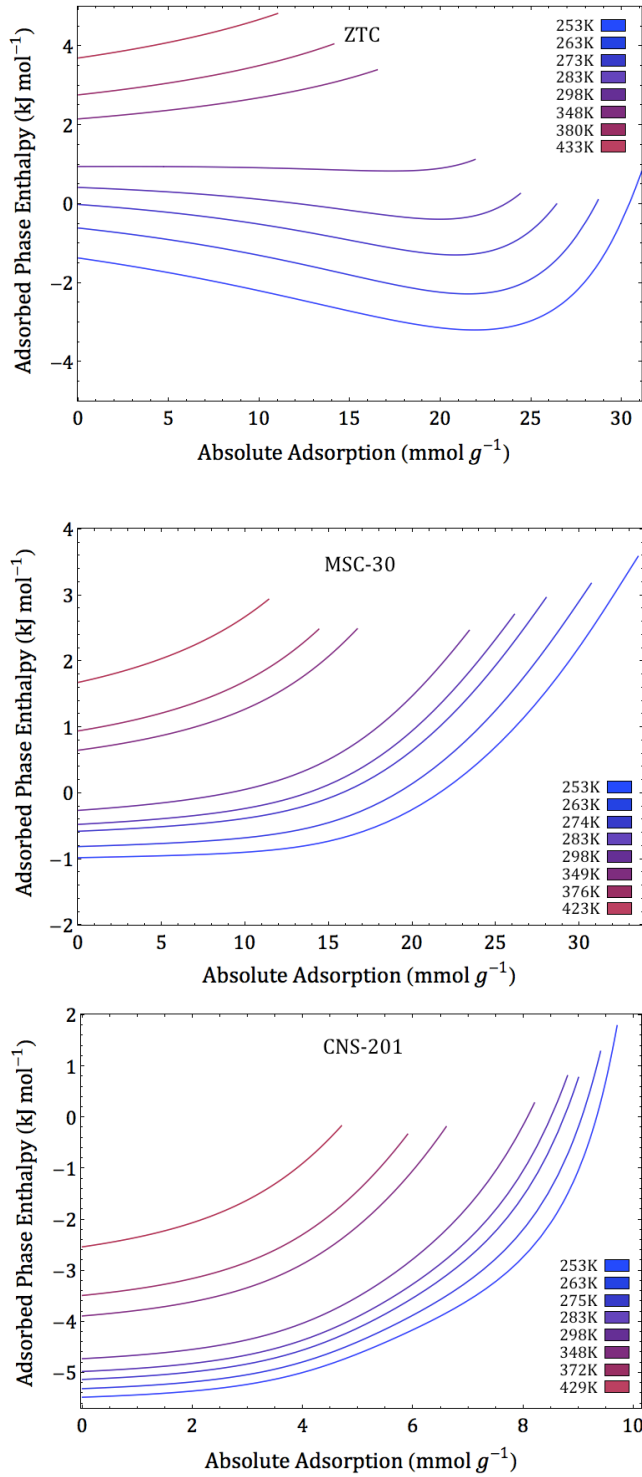


Figure 6. Adsorbed-phase enthalpy of krypton on ZTC, MSC-30, and CNS-201.

Due to favorable adsorbate-adsorbate interactions, the adsorbed-phase enthalpy of krypton on ZTC decreases towards a minimum (most favorable) enthalpy with coverage. Conversely, the adsorbed-phase enthalpy of krypton on MSC-30 and CNS-201 increases with coverage. The adsorbed-phase enthalpy may also be determined as a function of average interatomic distance. For example, the average interatomic distance of adsorbed krypton (x_{avg}) at a given state of surface coverage can be determined by dividing the micropore volume, V_{mic} , (1.66 cm³ g⁻¹ for ZTC) by the quantity of absolute adsorption (n_a), and taking the cube root:

$$x_{avg} = \left(\frac{V_{mic}}{n_a} \right)^{\frac{1}{3}} \quad (10)$$

The adsorbed-phase enthalpy at 253 K on ZTC as a function of average interatomic distance is comparable to the 12-6 Lennard-Jones potential between two krypton atoms²¹ (see Figure 7).

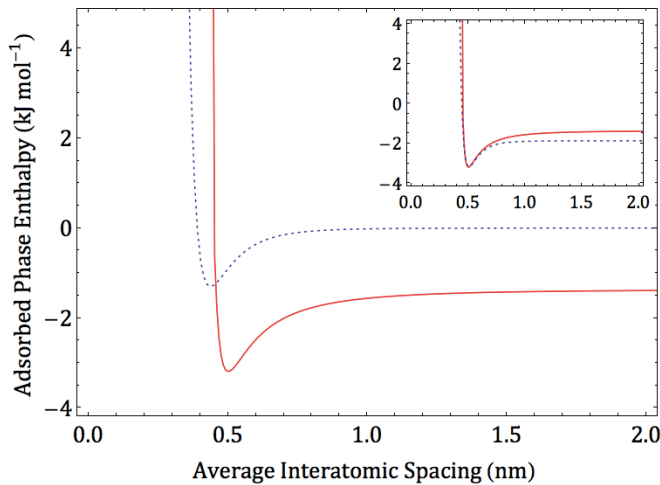


Figure 7. Comparison of the adsorbed-phase enthalpy of krypton on ZTC at 253 K (red) and the 12-6 Lennard-Jones potential of krypton (dashed blue). The inset shows both curves translated and superimposed for easier comparison.

At the lowest measured temperature in this work (253 K), the magnitude and form of the adsorbed-phase enthalpy of krypton on ZTC is remarkably similar to the 12-6 Lennard-Jones potential. Conversely, the adsorbed-phase enthalpies of krypton on MSC-30 and CNS-201 display no such behavior and are monotonically increasing functions. This provides further evidence that the anomalous isosteric heat of adsorption of krypton on ZTC results from enhanced interatomic interactions which can be rather accurately accounted for by the classic 12-6 interaction potential. The apparent offset in energy seen in Figure 7 is a result of the adsorbent-adsorbate interactions and the arbitrary nature of the enthalpy reference state (in this case the reference state is saturated liquid krypton at its normal boiling point, 120 K). The offset in interatomic distance (~ 0.07 nm) between the adsorbed-phase enthalpy and the 12-6 Lennard-Jones potential may result from clustering of the krypton atoms. While some of the krypton atoms may temporarily cluster into more optimally spaced groupings which reproduce the 12-6 Lennard-Jones potential shape and distance, the presence of non-clustered krypton atoms with larger interatomic distances could shift the *average* interatomic spacing to higher values resulting in the offset in interatomic distance.

The Henry's Law values of the adsorbed-phase enthalpies are also indicative of the atypical properties of ZTC as an adsorbent for krypton. The enthalpy of a two-dimensional ideal gas is $2RT$ and therefore depends linearly on temperature with a slope of $2R$ ($16.6 \text{ J mol}^{-1} \text{ K}^{-1}$). Correspondingly, the Henry's Law values of the adsorbed-phase enthalpy of krypton on MSC-30 and CNS-201 also depend linearly on temperature, with slopes of 15.6 and $16.7 \text{ J mol}^{-1} \text{ K}^{-1}$, respectively (see Figure 8).

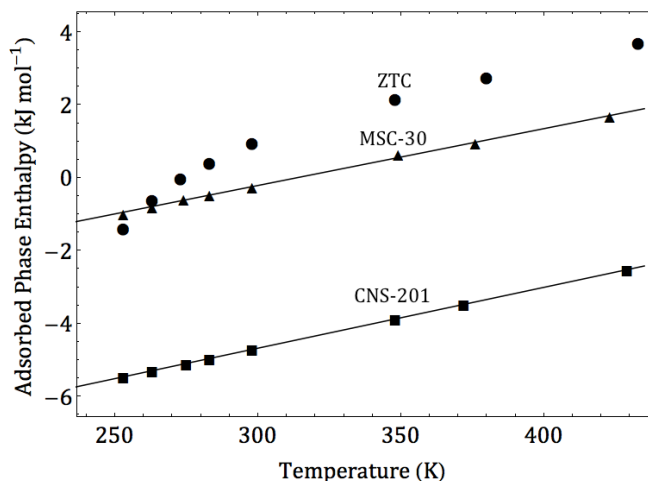


Figure 8. Henry's law enthalpies of adsorbed krypton on ZTC (circles), MSC-30 (triangles) and CNS-201 (squares) as a function of temperature. Lines are to guide the eye.

The Henry's Law values of the adsorbed-phase enthalpy of krypton on ZTC, however, do not vary linearly with temperature until beyond 350 K. At high temperatures (>350 K) the slope converges to approximately $2R$. At low temperatures, however, deviations between the measured Henry's Law values and those predicted using the ideal gas slope of $2R$, are observed. These deviations likely result from the unique structure of ZTC and may in part be due to a loss of favorable interactions with increasing temperature.

5.5 Entropy

The isosteric entropy of adsorption (ΔS_{ads}) is the change in entropy upon adsorption: the difference between the entropy of the adsorbed phase and the entropy of the gas phase at isosteric conditions. At equilibrium, the isosteric entropy of adsorption and the isosteric enthalpy of adsorption (ΔH_{ads}) are related by:

$$\Delta S_{ads} = \frac{\Delta H_{ads}}{T} \quad (13)^{19}$$

As for the enthalpy, the entropy of the adsorbed phase can be determined by adding the isosteric entropy of adsorption to the entropy of krypton gas (calculated using REFPROP²²). The molar entropy of adsorbed-phase krypton as a function of coverage on the three materials in this study is shown in Figure 9. The reference state in this case is solid krypton at absolute zero.

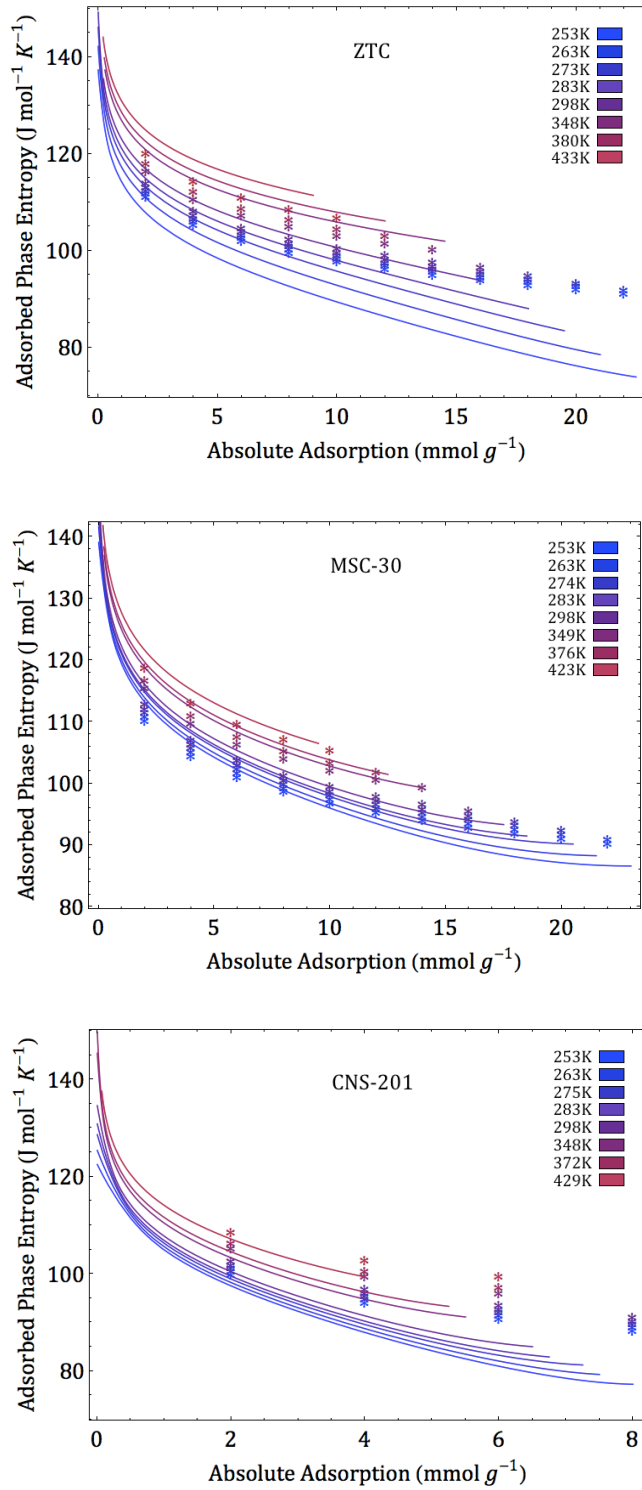


Figure 9. The entropy of adsorbed-phase krypton on ZTC, MSC-30 and CNS-201 derived by experiment (lines) and calculated using statistical mechanics (asterisks).

For comparison to the experimental data, the adsorbed-phase entropy of krypton was also calculated using statistical mechanics (shown in Figure 9). A basic statistical mechanics model based on a two-dimensional lattice gas was used, as described elsewhere¹⁹. Since krypton is a monatomic gas with spherical symmetry and no internal vibrational modes, only partition functions for the surface vibrational modes and configurational modes were considered. The entropies corresponding to these individual contributions were determined and summed to obtain the total entropy of the adsorbed phase (see Figure 9).

For krypton adsorbed on MSC-30 and CNS-201, agreement between the measured and calculated adsorbed-phase entropies is good, with discrepancies of 5% and 15% respectively. The small pores and high isosteric heat of adsorption of krypton on CNS-201 result in less accurate statistical mechanics approximations of surface vibrational modes and hence somewhat larger deviations than for MSC-30. Moreover, the general temperature dependence is preserved in both cases, especially at low quantities of uptake. For krypton on ZTC, however, discrepancies are in excess of 23% despite moderate pore sizes; the experimental adsorbed-phase entropy is much lower than estimated values due to enhanced interatomic interactions. It is reasonable to attribute a large fraction of this discrepancy to clustering effects (reduced configurations of the adsorbed phase due to interatomic interactions)⁴⁰, and further investigation of such phenomena is warranted.

6. Conclusions

Equilibrium excess adsorption uptake of krypton was measured on three microporous carbon materials: ZTC, MSC-30 and CNS-201. By fitting the data using a robust generalized Langmuir isotherm model, absolute adsorption quantities were determined along with

physically realistic fitting parameters and thermodynamic quantities of adsorption. While the isosteric heat of adsorption decreases with coverage on MSC-30 and CNS-201 (the typical case), it increases by over 10% on ZTC, reaching its maximum at a surface coverage of 19.6 mmol g⁻¹ at 253 K. This previously unreported effect for supercritical krypton adsorption on a high surface area carbon results from the enhancement of favorable krypton-krypton interactions on the ZTC surface due to its uniquely ordered porous nanostructure. Moreover, the magnitude of the increase is dependent on the strength of the interatomic interactions of krypton, a result that is corroborated by comparisons to ethane and methane. Additional analysis of the isosteric heat of adsorption maxima, adsorbed-phase enthalpy, and adsorbed-phase entropy provide further evidence and insight into the nature of the interactions responsible for the anomalous surface thermodynamics reported in this paper.

Acknowledgement:

This work was sponsored as a part of EFree (Energy Frontier Research in Extreme Environments), an Energy Frontier Research Center funded by the US Department of Energy, Office of Science, Basic Energy Sciences under Award Number DE-SC0001057.

References:

1. Dillon, A. C.; Heben, M. J. Hydrogen Storage Using Carbon Adsorbents: Past, Present and Future. *Appl. Phys. A: Mater. Sci. Process.* **2001**, *72*, 133-142.
2. Richard, M. A.; Cossement, D.; Chandonia, P. A.; Chahine, R.; Mori, D.; Hirose, K. Preliminary Evaluation of the Performance of an Adsorption-Based Hydrogen Storage System. *AIChE J.* **2009**, *55*, 2985-2996.
3. Alcaniz-Monge, J.; Lozano-Castello, D.; Cazorla-Amoros, D.; Linares-Solano, A. Fundamentals of Methane Adsorption in Microporous Carbons. *Microporous Mesoporous Mater.* **2009**, *124*, 110-116.
4. Dabrowski, A. Adsorption - from Theory to Practice. *Adv. Colloid Interface Sci.* **2001**, *93*, 135-224.
5. Panella, B.; Hirscher, M.; Roth, S. Hydrogen Adsorption in Different Carbon Nanostructures. *Carbon* **2005**, *43*, 2209-2214.
6. Poirier, E.; Chahine, R.; Bose, T. K. Hydrogen Adsorption in Carbon Nanostructures. *Int. J. Hydrogen Energy* **2001**, *26*, 831-835.
7. Plaza, M. G.; Pevida, C.; Arenillas, A.; Rubiera, F.; Pis, J. J. CO₂ Capture by Adsorption with Nitrogen Enriched Carbons. *Fuel* **2007**, *86*, 2204-2212.
8. Samanta, A.; Zhao, A.; Shimizu, G. K. H.; Sarkar, P.; Gupta, R. Post-Combustion CO₂ Capture Using Solid Sorbents: A Review. *Ind. Eng. Chem. Res.* **2012**, *51*, 1438-1463.
9. Kyotani, T.; Nagai, T.; Inoue, S.; Tomita, A. Formation of New Type of Porous Carbon by Carbonization in Zeolite Nanochannels. *Chem. Mater.* **1997**, *9*, 609-615.
10. Ryoo, R.; Joo, S. H.; Kruk, M.; Jaroniec, M. Ordered Mesoporous Carbons. *Adv. Mater.* **2001**, *13*, 677-681.
11. Nishihara, H.; Kyotani, T. Templated Nanocarbons for Energy Storage. *Adv. Mater.* **2012**, *24*, 4473-4498.
12. Yang, Z. X.; Xia, Y. D.; Mokaya, R. Enhanced Hydrogen Storage Capacity of High Surface Area Zeolite-Like Carbon Materials. *J. Am. Chem. Soc.* **2007**, *129*, 1673-1679.
13. Nishihara, H.; Hou, P.-X.; Li, L.-X.; Ito, M.; Uchiyama, M.; Kaburagi, T.; Ikura, A.; Katamura, J.; Kawarada, T.; Mizuuchi, K.; Kyotani, T. High-Pressure Hydrogen Storage in Zeolite-Templated Carbon. *J. Phys. Chem. C* **2009**, *113*, 3189-3196.
14. Yang, Z. X.; Xia, Y. D.; Sun, X. Z.; Mokaya, R. Preparation and Hydrogen Storage Properties of Zeolite-Templated Carbon Materials Nanocast via Chemical Vapor Deposition: Effect of the Zeolite Template and Nitrogen Doping. *J. Phys. Chem. B* **2006**, *110*, 18424-18431.
15. Su, F. B.; Zhao, X. S.; Lv, L.; Zhou, Z. C. Synthesis and Characterization of Microporous Carbons Templated by Ammonium-Form Zeolite Y. *Carbon* **2004**, *42*, 2821-2831.
16. Xia, Y. D.; Mokaya, R.; Walker, G. S.; Zhu, Y. Q. Superior CO₂ Adsorption Capacity on N-doped, High-Surface-Area, Microporous Carbons Templated from Zeolite. *Adv. Energy Mater.* **2011**, *1*, 678-683.
17. Guan, C.; Su, F. B.; Zhao, X. S.; Wang, K. Methane Storage in a Template-Synthesized Carbon. *Sep. Purif. Technol.* **2008**, *64*, 124-126.

18. Kyakuno, H.; Matsuda, K.; Nakai, Y.; Fukuoka, T.; Maniwa, Y.; Nishihara, H.; Kyotani, T. Amorphous Water in Three-Dimensional Confinement of Zeolite-Templated Carbon. *Chem. Phys. Lett.* **2013**, *571*, 54-60.
19. Murialdo, M.; Stadie, N. P.; Ahn, C. C.; Fultz, B. Observation and Investigation of Increasing Isothermic Heat of Adsorption of Ethane on Zeolite-Templated Carbon. *J. Phys. Chem. C* **2015**, *119*, 944-950.
20. Stadie, N. P.; Murialdo, M.; Ahn, C. C.; Fultz, B. Anomalous Isothermic Enthalpy of Adsorption of Methane on Zeolite-Templated Carbon. *J. Am. Chem. Soc.* **2013**, *135*, 990-993.
21. Cuadros, F.; Cachadina, I.; Ahumada, W. Determination of Lennard-Jones Interaction Parameters Using a New Procedure. *Mol. Eng.* **1996**, *6*, 319-325.
22. Lemmon, E. W.; Huber, M. L.; McLinden, M. O. *NIST Standard Reference Database 23: Reference Fluid Thermodynamic and Transport Properties-REFPROP*, version 8.0; National Institute of Standards and Technology: Gaithersburg, MD, 2007; CD-ROM.
23. Hwang, H. S.; Baik, H. K.; Park, K. W.; Song, K. M.; Lee, S. J. Excitation Energy Transfer of Metastable Krypton Atoms in Kr-He-Xe Low Pressure Glow Discharge for Mercury-Free Lighting. *Jpn. J. Appl. Phys.* **2010**, *49*, 3.
24. Chon, D.; Beck, K. C.; Simon, B. A.; Shikata, H.; Saba, O. I.; Hoffman, E. A. Effect of Low-Xenon and Krypton Supplementation on Signal/Noise of Regional CT-based Ventilation Measurements. *J. Appl. Physiol.* **2007**, *102*, 1535-1544.
25. Pavlovskaya, G. E.; Cleveland, Z. I.; Stupic, K. F.; Basaraba, R. J.; Meersmann, T. Hyperpolarized Krypton-83 as a Contrast Agent for Magnetic Resonance Imaging. *Proc. Natl. Acad. Sci. U.S.A.* **2005**, *102*, 18275-18279.
26. Takei, T.; Chikazawa, M. Measurement of Pore Size Distribution of Low-Surface-Area Materials by Krypton Gas Adsorption Method. *J. Ceram. Soc. Jpn.* **1998**, *106*, 353-357.
27. Youssef, A. M.; Bishay, A. F.; Hammad, F. H. Determination of Small Surface-Areas by Krypton Adsorption. *Surf. Technol.* **1979**, *9*, 365-370.
28. Ryan, P.; Farha, O. K.; Broadbelt, L. J.; Snurr, R. Q. Computational Screening of Metal-Organic Frameworks for Xenon/Krypton Separation. *AIChE J.* **2011**, *57*, 1759-1766.
29. Bae, Y.-S.; Hauser, B. G.; Colon, Y. J.; Hupp, J. T.; Farha, O. K.; Snurr, R. Q. High Xenon/Krypton Selectivity in a Metal-Organic Framework with Small Pores and Strong Adsorption Sites. *Microporous Mesoporous Mater.* **2013**, *169*, 176-179.
30. Izumi, J. Waste Gas Treatment Using Zeolites in Nuclear-related Industries. In *Handbook of Zeolite Science and Technology*; Auerbach, S. M., Carrado, K. A., Dutta, P. K., Eds.; Marcel Dekker: New York, 2003; Chapter 20.
31. Stadie, N. P.; Vajo, J. J.; Cumberland, R. W.; Wilson, A. A.; Ahn, C. C.; Fultz, B. Zeolite-Templated Carbon Materials for High-Pressure Hydrogen Storage. *Langmuir* **2012**, *28*, 10057-10063.
32. Dubinin, M. M.; Radushkevich, L. V. Equation of the Characteristic Curve of Activated Charcoal. *Proc. Acad. Sci. USSR, Phys. Chem. Sect.* **1947**, *55*, 331-337.
33. Nguyen, C.; Do, D. D. The Dubinin-Radushkevich Equation and the Underlying Microscopic Adsorption Description. *Carbon* **2001**, *39*, 1327-1336.

34. Brunauer, S.; Emmett, P. H.; Teller, E. Adsorption of Gases in Multimolecular Layers. *J. Am. Chem. Soc.* **1938**, *60*, 309-319.
35. Lastoskie, C.; Gubbins, K. E.; Quirke, N. Pore-Size Distribution Analysis of Microporous Carbons - A Density-Functional Theory Approach. *J. Phys. Chem.* **1993**, *97*, 4786-4796.
36. Lastoskie, C.; Gubbins, K. E.; Quirke, N. Pore-Size Heterogeneity and the Carbon Slit Pore - A Density-Functional Theory Model. *Langmuir* **1993**, *9*, 2693-2702.
37. Bowman, R. C.; Luo, C. H.; Ahn, C. C.; Witham, C. K.; Fultz, B. The Effect of Tin on the Degradation of LaNi_{5-y}Sny Metal-Hydrides During Thermal Cycling. *J. Alloys Compd.* **1995**, *217*, 185-192.
38. Sircar, S. Gibbsian Surface Excess for Gas Adsorption - Revisited. *Ind. Eng. Chem. Res.* **1999**, *38*, 3670-3682.
39. Mertens, F. O. Determination of Absolute Adsorption in Highly Ordered Porous Media. *Surf. Sci.* **2009**, *603*, 1979-1984.
40. Stadie, N. P.; Murialdo, M.; Ahn, C. C.; Fultz, B. Unusual Thermodynamics and Clustering of Adsorbed Methane on Zeolite-Templated Carbon. *J. Phys. Chem. C*, submitted for publication, **2015**.
41. Tee, L. S.; Gotoh, S.; Stewart, W. E. Molecular Parameters for Normal Fluids - Lennard-Jones 12-6 Potential. *Ind. Eng. Chem. Fundam.* **1966**, *5*, 356-363.

Chapter 8

A Generalized Law of Corresponding States for the Physisorption of Classical Gases with Cooperative Adsorbate-Adsorbate Interactions

M. Murialdo, N.P. Stadie, C.C. Ahn, and B. Fultz, “A Generalized Law of Corresponding States for the Physisorption of Classical Gases with Cooperative Adsorbate-Adsorbate Interactions,” *J. Phys. Chem. C*, 120, 11847 (2016).

DOI: 10.1021/acs.jpcc.6b00289

<http://pubs.acs.org/doi/abs/10.1021/acs.jpcc.6b00289>

Abstract

The Law of Corresponding States for classical gases is well established. Recent attempts at developing an analogous Law of Corresponding States for gas physisorption, however, have had limited success, in part due to the omission of relevant adsorption considerations such as the adsorbate volume and cooperative adsorbate-adsorbate interactions. In this work, we modify a prior Law of Corresponding States for gas physisorption to account for adsorbate volume, and test it with experimental data and a generalized theoretical approach. Furthermore, we account for the recently-reported cooperative adsorbate-adsorbate interactions on the surface of zeolite-templated carbon (ZTC) with an Ising-type model, and in doing so, show that the Law of Corresponding States for gas physisorption remains valid even in the presence of atypically enhanced adsorbate-adsorbate interactions.

1. Introduction

Gas physisorption on microporous carbons has been extensively explored for a variety of applications ranging from improved gas storage to efficient gas separation. At high pressures, nonideal effects can significantly influence both the gaseous and adsorbed phases. In bulk gases, the Law of Corresponding States generalizes the gas nonideality and provides a simplified equation of state. According to this law, nonideal gases behave similarly and have similar compressibility factors at corresponding conditions (i.e., when the conditions of the gases relative to the critical point are equal). The Law of Corresponding States has been shown to be highly accurate for bulk gases through a number of studies^{1,2}.

In 2002 Quinn hypothesized an extension to the Law of Corresponding States for gas physisorption, based on empirical evidence.³ Quinn posited that gases have approximately equal excess adsorption uptake quantities (n_e) at corresponding conditions on the same adsorbent, which we call “Quinn’s hypothesis of corresponding states.” Quinn provided evidence to support this hypothesis by comparing argon, carbon monoxide, methane, nitrogen, and oxygen physisorption on four microporous carbons. Quinn found general agreement among the corresponding excess adsorption uptake quantities, although discrepancies often exceeded 50%. Hydrogen physisorption did not follow the trend, a fact that was initially attributed to hydrogen being able to better penetrate the adsorbent micropores, but later explained more satisfactorily as a quantum effect.⁴ Recently, others have expanded Quinn’s hypothesis to include gate-opening MOFs and have noted deviations for larger molecules,⁵ but to date this issue has not been resolved. In this work we present a novel Law of Corresponding States for gas physisorption that includes adsorbate volume

considerations. It builds upon previous work but is more successful, especially for larger molecules such as ethane.

2. Quinn's Hypothesis of Corresponding States

Excess adsorption uptake of methane, krypton and ethane on three microporous carbons are compared at corresponding conditions in Figure 1 using values from Ref. ^{6,7,8} along with new measurements. These three carbons (ZTC, MSC-30 and CNS-201) have significant differences in synthesis, specific surface area, and pore-size distribution, but all contain predominantly micropores (see Supporting Information, S1). For each adsorbent, experimentally measured isotherms of the three gases are compared at reduced temperatures (T^R) of 1.25 ± 0.02 and 1.38 ± 0.03 and at corresponding reduced pressures (P^R), which are defined as

$$T^R = \frac{T}{T_c} \quad (1)$$

$$P^R = \frac{P}{P_c} \quad (2)$$

$$V^R = \frac{V}{V_c} \quad (3)$$

Here T , P and V are the system temperature, bulk phase pressure and bulk phase molar volume, and T_c , P_c and V_c are the critical temperature, pressure, and molar volume of the bulk fluid.

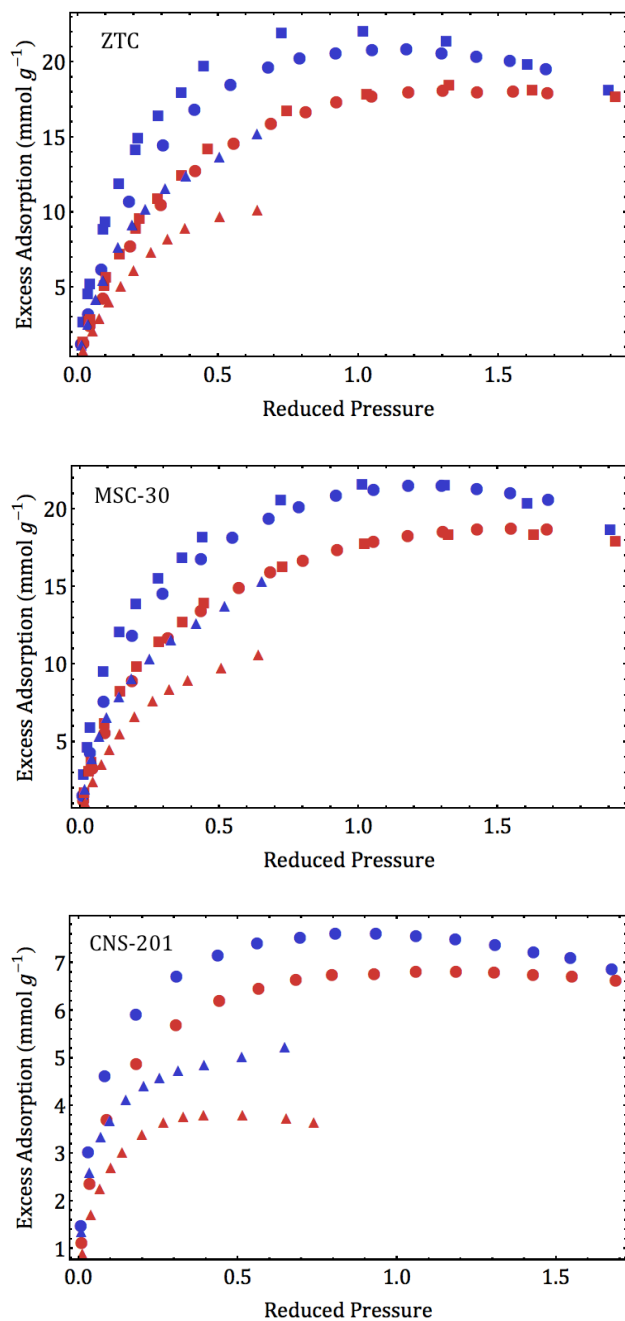


Figure 1. Comparison of methane (squares), krypton (circles), and ethane (triangles) excess adsorption at corresponding conditions as per Quinn's hypothesis (at reduced temperatures of 1.25 ± 0.02 (blue) and 1.38 ± 0.03 (red)).

As seen in Figure 1, there is good agreement between the measured methane and krypton isotherms using Quinn's hypothesis of corresponding states, with only moderate discrepancies (less than 25%). The ethane isotherms, however, deviate significantly from those of the other gases, with discrepancies of $\sim 50\%$.

It is notable that all of the adsorptive species used for empirical support of Quinn's hypothesis of corresponding states (argon, carbon monoxide, methane, nitrogen, and oxygen) have similar molecular size. This is seen by comparing their 12-6 Lennard-Jones parameters, σ , which serve as proxies for excluded-volume diameters (see Table 1). Argon, carbon monoxide, methane, nitrogen, oxygen, and krypton all have σ values that are within 5% of their group average, 0.3560 nm. Ethane, however, is a significantly larger molecule with a σ that is 26% larger than the group average. Accordingly, ethane does not adhere to Quinn's hypothesis of corresponding states.

Table 1. Lennard-Jones σ Parameters of Relevant Gases

| gas | Lennard-Jones σ (nm) |
|-----------------|--------------------------------|
| argon | 0.3405 ⁹ |
| carbon monoxide | 0.3661 ⁹ |
| methane | 0.3737 ⁹ |
| nitrogen | 0.3613 ⁹ |
| oxygen | 0.3382 ⁹ |
| krypton | 0.3636 ⁹ |
| ethane | 0.4480 ¹⁰ |

3. Law of Corresponding States Comparing Fractional Occupancy

In this work, we define fractional occupancy (θ) as the ratio of the absolute adsorbed amount (n_a) to the maximum possible quantity of adsorption for the adsorbent at any temperature or pressure (n_{max}):

$$\theta = \frac{n_a}{n_{max}} \quad (4)$$

By comparing fractional occupancies instead of excess adsorption, we develop a Law of Corresponding States for the physisorption of classical gases interacting through London dispersion forces that better fits empirical data:

“At corresponding conditions on the same adsorbent, classical adsorbed gases have the same fractional occupancy.”

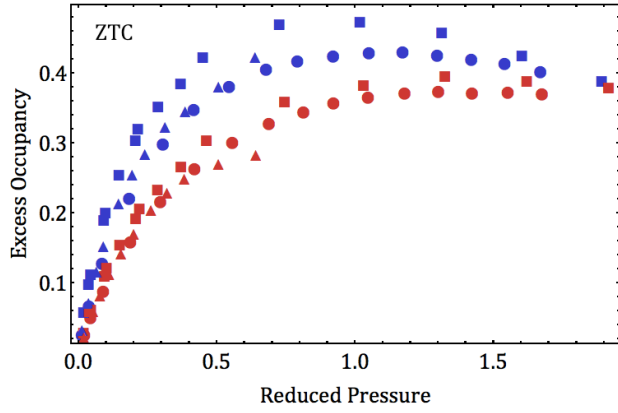
Unfortunately, absolute adsorption and hence fractional occupancy are not easily accessible through experimentation. Consequently we also define a proxy metric, the excess occupancy (θ_e):

$$\theta_e = \frac{n_e}{n_{max}} \quad (5)$$

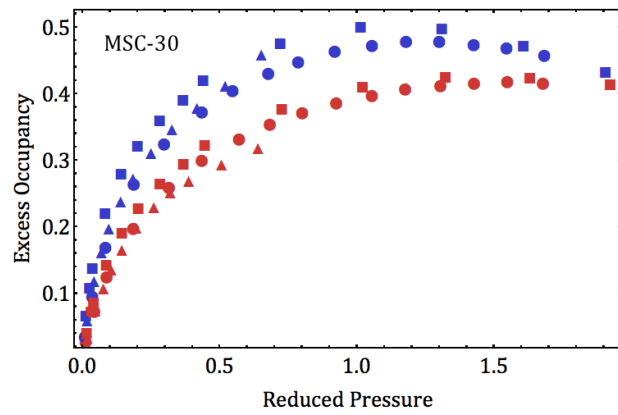
At low gas densities, the excess occupancy well approximates the fractional occupancy, but excess occupancies are more easily obtained by experiment. For this reason, here, we compare excess occupancies instead of the more fundamental fractional occupancies, which must be determined indirectly. For completeness, we also extrapolate fractional occupancies using a fitting procedure and compare these values at corresponding conditions in the Supporting Information (S3). The maximum adsorption quantity was estimated by multiplying the liquid

molar density of the adsorptive species at its triple point by the measured micropore volume of the adsorbent (see Supporting Information S2).

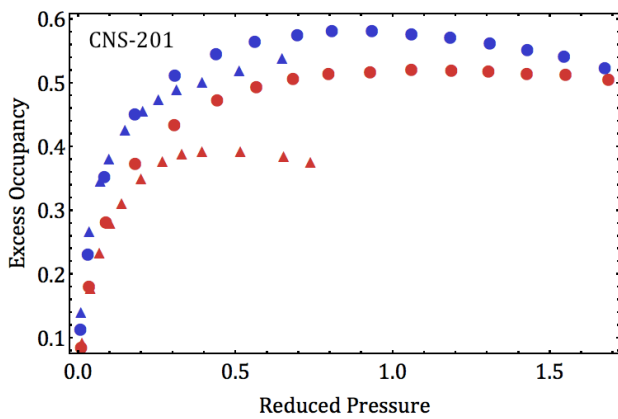
The experimentally-derived excess occupancies of methane, krypton and ethane on ZTC, MSC-30 and CNS-201 are compared at reduced temperatures of 1.25 ± 0.02 and 1.38 ± 0.03 (Figure 2, A-C). Using a robust fitting technique described in detail elsewhere¹¹, ethane excess occupancies have been extrapolated to higher reduced temperatures of 1.43 ± 0.01 , 1.80 ± 0.02 and 2.07 ± 0.05 and compared to experimentally measured methane and krypton data at corresponding conditions (Figure 2, D-E).



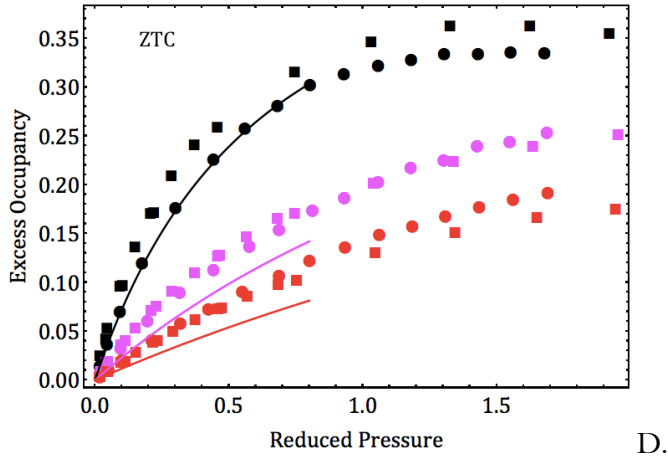
A.



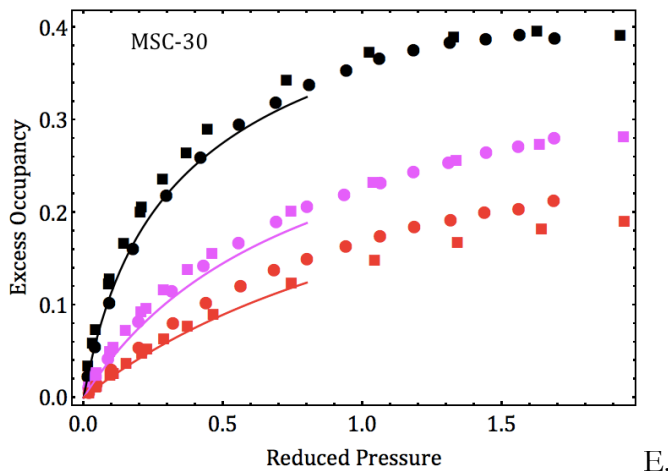
B.



C.



D.



E.

Figure 2. Comparison of excess occupancies at corresponding conditions for methane (squares), krypton (circles), and ethane (triangles) adsorption. The data in A-C are at reduced temperatures of 1.25 ± 0.02 (blue) and 1.38 ± 0.03 (red). The data in D-E are at reduced temperatures of 1.43 ± 0.01 (black), 1.80 ± 0.02 (magenta), and 2.07 ± 0.05 (red). The lines indicate extrapolated ethane results, calculated from the fit parameters obtained by fitting experimental data with a superposition of Langmuir isotherms.

Figure 2, which presents the experimentally-derived excess occupancies of methane, krypton, and ethane at corresponding conditions, shows good correspondence between the curves, with discrepancies of less than 25%, except for ethane at high temperatures on CNS-201. This may result from a rotational hindrance of the ethane molecules within the very small pores of CNS-201 (as small as ~ 0.54 nm in width). This comparison of excess occupancies instead of excess uptake gives a significant improvement over Quinn's hypothesis of corresponding states where discrepancies of $\sim 50\%$ can be found with the same experimental data. Likewise, the extrapolated excess occupancies of ethane on MSC-30 are in reasonable agreement (discrepancies of less than 25%) with the experimentally derived excess occupancies of methane and krypton at reduced temperatures of 1.43 ± 0.01 , 1.80 ± 0.02 , and 2.07 ± 0.05 . On ZTC, deviations between the experimental and the extrapolated isotherms are larger and likely derive from small fitting inaccuracies magnified over the huge extrapolation range (>220 K). The fitting and extrapolation procedure was not applied to ethane on CNS-201 due to an insufficient number of available isotherms.

4. Law of Corresponding States for Physisorption

There are two fundamentally distinct approaches to understanding gas-solid physisorption: the mono and multi-layer adsorption models developed by Langmuir, Brunauer, Emmett, Teller and others¹², and the pore-filling model developed by Eucken, Polanyi, Dubinin, and others¹². Each model successfully treats relevant physisorption phenomenon under differing conditions and both have widespread use. Here the Law of Corresponding States for physisorption is justified in the context of each model.

4.1 Monolayer Adsorption Model

Adsorbed molecules form a densified layer near the adsorbent surface, in a dynamic equilibrium with the gas phase. The significant decrease in the molar entropy of the adsorptive species upon adsorption is offset by a commensurate decrease in the molar enthalpy. At equilibrium

$$\frac{\Delta H_{ads}}{T} = \Delta S_{ads} \quad (6)$$

$$\Delta H_{ads} = H_a - H_g \quad (7)$$

$$\Delta S_{ads} = S_a - S_g \quad (8)$$

where ΔH_{ads} is the isosteric enthalpy of adsorption and ΔS_{ads} is the isosteric entropy of adsorption. It should be possible to predict the fractional occupancy of the adsorbed species at a fixed temperature and gas pressure with knowledge of the gas-phase enthalpy (H_g) and entropy (S_g), and knowledge of the constant-coverage, adsorbed-phase enthalpy (H_a) and entropy (S_a) (and how they change with fractional occupancy at a fixed temperature).

The gas-phase molar entropy, S_g (in reference to the boiling-point liquid molar entropy, S_{L1}), of monatomic gases with similar critical volumes is well approximated by a function that depends only on reduced quantities, $f(T^R, V^R)$ (Supporting Information, S4). We assume that the molar entropy of the adsorbed phase (S_a) is given by the molar entropy of the liquid phase (S_{L1}) with the addition of a θ -dependent entropy of configurations of the adsorbate molecules on the adsorbent, $f(\theta)$.¹³

$$S_a = S_{L1} + f(\theta) \quad (9)$$

The S_g (in reference to S_{Lj}) is approximated by $f(T^R, P^R)$,

$$-\Delta S_{ads} = f(T^R, P^R) - f(\theta) \quad (10)$$

For a monatomic gas, the right-hand side of Equation 6 (ΔS_{ads}) depends only on fractional occupancy and reduced quantities. Although polyatomic gases have additional degrees of freedom from internal vibrational and rotational modes, for many adsorbate-adsorbent systems, these internal vibrational and rotational modes are only negligibly altered upon physisorption^{13,14} and do not significantly contribute to ΔS_{ads} . The assumption that rotational modes remain largely unchanged upon physisorption may break down in special circumstances, particularly in pores small enough to inhibit rotational modes.

The left-hand side of Equation 6 depends on the isosteric enthalpy of adsorption, a proxy metric of the physisorption binding-site energies. We first consider an idealized adsorbent with completely homogeneous binding-site energies and no adsorbate-adsorbate interactions. Under these assumptions, ΔH_{ads} is a constant for an ideal gas-adsorbent system, independent of pressure, or fractional occupancy at a fixed reduced temperature. These assumptions are later relaxed.

To begin, we assume that the isosteric enthalpy of adsorption is proportional to the critical temperature of the adsorptive species,⁵ as detailed in the Supporting Information (S5, S6).

$$\Delta H_{ads} = c_1 T_c \quad (11)$$

Here c_1 is an undetermined (adsorbent specific) coefficient and the left-hand side of Equation 6 becomes

$$\frac{\Delta H_{ads}}{T} = \frac{c_1 T_c}{T} \quad (12)$$

By substituting Equation 1 into Equation 12

$$\frac{\Delta H_{ads}}{T} = \frac{c_1}{T^R} \quad (13)$$

Hence under the idealized assumptions above, the left-hand side of Equation 6 only depends on reduced quantities. Since both sides of Equation 6 only depend on reduced quantities and fractional occupancy, the fractional occupancy of distinct gases individually adsorbed on a specific idealized adsorbent must be equal at corresponding conditions.

4.2 Heterogeneities and Adsorbate-Adsorbate Interactions

Real adsorbents typically exhibit a heterogeneous distribution of binding sites. Such a distribution of binding-site energies leads to an isosteric heat ($-\Delta H_{ads}$) that decreases as a function of fractional occupancy as the most favorable sites are filled first. The distribution of binding sites is unique to the adsorbent and depends on pore-size distribution, surface structure, and chemical homogeneity. One may posit that each adsorbent has a characteristic binding-site energy distribution that varies with fractional occupancy and is proportional to the critical temperature of the adsorptive species, but is otherwise independent of the adsorptive species at corresponding conditions (see Supporting Information, S5, S6). In this approximation, c_f is no longer a constant in Equation 11. Instead c_f becomes a function of fractional occupancy that is unique to each adsorbent, but independent of the adsorptive species at corresponding conditions.

Furthermore, cooperative adsorbate-adsorbate interactions are important in some physisorptive systems. In these systems, favorable interactions can lead to an isosteric heat that

increases as a function of fractional occupancy^{6,7}. The contribution of these interactions is assumed to be proportional to the product of the critical temperature, T_c , and a function that depends only on fractional occupancy, $f(\theta)$, at a fixed reduced temperature (see Supporting Information, S7). The expression for ΔH_{ads} in Equation 11 is thus modified by adding a term that is proportional to $f(\theta)T_c$:

$$\frac{\Delta H_{ads}}{T} = \frac{c_1(\theta)T_c + c_2f(\theta)T_c}{T} \quad (14)$$

Here c_2 is an undetermined coefficient that is independent of the adsorptive species at corresponding conditions. By substitution

$$\frac{\Delta H_{ads}}{T} = \frac{c_1(\theta) + c_2f(\theta)}{T^R} \quad (15)$$

The left-hand side of Equation 6 remains approximately independent of the adsorptive species, even upon taking into account binding-site heterogeneity and adsorbate-adsorbate interactions (Equation 15). Consequently, Equation 6 only depends on reduced quantities and the fractional occupancy, consistent with the proposed Law of Corresponding States for gas physisorption.

4.3 BET Model

A simple extension of the Langmuir model to incorporate multiple layers of adsorption was worked out by Brunauer, Emmett, and Teller and is known as BET Theory¹⁵. This theory is widely used to determine the surface area of porous materials and gives the fractional occupancy (θ) as a function of pressure (P), saturation pressure (P_θ), and a parameter, c_{BET} .

$$\theta = \frac{c_{BET} \frac{P}{P_0}}{\left(1 - \frac{P}{P_0}\right) \left(1 - \frac{P}{P_0} + c_{BET} \frac{P}{P_0}\right)} \quad (16)$$

$$c_{BET} = e^{\frac{(-\Delta H_{ads} - H_l)}{RT}} \quad (17)$$

The parameter c_{BET} depends on the heat of adsorption for the first layer, $-\Delta H_{ads}$, the heat of liquefaction of the adsorbate, H_b , and the temperature, T . The assumption that ΔH_{ads} is proportional to T_c has been previously justified. We may similarly assume that H_l is proportional to T_c (see Supporting Information, Section S10). Finally, we assume that for a given gas, P_0 is proportional to P_c , allowing Equation 16 to be reduced as:

$$\theta \propto \frac{\left(e^{\frac{c_3}{RT^R}}\right)(PR)}{(1-PR) \left(1-PR + \left(e^{\frac{c_3}{RT^R}}\right)(PR)\right)} \quad (18)$$

In this expression, c_3 is the factor relating the heat of adsorption and the heat of liquefaction. Equation 18 gives the fractional occupancy in terms of only reduced parameters, consistent with the Law of Corresponding States for physisorption.

4.4 Pore-Filling Model

The similarity between the Law of Corresponding States and Dubinin-Polanyi theory was recently noted by Sircar et al.⁵ Here we further develop this insight to show the importance of fractional occupancy to the Law of Corresponding States for physisorption.

Specifically, we consider a pore-filling model of adsorption in the form of the Dubinin-Astakhov equation:¹⁶

$$\theta = e^{-\left(\frac{RT \ln\left(\frac{P_0}{P}\right)}{E}\right)^\chi} \quad (19)$$

In this equation, T is the temperature, P is the pressure, P_0 is the equilibrium vapor pressure, E is the characteristic binding energy, and χ is an adsorbent-specific heterogeneity parameter.

$$E = \beta E_0 \quad (20)$$

$$\beta = \frac{\alpha}{\alpha_0} \quad (21)$$

The affinity coefficient (β) relates the characteristic binding energy of a sample adsorbate (E) to that of the standard adsorbate (E_0) and depends on the ratio of their static polarizabilities, α and α_0 , respectively. The adsorbate polarizability is assumed to be proportional to the critical temperature of the adsorptive species (see Supporting Information, S5).

Equation 19 then reduces to:

$$\frac{(-\ln(\theta))^{\frac{1}{\chi}}}{R} = \frac{T \ln\left(\frac{P_0^R}{P^R}\right)}{c_4 T_c} = \frac{T^R \ln\left(\frac{P_0^R}{P^R}\right)}{c_4} \quad (22)$$

where

$$P_0^R = \frac{P_0}{P_c} \quad (23)$$

The undetermined constant, c_4 , is derived from the polarizability and characteristic binding energy of the standard adsorbate. Both sides of Equation 22 are independent of the adsorptive

species at corresponding conditions, consistent with the Law of Corresponding States for gas physisorption.

5. Anomalous Surface Thermodynamics

As we previously reported, both methane and krypton physisorption on ZTC yield anomalous surface thermodynamics at supercritical temperatures.^{11,6,7} Methane and krypton isotherms were fitted with a superposition of Langmuir isotherms to extract thermodynamic quantities^{11,6,7}. This yields analytically differentiable fits that are useful in determining the absolute adsorption, and the isosteric enthalpy of adsorption.^{11,6,7} On ZTC, the isosteric heats of methane and krypton adsorption increase with fractional occupancy, a property that is attributed to enhanced adsorbate-adsorbate interactions within the uniquely nanostructured pores.

From Equation 7, the molar enthalpy of the adsorbed phase, H_a (as a function of absolute adsorption) was determined by adding the isosteric enthalpy of adsorption (ΔH_{adv}) to the gas-phase enthalpy values (H_g) at the same conditions (obtained from REFPROP¹⁷). On ZTC, enhanced adsorbate-adsorbate interactions cause the low-temperature adsorbed-phase enthalpies to decrease toward minimum, most favorable values, which are reached at moderate fractional occupancies (Figure 3).

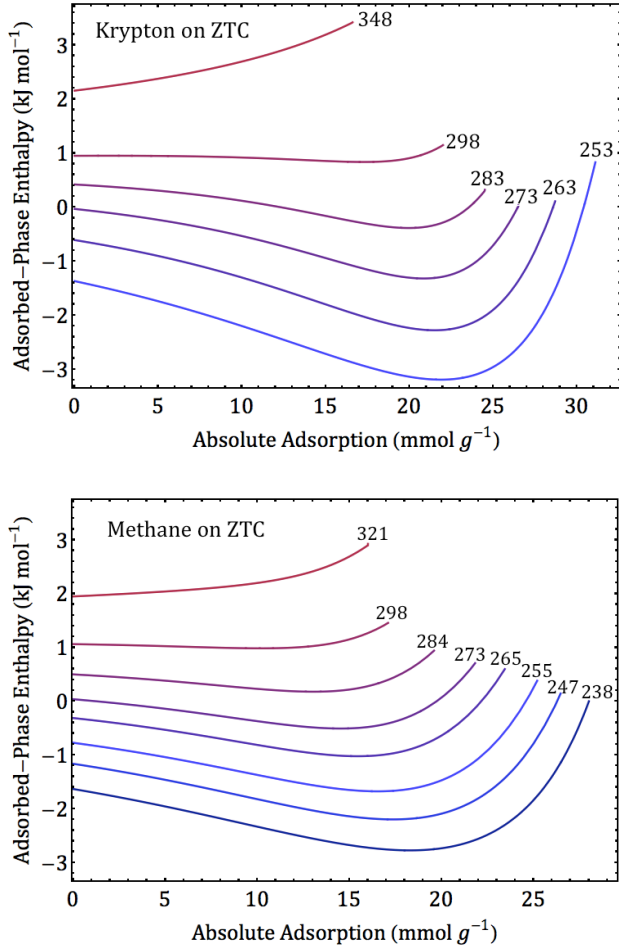


Figure 3. Adsorbed-phase enthalpies of krypton and methane on ZTC. Labels are temperatures in K.

The adsorbed-phase enthalpies may also be plotted as a function of the average intermolecular spacing in the adsorbed phase (x_{avg}) (Figure 4). Here x_{avg} was estimated by dividing the micropore volume of ZTC (V_{mic}), as measured by the Dubinin-Radushkevich method^{18,19}), by the quantity of absolute adsorption (n_a) and taking the cube root.⁷

$$x_{avg} = \left(\frac{V_{mic}}{n_a} \right)^{\frac{1}{3}} \quad (24)$$

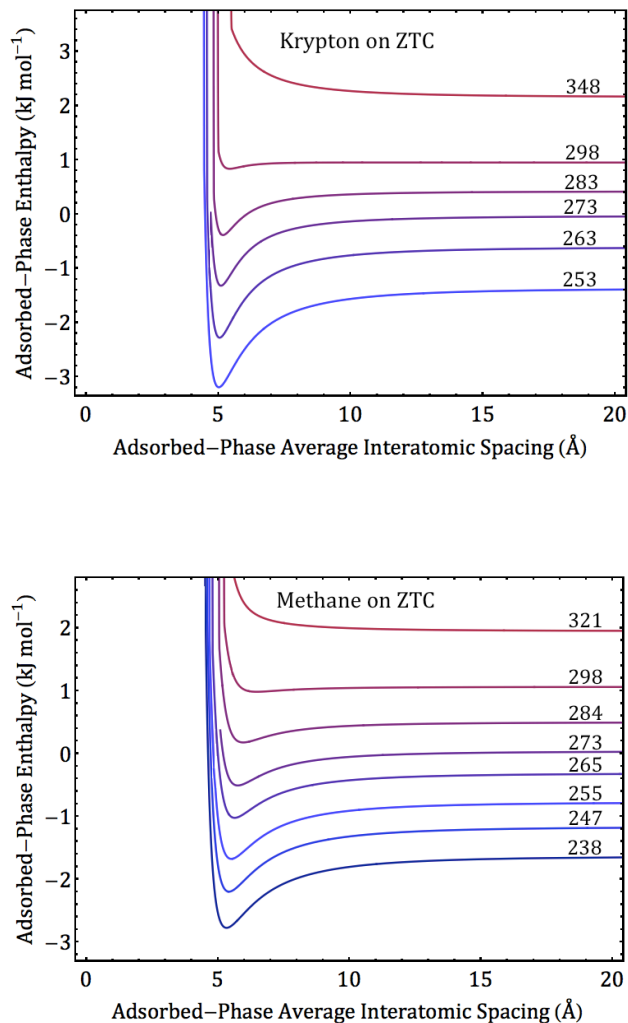


Figure 4. Adsorbed-phase enthalpies of methane and krypton on ZTC, as a function of x_{avg} . Labels are temperatures in K.

As shown in Figure 4, the adsorbed-phase enthalpies (as a function of x_{avg}) change with temperature and resemble a 12-6 Lennard-Jones potential. The deepest “potential wells” are observed at the lowest temperatures. The significant temperature dependence shows that the enhanced adsorbate-adsorbate interactions are disrupted by thermal motion, and suggests

that they may be modeled with a cooperative interaction model such as the Ising model. The heat capacity of the adsorbed phase at constant pressure (C_P) is determined from the adsorbed-phase enthalpy (Figure 5).

$$C_P = \left. \frac{dH_a}{dT} \right|_P \quad (25)$$

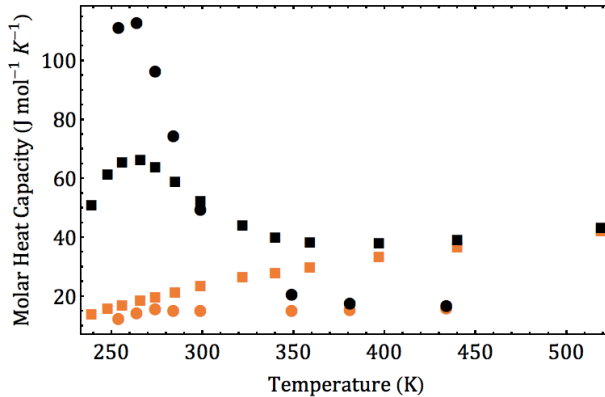


Figure 5. Constant pressure heat capacities of methane (squares) and krypton (circles) adsorbed phases on ZTC (black) and MSC-30 (orange) at an example pressure of 2 MPa.

For both methane and krypton there is good agreement between adsorbed-phase heat capacities at high temperatures for both ZTC and MSC-30. In the case of krypton, a monatomic gas, the C_P on ZTC at high temperatures and the C_P on MSC-30 at all temperatures are in good agreement with the C_P for an ideal two-dimensional gas ($16.6 \text{ J mol}^{-1} \text{ K}^{-1}$). At low temperatures, however, the C_P of both gases are significantly larger on ZTC than on MSC-30, with values that exceed even the liquid-phase heat capacities (methane $\sim 55.7 \text{ J}$

$\text{mol}^{-1} \text{K}^{-1}$ and krypton $\sim 44.7 \text{ J mol}^{-1} \text{K}^{-1}$)¹⁷. These unexpectedly large adsorbed-phase heat capacities may be attributed to a phase transition in the adsorbed phase on the surface of ZTC.

6. Model for Cooperative Interactions

As temperature is increased, the effects of adsorbate-adsorbate interactions decrease, and disappear as the slopes in Figure 3 go to zero at a critical temperature (T_θ) of $\sim 300 \text{ K}$. Figure 5 indicates the presence of a phase transition (in the adsorbed phase) around 270 K . We assume that below T_θ , two phases arise: a vacancy-rich phase with a low concentration of occupied sites (α'), and an adsorbate-rich phase with a high concentration of occupied sites (α'') and more adsorbate-adsorbate interactions. We expect an unmixing phase diagram where the concentration of occupied sites in the α' and α'' phases are temperature dependent. The simplest phase diagram is symmetric, so these concentrations, $c_{\alpha'}$ and $c_{\alpha''}$, are related by

$$c_{\alpha'} = 1 - c_{\alpha''} \quad (26)$$

The average adsorbate-adsorbate interaction energy per adsorbed molecule (U_{avg}) should be dominated by the interactions in the adsorbate-rich α'' phase, with phase fraction $F_{\alpha''}$

$$F_{\alpha''} = \frac{\theta + c_{\alpha''} - 1}{2c_{\alpha''} - 1} \quad (27)$$

For simplicity we consider the case when $\theta=0.5$ and thus equal phase fractions of 0.5 for all temperatures. If we assume (as in the point approximation) that the arrangement of molecules within the “clustered” α'' phase is random and that each nearest-neighbor pair has an interaction strength of ϵ (from the Lennard-Jones potential)⁹, then for $\theta=0.5$

$$U_{avg} = \frac{z\varepsilon c_{\alpha''}^2}{2} \quad (28)$$

With the following definitions

$$L = 2c_{\alpha''} - 1 \quad (29)$$

$$\frac{1+L}{1-L} = e^{\left(\frac{2T_0L}{T}\right)} \quad (30)$$

the unmixing problem is transformed to the Bragg-Williams ordering problem with one order parameter, L .²⁰ By substitution

$$U_{avg} = \frac{z\varepsilon\left(\frac{L+1}{2}\right)^2}{2} \quad (31)$$

In the context of this model, cooperative adsorbate-adsorbate interactions on ZTC at temperatures below T_0 are consistent with the Law of Corresponding States for physisorption as explained in Section 4.2 and elaborated on in the Supporting Information, Section S7.

For experimental comparison, for each measured temperature, we determined the difference between the minimum enthalpy ($\theta \approx 0.5$) and the low coverage enthalpy ($\theta \approx 0$) (in Figure 3) as a proxy measure of U_{avg} . These “potential well” depths were then normalized by

$\frac{z\varepsilon}{2}$ so they could be compared directly to $\left(\frac{L+1}{2}\right)^2$ in Figure 6, per Equation 31. In Figure 6,

we set $T_0 = 300$ K and assume $z = 4$ (square-lattice).

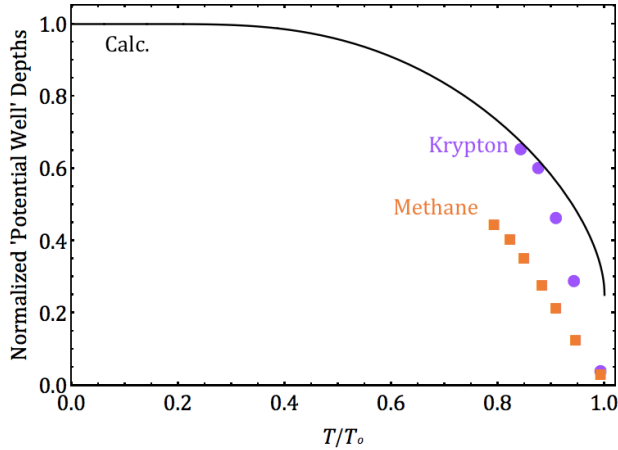


Figure 6. Normalized “potential well” depths of methane and krypton on ZTC, compared to calculated $\left(\frac{L+1}{2}\right)^2$.

Figure 6 compares the measured adsorbate-adsorbate interaction enthalpies to thermal trends from the Ising model. Qualitative similarities between the measured and modeled temperature dependence support the hypothesis of cooperative adsorbate-adsorbate interactions on ZTC. The observed deviations are not surprising for such a simple model and uncertainty in the n_{max} , T_0 and z parameters.

7. Conclusions

The principle that distinct gases have similar adsorptive fractional occupancies at corresponding conditions on the same adsorbent is established as a novel Law of Corresponding States for gas physisorption. This principle is tested empirically using measurements of methane, krypton, and ethane physisorption on ZTC, MSC-30, and CNS-201 at reduced temperatures of 1.25 ± 0.02 and 1.38 ± 0.03 . Reasonable agreement is found

across different size gases with discrepancies of less than 25%. Accordingly this principle is useful for estimating pure gas isotherms, though should not be considered a replacement for experimental isotherm data. Further support is obtained from statistical mechanics wherein the validity of this principle as a first approximation is established for a number of conditions. The principle of corresponding states proves successful even in the presence of cooperative adsorbate-adsorbate interactions, which were modeled using the Ising model in a low-level approximation.

Acknowledgement:

This work was sponsored as a part of EFree (Energy Frontier Research in Extreme Environments), an Energy Frontier Research Center funded by the US Department of Energy, Office of Science, Basic Energy Sciences under Award Number DE-SC0001057.

References:

1. Guggenheim, E. A. The Principle of Corresponding States. *J. Chem. Phys.* **1945**, *13*, 253-261.
2. Reid, R.; Prausnitz, J.; Sherwood, T. *The Properties of Gases and Liquids*; McGraw-Hill Book Company: New York, 1977.
3. Quinn, D. F. Supercritical Adsorption of 'Permanent' Gases under Corresponding States on Various Carbons. *Carbon* **2002**, *40*, 2767-2773.
4. Kim, H. Y.; Lueking, A. D.; Gatica, S. M.; Johnson, J. K.; Cole, M. W. A Corresponding States Principle for Physisorption and Deviations for Quantum Fluids. *Mol. Phys.* **2008**, *106*, 1579-1585.
5. Sircar, S.; Pramanik, S.; Li, J.; Cole, M. W.; Lueking, A. D. Corresponding States Interpretation of Adsorption in Gate-Opening Metal-Organic Framework Cu(dhbc)(2)(4,4'-bpy). *J. Colloid Interface Sci.* **2015**, *446*, 177-184.
6. Stadie, N. P.; Murialdo, M.; Ahn, C. C.; Fultz, B. Anomalous Isothermic Enthalpy of Adsorption of Methane on Zeolite-Templated Carbon. *J. Am. Chem. Soc.* **2013**, *135*, 990-993.
7. Murialdo, M.; Stadie, N. P.; Ahn, C. C.; Fultz, B. Krypton Adsorption on Zeolite-Templated Carbon and Anomalous Surface Thermodynamics. *Langmuir* **2015**, *31*, 7991-7998.
8. Murialdo, M.; Stadie, N. P.; Ahn, C. C.; Fultz, B. Observation and Investigation of Increasing Isothermic Heat of Adsorption of Ethane on Zeolite-Templated Carbon. *J. Phys. Chem. C* **2015**, *119*, 944-950.
9. Talu, O.; Myers, A. L. Reference Potentials for Adsorption of Helium, Argon, Methane, and Krypton in High-Silica Zeolites. *Colloid. Surf. A Physicochem. Eng. Asp.* **2001**, *187*, 83-93.
10. Tee, L. S.; Gotoh, S.; Stewart, W. E. Molecular Parameters for Normal Fluids - Lennard-Jones 12-6 Potential. *Ind. Eng. Chem. Fundam.* **1966**, *5*, 356-363.
11. Stadie, N. P.; Murialdo, M.; Ahn, C. C.; Fultz, B. Unusual Entropy of Adsorbed Methane on Zeolite-Templated Carbon. *J. Phys. Chem. C* **2015**, *119*, 26409-26421.
12. Dabrowski, A. Adsorption - From Theory to Practice. *Adv. Colloid Interface Sci.* **2001**, *93*, 135-224.
13. Campbell, C. T.; Sellers, J. R. V. The Entropies of Adsorbed Molecules. *J. Am. Chem. Soc.* **2012**, *134*, 18109-18115.
14. Lundqvist, B. I. Theoretical Aspects of Adsorption. In *Interaction of Atoms and Molecules with Solid Surfaces*; Bortolani, V.; March, N. H.; Tosi, M. P., Eds.; Plenum Press: New York, 1990; 213-254.
15. Brunauer, S.; Emmett, P. H.; Teller, E. Adsorption of Gases in Multimolecular Layers. *J. Am. Chem. Soc.* **1938**, *60*, 309-319.
16. Burevski, D. The Application of the Dubinin-Astakhov Equation to the Characterization of Microporous Carbons. *Colloid Polym. Sci.* **1982**, *260*, 623-627.
17. Lemmon, E. W.; Huber, M. L.; McLinden, M. O. *NIST Standard Reference Database 23: Reference Fluid Thermodynamic and Transport Properties*, version 8.0; National Institute of Standards and Technology: Gaithersburg, MD, 2007; CD-ROM.

18. Dubinin, M. M.; Radushkevich, L. V. Equation of the Characteristic Curve of Activated Charcoal. *Proc. Acad. Sci. USSR, Phys. Chem. Sect.* **1947**, *55*, 331-337.
19. Nguyen, C.; Do, D. D. The Dubinin-Radushkevich Equation and the Underlying Microscopic Adsorption Description. *Carbon* **2001**, *39*, 1327-1336.
20. Pathria, R. K.; Beale, P. D. *Statistical Mechanics*; Butterworth-Heinemann: New York, 2011.

Chapter 9

Supporting Information for Chapter 8

M. Murialdo, N.P. Stadie, C.C. Ahn, and B. Fultz, “A Generalized Law of Corresponding States for the Physisorption of Classical Gases with Cooperative Adsorbate-Adsorbate Interactions,” *J. Phys. Chem. C*, 120, 11847 (2016).

(Supporting Information)

DOI: 10.1021/acs.jpcc.6b00289

<http://pubs.acs.org/doi/abs/10.1021/acs.jpcc.6b00289>

S1. Adsorbent Materials

MSC-30

MSC-30 (Maxsorb) is a microporous superactivated carbon obtained from Kansai Coke & Chemicals Company Ltd. (Japan). As determined by nitrogen adsorption and BET analysis, MSC-30 has a surface area of $3244 \pm 28 \text{ m}^2 \text{ g}^{-1}$. Using nitrogen adsorption data and a slit-pore model, NLDFT pore-size analysis¹ was conducted to determine the pore-size distribution. MSC-30 has a broad range of pore sizes (from 6 to 35 Å). Over 40% of the micropore volume is contained in pores of greater than 21 Å in width. The total micropore volume was found to be $1.54 \text{ cm}^3 \text{ g}^{-1}$ by the Dubinin-Radushkevich method. The skeletal density was measured by helium pycnometry and determined to be 2.1 g cm^{-3} . Cu K α X-ray diffraction of MSC-30 gave a broad peak at $2\theta=34^\circ$, in accordance with that reported for AX-21. The elemental composition (CHN) was determined via the Dumas method² in combustion experiments, indicating that 1.16 wt% of MSC-30 is hydrogen. Results from XPS experiments on MSC-30 are summarized in Table S1.³

Table S1. Summary of XPS Data on MSC-30 and ZTC

| peak position (eV) | 285.0 | 285.7 | 286.4 | 287.3 | 288.1 | 289.4 | 290.2 | 291.5 |
|-----------------------|---------------------|---------------------|-------|-------|-------|-------|-------|-------|
| component | C-C sp ² | C-C sp ³ | C-OR | C-O-C | C=O | COOR | - | - |
| ZTC | 53.4 | 18.0 | 8.6 | 6.0 | 1.1 | 4.2 | 1.0 | 7.7 |
| MSC-30 | 48.0 | 18.8 | 6.8 | 4.8 | 6.1 | 4.2 | 3.6 | 7.7 |

CNS-201

CNS-201 is a microporous activated carbon obtained from A. C. Carbone Inc. (Canada). As determined by nitrogen adsorption and BET analysis, CNS-201 has a surface area of $1095 \pm 8 \text{ m}^2 \text{ g}^{-1}$. Using nitrogen adsorption data and a slit-pore model, NLDFIT pore-size analysis was conducted to determine the pore-size distribution. CNS-201 has a three dominant pore widths of 5.4, 8.0, and 11.8 Å, containing roughly 50%, 20%, and 15% of the total micropore volume respectively. The micropore volume was found to be $0.45 \text{ cm}^3 \text{ g}^{-1}$ by the Dubinin-Radushkevich method^{4,5}. The skeletal density was measured by helium pycnometry and determined to be 2.1 g cm^{-3} .

Zeolite-Templated Carbon (ZTC)

ZTC is a templated carbon synthesized using zeolite NaY and a process described elsewhere.^{6,7} As determined by nitrogen adsorption and BET analysis, ZTC has a surface area of $3591 \pm 60 \text{ m}^2 \text{ g}^{-1}$. Using nitrogen adsorption data and a slit-pore model, NLDFIT pore-size analysis was conducted to determine the pore-size distribution. ZTC has a narrow pore-size distribution centered at 12 Å. Over 90% of the micropore volume is contained in pores of

widths between 8.5 and 20 Å. The total micropore volume was found to be 1.66 cm³ g⁻¹ by the Dubinin-Radushkevich method. The skeletal density was measured by helium pycnometry and determined to be 1.8 g cm⁻³. Cu K α X-ray diffraction of ZTC produced a sharp peak at $2\theta=6^\circ$, indicative of the template periodicity of ~ 15 Å. The elemental composition (CHN) was determined using the Dumas method in combustion experiments, indicating that 2.44 wt% of MSC-30 is hydrogen. Results from XPS experiments on ZTC are summarized in Table S1. TEM analysis has also provided evidence of the periodic structure of ZTC.³

S2. Approximation of n_{max}

All three materials tested are predominantly microporous. The maximum adsorption quantity (n_{max}) was estimated as the product of the total micropore volume and the liquid density of the adsorptive species at its triple point. This assumes complete micropore filling at a maximal density given by the liquid-phase density. The micropore volumes of each adsorbent were determined by applying the Dubinin-Radushkevich method to nitrogen adsorption isotherms measured at 77 K.³ The liquid densities were obtained from REFPROP⁸. Both the micropore volumes and the liquid densities are listed in Table S2 along with the as-determined values for n_{max} .

Table S2. Liquid Molar Densities, Adsorbent Micropore Volumes,
and Estimated n_{max} Values

| | density (mol dm ⁻³) | ZTC | MSC-30 | CNS-201 |
|--------------------------------------|---------------------------------|------|--------|---------|
| micropore volume (cm ⁻³) | | 1.66 | 1.54 | 0.45 |
| krypton | 29.2 | 48.5 | 45.0 | 13 |
| methane | 28.1 | 46.7 | 43.3 | 13 |
| ethane | 21.7 | 36.0 | 33.4 | 9.8 |

S3. Comparison of Fractional Occupancies at Corresponding Conditions

While absolute adsorption is of greater physical relevance, excess adsorption is the experimentally-determined quantity in physisorption experiments. To obtain absolute adsorption uptake quantities (n_a) from excess adsorption quantities (n_e) we used Gibb's definition of excess adsorption

$$n_e = n_a - V_{ads}\rho_g \quad (S1)$$

where ρ_g is the gas-phase density. We fit the unknown absolute adsorption uptake quantities and adsorption volumes (V_{ads}) with a superposition of Langmuir isotherms⁹ to obtain

$$n_e = (n_{max} - V_{max}\rho_g) \left(\sum_i \alpha_i \left(\frac{K_i P}{1 + K_i P} \right) \right) \quad (S2)$$

where K_i is the equilibrium constant of the i th Langmuir isotherm, α_i is the weighting factor for the i th Langmuir isotherm ($\sum_i \alpha_i = 1$), and V_{max} is the maximum adsorption volume. While the number of Langmuir isotherms (i) may be adjusted, we found that setting $i=2$ gives high quality fits with a minimum number of parameters. Moreover many of the fitting parameters hold physical significance that may be verified by comparison to independent estimates. For $i=2$, the absolute adsorption is given by

$$n_a = n_{max} \left((1 - \alpha) \left(\frac{K_1 P}{1 + K_1 P} \right) + \alpha \left(\frac{K_2 P}{1 + K_2 P} \right) \right) \quad (S3)$$

This fitting procedure has been described in more detail elsewhere.⁹

Having determined absolute adsorption, we compare the fractional occupancies of methane, krypton and ethane on ZTC and MSC-30 at corresponding reduced temperatures of

1.25 \pm 0.02 and 1.38 \pm 0.03 and corresponding reduced pressures (Figure S1). CNS-201 was not considered due to an insufficient number of experimental isotherms.

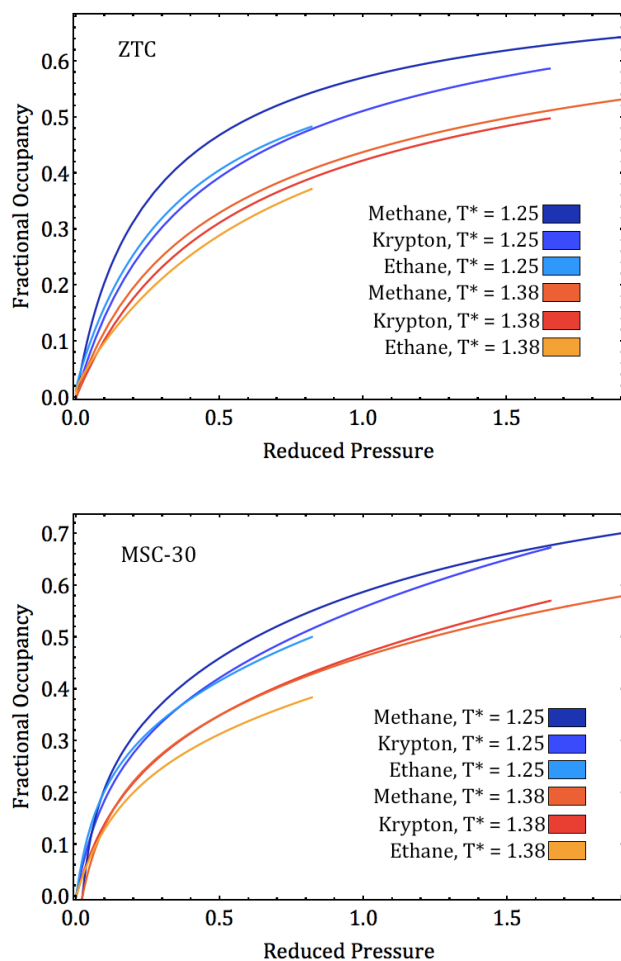


Figure S1. Comparison of krypton, methane and ethane fractional occupancies on ZTC and MSC-30 at corresponding conditions.

As with the excess occupancies, the fractional occupancies compared at corresponding conditions are in reasonable agreement with one another. Additional errors may have been introduced in the fitting procedure.

S4. Assumption that S_g (in Reference to S_{L1}) is Well Approximated by $f(T^R, P^R)$ for Monatomic Gases with Similar Critical Volumes

According to the Trouton-Hildebrand-Everett rule, “the entropy of vaporization for normal liquids is the same when evaporated to the same concentration”.¹⁰ Despite notable exceptions (e.g. due to hydrogen bonding), the Trouton-Hildebrand-Everett rule is generally accurate.^{11,12} The entropy of vaporization (ΔS_{vap}) is defined as the difference between the gas-phase entropy (S_{g1}) and the liquid-phase entropy (S_{L1}), where the “1” subscript indicates that the entropies are measured at the normal boiling temperature.

$$\Delta S_{vap} = S_{g1} - S_{L1} \quad (S4)$$

For a monatomic gas at dilute conditions, additional changes to the gas-phase enthalpy due to increasing temperature are accounted for as

$$\Delta S_{g\ 1 \rightarrow 2} = \frac{3}{2} R \ln\left(\frac{T}{T_{BP}}\right) \quad (S5)$$

where the subscript “ $g\ 1 \rightarrow 2$ ” indicates that the entropy change takes the gas from the normal boiling temperature, 1, to a new temperature, 2. Noting the proportionality between the normal boiling temperature and the critical temperature for gases with similar V_c

$$\Delta S \propto \frac{3}{2} R \ln(T^R) \quad (S6)$$

For gases with similar V_c , the gas concentration, or equivalently the molar volume (V), is approximately proportional to V^R , and the difference between S_{g2} and S_{L1} is well approximated as a function that depends only on T^R and V^R , $f(T^R, V^R)$. Figure S2 compares the gas-phase entropies (measured in reference to S_{L1}) of three monatomic gases with similar critical volumes (argon, $0.096\text{ dm}^3\text{ mol}^{-1}$; krypton $0.12\text{ dm}^3\text{ mol}^{-1}$; xenon $0.15\text{ dm}^3\text{ mol}^{-1}$) and

one monatomic gas with a different critical volume (neon, $0.051 \text{ dm}^3 \text{ mol}^{-1}$) at corresponding conditions.⁸ The gas-phase entropies of argon, krypton, and xenon are all in good agreement with one another, while that of neon deviates significantly due to its smaller critical volume and quantum effects.

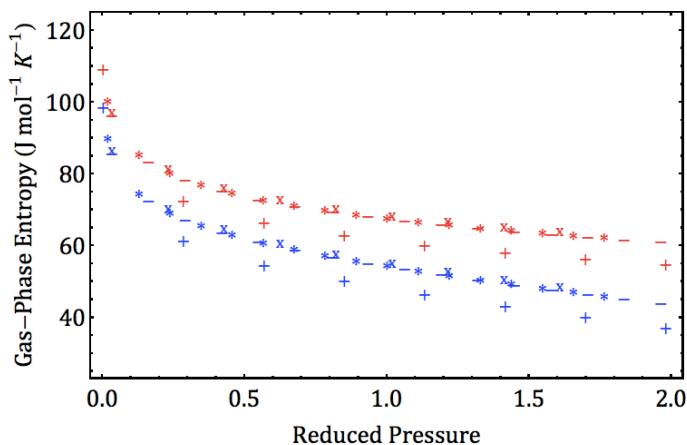


Figure S2. Gas-Phase molar entropies of neon (+), argon (-), krypton (*), and xenon (x) at reduced temperatures of 1.25 (blue) and 2.07 (red), at corresponding reduced pressures.

S5. Assumption that ΔH_{ads} is Proportional to T_c

For interactions from purely London dispersion forces, ΔH_{ads} is expected to be proportional to the static polarizability (α) of the adsorbate following London's theory¹³. This assumption is valid for small and moderately-sized classical molecules (e.g., ethane) that have a fairly uniform charge distribution (e.g., non-polar species without a strong quadrupole moment).

For small and moderately-sized classical molecules that interact through

London dispersion forces, the critical temperature is found to be proportional to the square root of the static polarizability¹⁴. In many cases, however, the curvature is minimal and the trend is essentially linear. This is illustrated for noble gases in Figure S3.

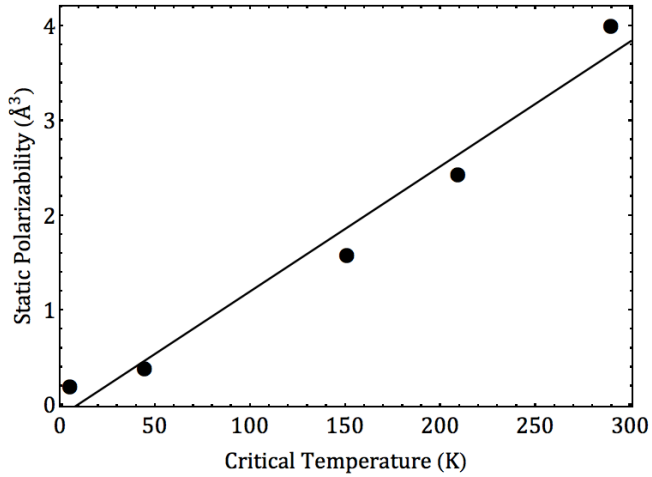


Figure S3. Static polarizability of noble gases¹⁵ as a function of the gas critical temperature⁸. A linear fit is shown.

Therefore, a simple approximation that the critical temperature is directly proportional to the polarizability (α) is acceptable:

$$\alpha \approx c_5 T_c \quad (\text{S7})$$

Here, c_5 is the proportionality constant. It then follows that:

$$\Delta H_{ads} \approx c_6 T_c \quad (\text{S8})$$

$$\frac{(\Delta H_{ads})}{T_c} \approx c_6 \quad (\text{S9})$$

The validity of this approximation is investigated in Table S3, wherein $-\Delta H_{ads}$ is derived experimentally from adsorption measurements (at $\theta \approx 0$ on ZTC, MSC-30, and CNS-201). We find that c_6 is reasonably constant across different gases on the same adsorbent. As is a

commonly employed assumption elsewhere, the effect of temperature on the isosteric enthalpy of adsorption is assumed to be negligible compared to its absolute magnitude.

Table S3. Empirical Values of $\frac{(-\Delta H_{ads})}{T_c}$ for Krypton,

Methane and Ethane on MSC-30, ZTC and CNS-201

| | MSC-30 | ZTC | CNS-201 |
|-----------------|-----------|-----------|-----------|
| krypton | 0.062 | 0.058 | 0.085 |
| methane | 0.076 | 0.072 | 0.097 |
| ethane | 0.069 | 0.066 | 0.080 |
| mean and spread | 0.069±10% | 0.065±11% | 0.087±11% |

The validity of Equation S9 is also investigated by comparing $\frac{(-\Delta H_{ads})}{T_c}$ as a function of fractional occupancy on MSC-30 and ZTC (based on the availability of high pressure isosteric enthalpy of adsorption data at corresponding temperatures). On MSC-30, the $\frac{(-\Delta H_{ads})}{T_c}$ values approximately track one another as they decrease monotonically with fractional occupancy due to binding-site heterogeneity (Figure S4). On ZTC, methane and krypton exhibit anomalous surface thermodynamics at temperatures below T_0 due to cooperative adsorbate-adsorbate interactions. This leads to $\frac{(-\Delta H_{ads})}{T_c}$ values that initially increase with fractional occupancy, but nonetheless approximately track one another (Figure S5) due to the considerations explained in Sections 4.2 (Chapter 8) and S7 (Chapter 9). Additional discrepancies may result from uncertainty in the n_{max} parameter.

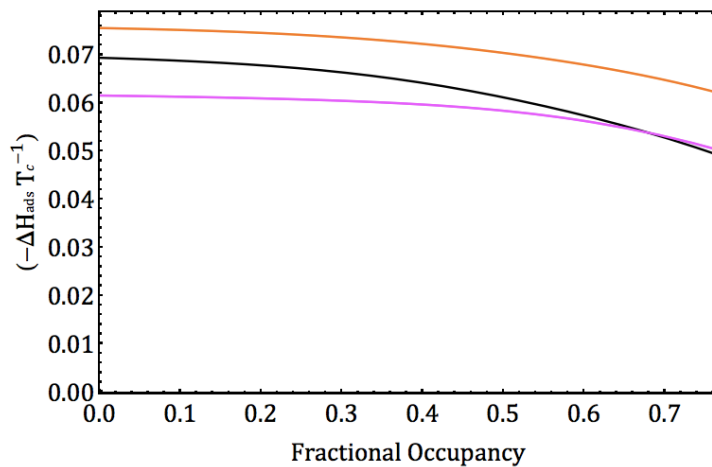


Figure S4. Comparison of $\frac{(-\Delta H_{ads})}{T_c}$ of methane (orange), krypton (purple), and ethane (black) on MSC-30 at a reduced temperature of 1.25.

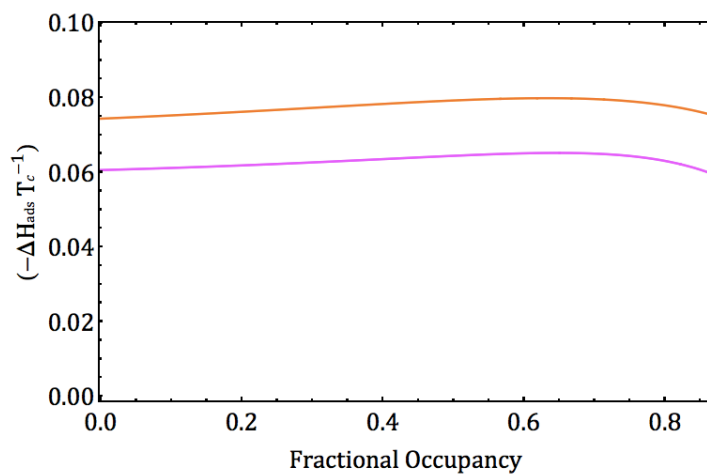


Figure S5. Comparison of $\frac{(-\Delta H_{ads})}{T_c}$ of methane (orange) and krypton (purple) on ZTC at a reduced temperature of 1.25.

S6. Generalizing the Proportionality

Between ΔH_{ads} and T_c to NonIdeal Gases

The molar enthalpy of an ideal gas depends solely on the temperature. This, along with the assumptions in Section 4.1 of Chapter 8, allows for a constant $\frac{-\Delta H_{ads}}{T}$ for multiple gases individually adsorbed on a single adsorbent at a fixed reduced temperature. The enthalpy of a nonideal gas, however, depends on pressure and volume as well as temperature, as illustrated by the case of a van der Waals gas (H_{vdW})

$$H_{vdW} = \frac{3}{2} N k_B T - \frac{N^2 a}{V} + PV \quad (S10)$$

where N is the number of gas molecules, k_B is Boltzmann's constant, T is the temperature, P is the pressure, V is the volume of the system, and a and b are the van der Waals parameters. Expressed as a function of T^R , P^R , and V^R :

$$H_{vdW} = \frac{a}{b} \left[\frac{4NT^R}{9} - \frac{N}{3V^R} + \frac{P^R V^R N}{27} \right] \quad (S11)$$

The van der Waals critical temperature, $T_c = \frac{8a}{27bNk_B}$, can also be included giving:

$$H_{vdW} = \left(\frac{27T_c N k_B}{8} \right) \left[\frac{4NT^R}{9} - \frac{N}{3V^R} + \frac{P^R V^R N}{27} \right] \quad (S12)$$

The gas-phase molar enthalpy (H_g) of a van der Waals gas is therefore proportional to the critical temperature and otherwise depends only on the reduced quantities as:

$$H_g \propto T_c f(T^R, P^R, V^R) \quad (S13)$$

Furthermore, we assume that the adsorbed-phase molar enthalpy (H_a) is proportional to the critical temperature, and otherwise depends only on the fractional occupancy and reduced quantities (as empirically supported by the data in Figure 3 of Chapter 8).

$$H_a \propto T_c f(\theta, T^R, P^R, V^R) \quad (\text{S14})$$

Since the isosteric enthalpy of adsorption is the difference between the gas-phase and adsorbed-phase enthalpies at constant coverage, T_c can be factored out of both:

$$\Delta H_{ads} \propto T_c [f(T^R, P^R, V^R) - f(\theta, T^R, P^R, V^R)] \quad (\text{S15})$$

The isosteric enthalpy of adsorption of a van der Waals gas is therefore proportional to its critical temperature, and otherwise depends only on the fractional occupancy and reduced quantities.

S7. Assumption that the Contributions of Adsorbate-Adsorbate Interactions to ΔH_{ads} are Proportional to $f(\theta)T_c$

Methane and krypton adsorption on ZTC exhibit anomalous surface thermodynamics where the isosteric heats of adsorption increase with coverage.^{16,17} This results from adsorbate-adsorbate interactions that are enhanced by the surface nanostructure. We have previously provided both enthalpic and entropic evidence of adsorbed-phase clustering on ZTC.^{9,17} In this work we draw a connection between the adsorbed-phase clustering and the Ising model by analyzing the temperature dependence of the clustering as an unmixing phase transition. The applicability of this model is supported by considerations of the adsorbed-phase heat capacity (Figure 5 of Chapter 8) and the general temperature dependence of the effect (Figure 6 of Chapter 8). To use the Ising model, we assume the critical temperature of the unmixing phase

transition (T_θ) is proportional to the Lennard-Jones interaction potential (ϵ) of the adsorbate, and hence proportional to the critical temperature of the adsorbate (T_c).¹⁸ We define a reduced phase-transition critical temperature (T_o^R) such that

$$T_o^R = \frac{T}{T_o} \quad (\text{S16})$$

By the transitive property

$$T_o^R \propto T^R \quad (\text{S17})$$

For $T_o^R < 1$, unmixing occurs, and the adsorbate-vacancy binary solid solution separates into a vacancy-rich α' phase and an adsorbate-rich α'' phase. The adsorbate concentration in each phase, $c_{\alpha'}$ and $c_{\alpha''}$, respectively, depends on T_o^R . The relative phase fraction of the α'' phase

($F_{\alpha''}$) is given by the lever rule:

$$F_{\alpha''} = \frac{\theta + c_{\alpha''} - 1}{2c_{\alpha''} - 1} \quad (\text{S18})$$

The adsorbate-adsorbate interaction energy is predominantly from the adsorbate-rich α'' phase. Under the assumption of random ordering (the point approximation), the average adsorbate-adsorbate energy per molecule in the α'' phase, $U_{\alpha''}$, is

$$U_{\alpha''} = \frac{z\epsilon c_{\alpha''}}{2} \quad (\text{S19})$$

where z is the coordination number. The overall adsorbate-adsorbate energy per molecule, U_{avg} in both phases is given by a weighted average of the mean adsorbate energy in each phase and the fraction of adsorbate molecules in each phase

$$U_{avg} = \frac{F_{\alpha'} c_{\alpha'} U_{\alpha'} + F_{\alpha''} c_{\alpha''} U_{\alpha''}}{\theta} \quad (\text{S20})$$

where the energy of the vacancy-rich phase, $U_{\alpha'}$, is assumed to be zero. By substitution we arrive at a general expression to model U_{avg} .

$$U_{avg} = \left(\frac{z\epsilon c_{\alpha'}^2}{2} \right) \left(\frac{\theta + c_{\alpha'} - 1}{2c_{\alpha'} - 1} \right) \left(\frac{1}{\theta} \right) \quad (S21)$$

For a fixed reduced temperature, $c_{\alpha'}$ is a constant. The coordination number, z , is also assumed to be a constant. Equation S21 is thus the product of a function proportional to ϵ and a function $f(\theta)$ that only varies with θ . Notably this equation displays the expected qualitative behaviors, increasing as a function of fractional occupancy at low coverage and leveling off at high coverage. We may make the assumption that ϵ is proportional to T_c ¹⁸ leaving an equation that only varies with $f(\theta)T_c$.

S8. Justification for the Law of Corresponding States in Bulk Gases

The Law of Corresponding States in bulk fluids is well established and can be readily understood by examining the van der Waals equation of state:

$$P = \frac{RT}{V-b} - \frac{a}{V^2} \quad (S22)$$

Here, P is pressure, T is temperature, V is volume, R is the gas constant, and a and b are the van der Waals parameters (unique for each gas). By substituting in the reduced temperature, reduced pressure and reduced volume:

$$P^*P_c = \frac{RT^*T_c}{V^*V_c - b} - \frac{a}{V^*V_c} \quad (S23)$$

The critical quantities in terms of the van der Waals parameters (a and b)¹⁹ are

$$T_c = \frac{8a}{27Rb} \quad (\text{S24})$$

$$P_c = \frac{a}{27b^2} \quad (\text{S25})$$

$$V_c = 3b \quad (\text{S26})$$

Substituting these critical quantities into Equation S23:

$$P^R = \frac{8T^R}{3V^{R-1}} - \frac{3}{V^R} \quad (\text{S27})$$

Equation 11 depends only on reduced quantities, which are by definition identical for all gases at corresponding conditions, thus providing a basis for the Law of Corresponding States in bulk fluids.

S9. Additional Data Compared with Law of Corresponding States for Physisorption

Using experimental physisorption data published elsewhere, the Law of Corresponding States for physisorption is illustrated on three additional adsorbents, each representing a unique class of materials. These examples showcase the importance of the adsorbate molecular volume. Two plots are shown for each adsorbent, the first comparing excess adsorption at corresponding conditions and the second comparing excess occupancies at corresponding conditions. In each case, excess occupancies at corresponding conditions have better agreement than excess adsorption at corresponding conditions. This is especially pronounced for adsorbates that have very different liquid molar volumes (e.g. argon and cyclohexane).

Agot Grade Artificial Nuclear Graphite²⁰

In Figure S6, argon and nitrogen adsorption isotherms on highly pure graphite are compared at a reduced temperature of 0.6 ± 0.01 . Argon and nitrogen have similar van der Waals molar volumes of 0.03201 and 0.0387 L mol⁻¹ respectively. Thus switching from a

comparison of excess adsorption to excess occupancy only minimally improves the agreement between the corresponding isotherms.

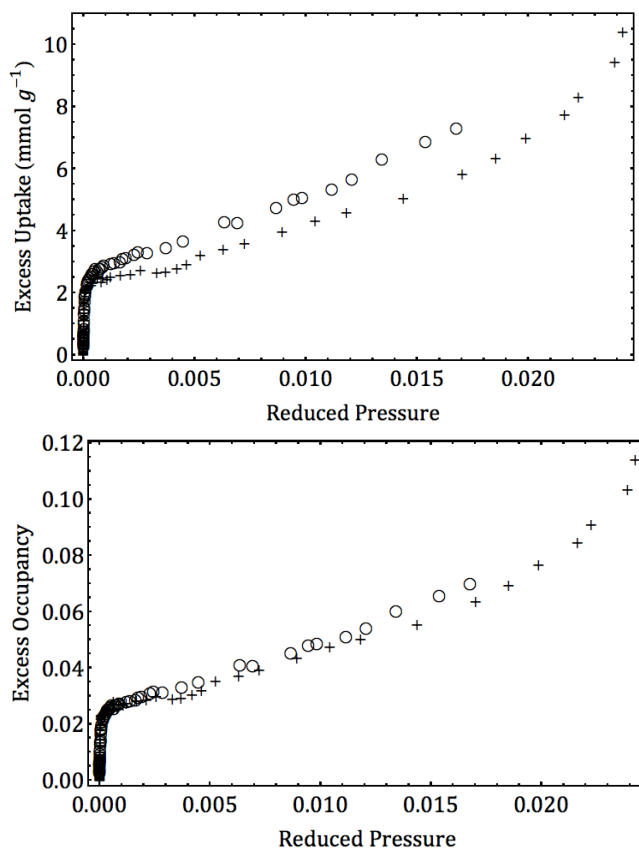


Figure S6. Comparison of excess adsorption (top) and excess occupancy (bottom) of argon (circles) and nitrogen (+) adsorption on Agot grade artificial nuclear graphite at corresponding conditions ($T^R = 0.6 \pm 0.01$).²⁰

Ni(bodc)(ted)_{0.5} Metal-Organic Framework²¹

In Figure S7, argon and cyclohexane adsorption isotherms on Ni(bodc)(ted)_{0.5} are compared at a reduced temperature of 0.57 ± 0.01 . Argon and cyclohexane have dissimilar van der Waals molar volumes of 0.03201 and 0.1424 L mol⁻¹ respectively. This leads to large

discrepancies when comparing excess adsorption that are resolved by comparing excess occupancy.

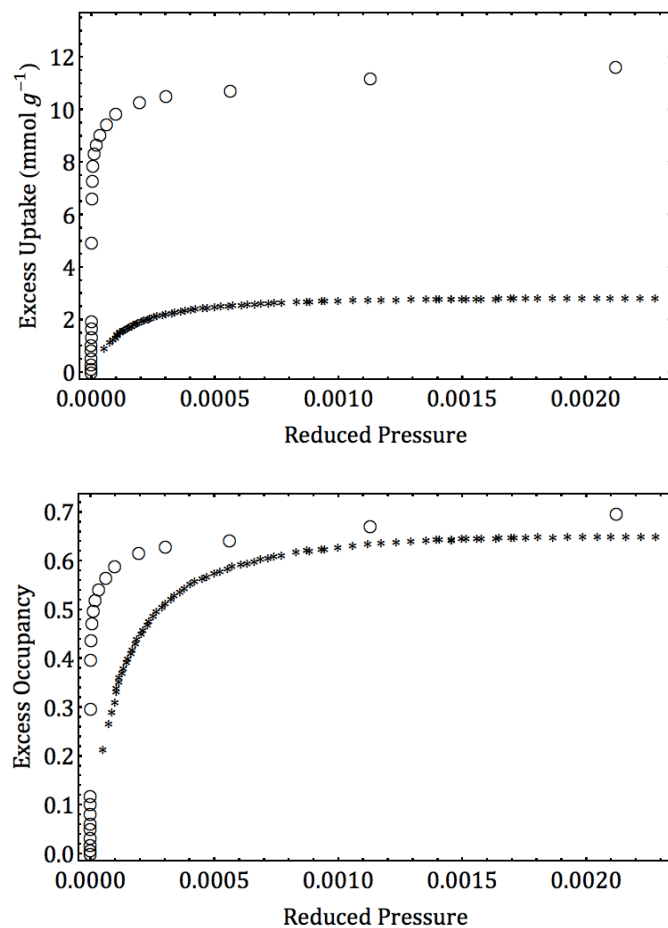


Figure S7. Comparison excess adsorption (top) and excess occupancy (bottom) of argon (circles) and cyclohexane (*) adsorption on $[\text{Ni}(\text{bodc})(\text{ted})_{0.5}]$ at corresponding conditions ($T^{\text{R}} = 0.57 \pm 0.01$).²¹

Zeolite NaX²²

In Figure S8, carbon dioxide, ethane, and sulfur hexafluoride adsorption isotherms on zeolite NaX are compared at a reduced temperature of 0.94 ± 0.02 . The van der Waals molar volumes of carbon dioxide, ethane, and sulfur hexafluoride are 0.04267, 0.0638, and 0.08786 L mol⁻¹, respectively. Comparing excess occupancies rather than excess adsorption improves the

agreement of the isotherms. It is notable that all three gases have similar critical temperatures of 304, 305, and 319 K respectively, and yet the differences in the van der Waals molar volumes yield significant discrepancies when comparing excess adsorption.

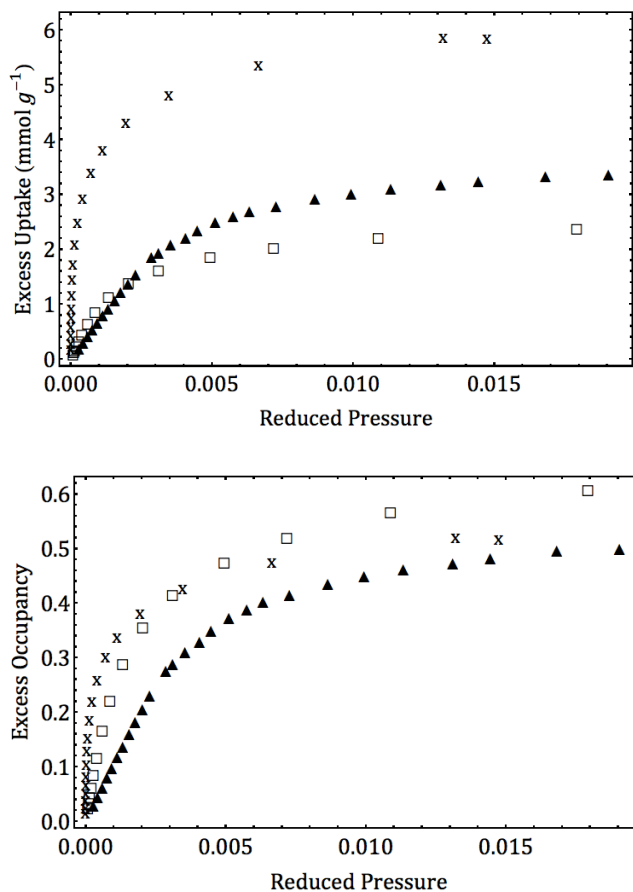


Figure S8. Comparison of excess adsorption (top) and excess occupancy (bottom) of carbon dioxide (x), ethane (triangles), and sulfur hexafluoride (squares) adsorption on zeolite NaX at corresponding conditions ($T^R = 0.94 \pm 0.02$).²²

S10. Heat of Liquefaction vs. Critical Temperature

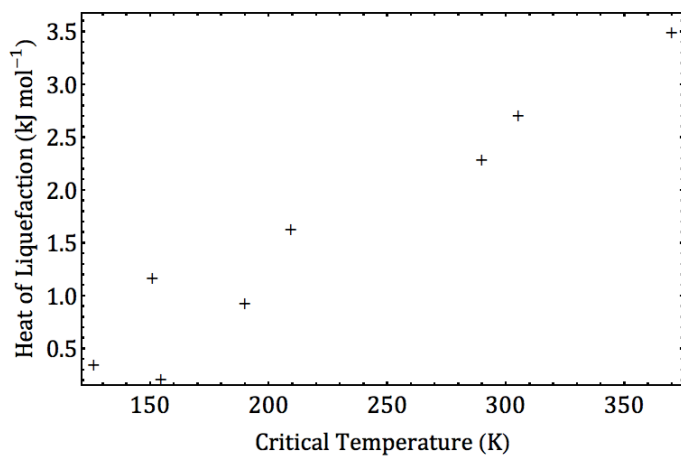


Figure S9. Plotting the heat of liquefaction as a function of critical temperature for moderately-sized classical gases shows an approximately linear correlation.⁸

References:

1. Tarazona, P.; Marconi, U. M. B.; Evans, R. Phase-Equilibria of Fluid Interfaces and Confined Fluids - Nonlocal Versus Local Density Functionals. *Mol. Phys.* **1987**, *60*, 573-595.
2. Dumas, J. B. A Method of Estimating Nitrogen in Organic Material. *Ann. Chim. Phys.* **1833**, *58*, 171-173.
3. Stadie, N. P.; Vajo, J. J.; Cumberland, R. W.; Wilson, A. A.; Ahn, C. C.; Fultz, B. Zeolite-Templated Carbon Materials for High-Pressure Hydrogen Storage. *Langmuir* **2012**, *28*, 10057-10063.
4. Dubinin, M. M.; Radushkevich, L. V. Equation of the Characteristic Curve of Activated Charcoal. *Proc. Acad. Sci. USSR, Phys. Chem. Sect.* **1947**, *55*, 331-337.
5. Nguyen, C.; Do, D. D. The Dubinin-Radushkevich Equation and the Underlying Microscopic Adsorption Description. *Carbon* **2001**, *39*, 1327-1336.
6. Kyotani, T.; Nagai, T.; Inoue, S.; Tomita, A. Formation of New Type of Porous Carbon by Carbonization in Zeolite Nanochannels. *Chem. Mater.* **1997**, *9*, 609-615.
7. Nishihara, H.; Hou, P.-X.; Li, L.-X.; Ito, M.; Uchiyama, M.; Kaburagi, T.; Ikura, A.; Katamura, J.; Kawarada, T.; Mizuuchi, K.; Kyotani, T. High-Pressure Hydrogen Storage in Zeolite-Templated Carbon. *J. Phys. Chem. C* **2009**, *113*, 3189-3196.
8. Lemmon, E. W.; Huber, M. L.; McLinden, M. O. *NIST Standard Reference Database 23: Reference Fluid Thermodynamic and Transport Properties-REFPROP*, version 8.0; National Institute of Standards and Technology: Gaithersburg, MD, 2007; CD-ROM.
9. Stadie, N. P.; Murialdo, M.; Ahn, C. C.; Fultz, B. Unusual Entropy of Adsorbed Methane on Zeolite-Templated Carbon. *J. Phys. Chem. C* **2015**, *119*, 26409-26421.
10. Hildebrand, J. H. The Entropy of Vaporization as a Means of Distinguishing Normal Liquids. *J. Am. Chem. Soc.* **1915**, *37*, 970-978.
11. Hildebrand, J. H. Liquid Structure and Entropy of Vaporization. *J. Chem. Phys.* **1939**, *7*, 233-235.
12. Green, J. A.; Irudayam, S. J.; Henschman, R. H. Molecular Interpretation of Trouton's and Hildebrand's Rules for the Entropy of Vaporization of a Liquid. *J. Chem. Thermodyn.* **2011**, *43*, 868-872.
13. London, F. The General Theory of Molecular Forces. *Trans. Faraday Soc.* **1937**, *33*, 8-26.
14. Bretsznajder, S. *International Series of Monographs in Chemical Engineering: Prediction of Transport and Other Physical Properties of Fluids*; Pergamon Press: New York, 1971.
15. Rice, J. E.; Taylor, P. R.; Lee, T. J.; Almlöf, J. The Determination of Accurate Dipole Polarizabilities Alpha and Gamma for the Noble-Gases. *J. Chem. Phys.* **1991**, *94*, 4972-4979.
16. Stadie, N. P.; Murialdo, M.; Ahn, C. C.; Fultz, B. Anomalous Isothermic Enthalpy of Adsorption of Methane on Zeolite-Templated Carbon. *J. Am. Chem. Soc.* **2013**, *135*, 990-993.

17. Murialdo, M.; Stadie, N. P.; Ahn, C. C.; Fultz, B. Krypton Adsorption on Zeolite-Templated Carbon and Anomalous Surface Thermodynamics. *Langmuir* **2015**, *31*, 7991-7998.
18. Evans, G. J. Cooperative Molecular Behavior and Field Effects on Liquids: Experimental Considerations. In *Dynamical Processes in Condensed Matter*; Evans, M. W., Ed.; John Wiley and Sons: New York, 1985; 293-376.
19. Haentzschel, E. The Calculation of the A and B Constants of van der Waals's Equation from Critical Values. *Ann. Phys.* **1905**, *16*, 565-573.
20. Banaresmunoz, M. A.; Gonzalez, L. V. F.; Llorenta, J. M. M. Adsorption-Isotherms of Nitrogen and Argon on an Agot Grade Artificial Nuclear Graphite at 77-K and 90-K. *Carbon* **1987**, *25*, 603-608.
21. Li, K. H.; Lee, J.; Olson, D. H.; Emge, T. J.; Bi, W. H.; Eibling, M. J.; Li, J. Unique Gas and Hydrocarbon Adsorption in a Highly Porous Metal-Organic Framework Made of Extended Aliphatic Ligands. *Chem. Commun.* **2008**, *46*, 6123-6125.
22. Siperstein, F. R.; Myers, A. L. Mixed-Gas Adsorption. *Aiche J.* **2001**, *47*, 1141-1159.

A Thermodynamic Investigation of Adsorbate-Adsorbate

Interactions of Carbon Dioxide on Nanostructured Carbons

M. Murialdo, C.C. Ahn, and B. Fultz, “A Thermodynamic Investigation of Adsorbate-Adsorbate Interactions of Carbon Dioxide on Nanostructured Carbons,” *AIChE J.* (submitted, 2016).

Abstract

A thermodynamic study of carbon dioxide adsorption on a zeolite-templated carbon (ZTC), a superactivated carbon (MSC-30), and an activated carbon (CNS-201) was carried out at temperatures from 240 to 478 K and pressures up to 5.5 MPa. Excess adsorption isotherms were fitted with generalized Langmuir-type equations, allowing the isosteric heats of adsorption and adsorbed-phase heat capacities to be obtained as a function of absolute adsorption. On MSC-30, a superactivated carbon, the isosteric heat of carbon dioxide adsorption *increases* with occupancy from 19 to 21 kJ mol⁻¹, before decreasing at high loading. This increase is attributed to attractive adsorbate-adsorbate intermolecular interactions as evidenced by the slope and magnitude of the increase in isosteric heat and the adsorbed-phase heat capacities. An analysis of carbon dioxide adsorption on ZTC indicates a high degree of binding-site homogeneity. A generalized Law of Corresponding States analysis indicates lower carbon dioxide adsorption than expected.

1. Introduction

Anthropogenic contributions to carbon dioxide in the atmosphere have become an ever-increasing concern, recently highlighted by the IPCC Fifth Assessment Report¹. Given the growing nature of world energy demands and our continued reliance on fossil fuels, carbon-capture and storage (CCS) should be considered in any plan to mitigate climate change.^{2,3}

Physisorptive materials are promising for a variety of gas applications because they require only low regeneration energies and are stable through thousands of cycles.^{4,5} In physisorption, solid adsorbents induce a local densification of gas at the adsorbent surface by weak physical interactions. Physisorptive materials have been widely used for gas storage applications.^{6,7} Because different gases adsorb to a given surface with differing selectivities, physisorptive materials are also promising for gas separations^{8,9}. A number of studies have shown that physisorptive materials are viable candidates for separating carbon dioxide from mixed-gas streams.^{10,11,12}

An adsorbent's selectivity of one gas over another is dependent on the thermodynamic properties of the gas-adsorbent system. As gas molecules are adsorbed, their molar entropy decreases. This is offset by a decrease in molar enthalpy from favorable interactions between the adsorbate and the adsorbent. The differential change in molar enthalpy at constant surface occupancy, defined as the isosteric enthalpy of adsorption (ΔH_{ads}), is an important and readily accessible figure of merit for physisorptive processes.¹³ Optimizing the isosteric enthalpy of adsorption has been the topic of active research.^{14,15,16} A variety of high surface area materials including metal-organic frameworks, covalent-organic frameworks, zeolites, zeolite-templated

carbons, and activated carbons have been investigated as carbon dioxide adsorbents, and have exhibited isosteric heats of adsorption of up to $90 \text{ kJ}\cdot\text{mol}^{-1}$.^{17,18,19,20,21,22,23}

In general the isosteric heat of adsorption ($-\Delta H_{ads}$) decreases as a function of surface loading due to heterogeneity of the binding sites.²⁴ This has the effect of limiting the pressure range over which gas separation and storage are optimal. However, recent investigations of nonideal gases adsorbed on carbonaceous materials at high pressures have shown that, in some systems, strong lateral intermolecular interactions between adsorbate molecules can lead to an isosteric heat of adsorption that increases with increasing occupancy near ambient temperatures.^{25,26,27,28} This effect is realized in adsorbent materials with optimal surface structure and a narrow distribution of binding-site energies.^{29,30} At high pressures, carbon dioxide gas has strong intermolecular interactions and nonideal behavior, and is therefore a candidate for this effect. In this paper we report that the superactivated carbon MSC-30 has an atypical, increasing isosteric heat of carbon dioxide adsorption, and we provide evidence that this effect derives from adsorbate-adsorbate intermolecular interactions.

2. Experimental Methods

Carbon dioxide uptake was measured on three carbonaceous materials: CNS-201, MSC-30, and ZTC. The activated carbon CNS-201 was obtained from A.C. Carbons Canada Inc., and MSC-30, a superactivated carbon, was obtained from Kansai Coke & Chemicals Company Ltd. ZTC was synthesized by infiltrating zeolite NaY with furfuryl alcohol followed by polymerization, carbonization and the ultimate dissolution of the zeolite template. This synthesis has been described in detail elsewhere³¹. Each material was degassed at 520 K under

vacuum (less than 10^{-3} Pa) prior to measurements. The skeletal densities of the materials were determined by helium pycnometry.

Equilibrium N_2 adsorption isotherms were measured at 77 K with a BELSORP-max volumetric instrument (BEL-Japan Inc.), and surface areas were calculated using the Brunauer-Emmett-Teller (BET) method³². The Dubinin-Radushkevich (DR) method^{33,34} was used to calculate micropore volumes. Pore-size distributions were calculated by the non-local density functional theory (NLDFT) method³⁵ from high-resolution data collected on a Micromeritics ASAP 2020, using a carbon slit-pore model and software provided by Micromeritics.

Equilibrium carbon dioxide adsorption isotherms were measured at up to nine temperatures between 240 and 478 K using a custom Sieverts apparatus that was designed and tested for accuracy to 10 MPa³⁶. The sample holder was submerged in an isothermal chiller bath for low temperature isotherms, or placed inside a cylindrical copper heat exchanger and wrapped with insulated fiberglass heating tape for high temperature isotherms. A proportional-integral-derivative (PID) controller was used to maintain a constant temperature during measurements; fluctuations were less than ± 0.1 K at low temperatures and no higher than ± 0.4 K at high temperatures.

The Sieverts apparatus is equipped with a digital cold cathode pressure sensor (I-MAG, Series 423) and a molecular drag pump capable of achieving a vacuum pressure of 10^{-4} Pa. High-pressure measurements were made using an MKS Baratron (Model 833) pressure transducer. Temperature was measured on the wall of the manifold and on the outer wall of the sample holder using K-type thermocouples and platinum resistance thermometers. Supercritical fluid chromatography (SFC) grade carbon dioxide (99.995%) gas was obtained from Air Liquide America Corporation, and multiple adsorption/desorption isotherms were

measured to ensure reversibility and reproducibility. Gas densities were determined from the REFPROP Standard Reference Database³⁷.

3. Results

3.1. Nitrogen Adsorption and Helium Pycnometry

The pore-size distributions calculated by nonlocal density functional methods of CNS-201, MSC-30, and ZTC are shown in Figure 1. CNS-201 was found to have distinct, extremely narrow pore sizes of < 1.5 nm in width. MSC-30, on the other hand, has a broad pore size distribution with pore widths ranging from 0.6 to >3 nm. ZTC has a single dominant pore width of 1.2 nm, consistent with the inverse of the zeolite structure. The BET surface areas of MSC-30, CNS-201, and ZTC were found to be 3244 ± 28 , 1095 ± 8 , and 3591 ± 60 $\text{m}^2 \cdot \text{g}^{-1}$, respectively. ZTC is one of the highest specific surface area carbonaceous materials reported to date. The micropore volumes of MSC-30, CNS-201, and ZTC were determined to be 1.54, 0.45, and 1.66 $\text{mL} \cdot \text{g}^{-1}$, respectively. The theoretical maximum possible carbon dioxide adsorption (n_m) was estimated as the product of the micropore volume and the density of liquid carbon dioxide at its triple point,³⁰ yielding estimated n_m values of 41.3, 12, and 44.5 $\text{mmol} \cdot \text{g}^{-1}$ for MSC-30, CNS-201, and ZTC, respectively. MSC-30 and CNS-201 have skeletal densities of $2.1 \text{ g} \cdot \text{mL}^{-1}$, while ZTC has a lower skeletal density of $1.8 \text{ g} \cdot \text{mL}^{-1}$ due to a higher hydrogen content³⁸.

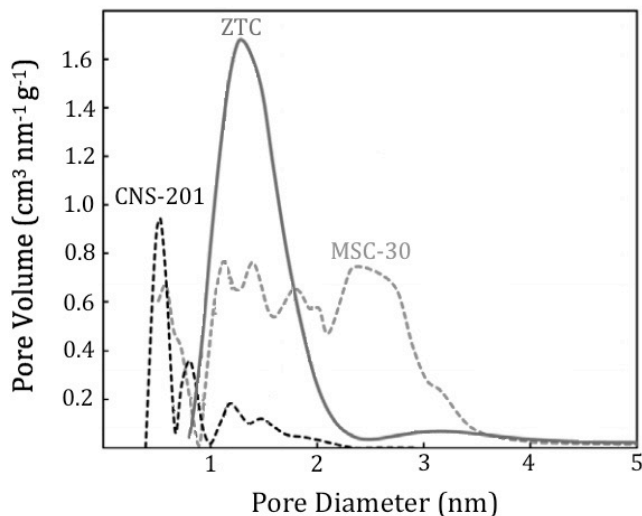


Figure 1. The pore-size distribution of MSC-30, CNS-201, and ZTC as calculated by the NLDFT method.

3.2. Carbon Dioxide Adsorption

Equilibrium excess adsorption isotherms of carbon dioxide on the nanostructured carbons are shown in Figure 2. The low temperature isotherms display maxima at pressures between 0.5-5 MPa, as expected for Gibbs excess quantities. At all measured temperatures, MSC-30 has the highest maximum excess adsorption quantities. At room temperature (298 K), the maximum excess uptakes on MSC-30, CNS-201, and ZTC were 22.7, 7.25, and 17.8 $\text{mmol}\cdot\text{g}^{-1}$ respectively, corresponding to 7.00, 6.62, and 4.96 $\text{mmol}\cdot(1000 \text{ m}^2)^{-1}$. This correlation of BET surface area and Gibbs surface excess uptake maximum capacity is consistent with other similar materials, which have an average “Chahine’s-type rule” for carbon dioxide uptake at 298 K of $\sim 7 \text{ mmol} (1000 \text{ m}^2)^{-1}$.³⁹

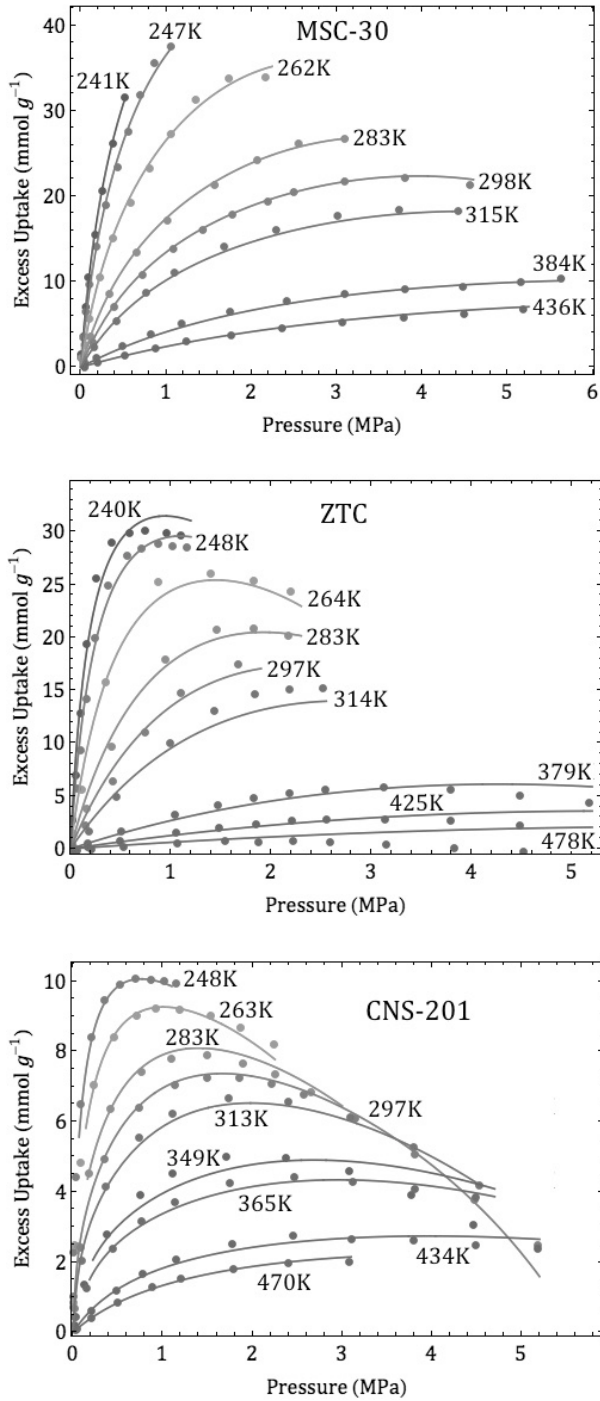


Figure 2. Equilibrium excess adsorption isotherms of carbon dioxide on MSC-30 (top), ZTC (middle), and CNS-201 (bottom). The curves show the best simultaneous fit of the measured data for a given material, using Equation 2 below.

3.3. Adsorption Data Analysis

Adsorption measurements give excess adsorption (n_e), not absolute adsorption (n_a).⁴⁰ At low pressures, excess adsorption approximates absolute adsorption. At high pressures, however, the absolute adsorption remains a monotonically increasing quantity, but excess adsorption does not. By utilizing a fitting equation consistent with the definition of excess adsorption, measured data can be fitted beyond the maximum of excess adsorption. Our carbon dioxide excess adsorption isotherms were fitted using a generalized Langmuir equation, recently described and applied to high-pressure methane adsorption.²⁹ This fitting technique was adapted from that implemented by Mertens⁴¹.

The fitting procedure incorporates the Gibbs definition of excess adsorption, which is related to absolute adsorption as follows:

$$n_e = n_a - V_a \rho(P, T) \quad (1)$$

The gas density (ρ) is a function of pressure (P) and temperature (T) and was estimated from the modified Benedict–Webb–Rubin equation of state³⁷. The volume of the adsorption layer, V_a is the only unknown preventing direct calculation of absolute adsorption. Here V_a is left as an independent fitting parameter. The Gibbs excess adsorption was fitted using the following generalized Langmuir equation:

$$n_e(P, T) = (n_{max} - V_{max} \rho(P, T)) \left[\sum_i \alpha_i \frac{K_i P}{1 + K_i P} \right] \quad (2)$$

$$K_i = \frac{A_i}{\sqrt{T}} e^{-E_i/RT} \quad (3)$$

$$\sum_i \alpha_i = 1 \quad (4)$$

The independent fitting parameters are α_i (weighting factors) and K_i (equilibrium constants) for the i Langmuir isotherms, the scaling factor n_{max} and the maximum volume of the

adsorption layer V_{max} . The equilibrium constants (Equation 3) depend on the prefactors (A_i) and energies (E_i) of the Arrhenius-type exponentials and R , the universal gas constant. For a good balance between number of fitting parameters and goodness of fit, the number of superimposed Langmuir equations used was $i=2$. The residual mean square values of the resulting fits of the adsorption data for MSC-30, CNS-201, and ZTC were 0.1, 0.07, and 0.7 (mmol g^{-1})² respectively.

The best-fit parameters of carbon dioxide on MSC-30, CNS-201, and ZTC are compared to the best-fit parameters of methane²⁵, ethane²⁶, and krypton²⁷ on the same materials (using the same fitting equation) in Table 1. In many cases, the fit parameters correlate to physical properties, and may sometimes be validated by comparison to independent estimates. For example, the adsorbent micropore volume can be determined by the Dubinin-Radushkevich method³³ and compared to V_{max} . Likewise the product of the adsorbent micropore volume and the liquid molar density of the adsorbate³⁷ (n_m) provides an estimate of n_{max} . Rigorous comparisons of the fitted and independently estimated parameters are shown in Table 2.

Table 1. Best-fit parameters from Generalized Langmuir Fits.

| | n_{max} (mmol g^{-1}) | α | V_{max} (mL g^{-1}) | A_1 ($\text{k}^{1/2} \text{MPa}^{-1}$) | E_1 (kJ mol^{-1}) | A_2 ($\text{k}^{1/2} \text{MPa}^{-1}$) | E_2 (kJ mol^{-1}) |
|---------------------------------------|---------------------------------------|----------|-------------------------------------|---|-----------------------------------|---|-----------------------------------|
| CO ₂ /ZTC | 45.4 | 1.64E-12 | 12.4 | 0.00143 | 21.6 | 0.121 | 3.94 |
| CO ₂ /CNS-201 | 12.9 | 0.800 | 3.41 | 0.0456 | 23.0 | 0.00244 | 22.0 |
| CO ₂ /MSC-30 | 81.1 | 0.207 | 10.0 | 0.000107 | 23.6 | 0.0635 | 14.3 |
| CH ₄ /ZTC | 35.6 | 0.460 | 2.04 | 0.0590 | 11.6 | 0.000180 | 20.4 |
| CH ₄ /CNS-201 | 9.77 | 0.580 | 0.490 | 0.0610 | 17.2 | 0.00440 | 16.4 |
| CH ₄ /MSC-30 | 41.0 | 0.700 | 2.30 | 0.0680 | 13.4 | 0.00460 | 12.9 |
| C ₂ H ₆ /ZTC | 25.0 | 0.827 | 1.58 | 2.14E-07 | 41.0 | 0.0444 | 18.5 |
| C ₂ H ₆ /MSC-30 | 36.1 | 0.713 | 2.60 | 0.0865 | 19.8 | 0.00647 | 17.8 |
| Kr/ZTC | 39.3 | 0.686 | 2.02 | 1.81E-06 | 30 | 0.0924 | 10.0 |
| Kr/CNS-201 | 10.9 | 0.462 | 0.490 | 0.00590 | 15.1 | 0.0689 | 16.3 |
| Kr/MSC-30 | 57.8 | 0.726 | 2.98 | 0.112 | 11.6 | 0.00306 | 12.8 |

Table 2. Comparison of V_{max} and n_{max} Parameters to Independent Estimates

| | V_{max} (mL g ⁻¹) | micropore volume (mL g ⁻¹) | n_{max} (mmol g ⁻¹) | n_m (mmol g ⁻¹) |
|---------------------------------------|---------------------------------|--|-----------------------------------|-------------------------------|
| CO ₂ /ZTC | 12.4 | 1.66 | 45.4 | 44.5 |
| CO ₂ /CNS-201 | 3.41 | 0.45 | 12.9 | 12 |
| CO ₂ /MSC-30 | 10.0 | 1.54 | 81.1 | 41.3 |
| CH ₄ /ZTC | 2.04 | 1.66 | 35.6 | 46.6 |
| CH ₄ /CNS-201 | 0.490 | 0.45 | 9.77 | 13 |
| CH ₄ /MSC-30 | 2.30 | 1.54 | 41.0 | 43.3 |
| C ₂ H ₆ /ZTC | 1.58 | 1.66 | 25.0 | 36.0 |
| C ₂ H ₆ /MSC-30 | 2.60 | 1.54 | 36.1 | 33.4 |
| Kr/ZTC | 2.02 | 1.66 | 39.3 | 48.5 |
| Kr/CNS-201 | 0.490 | 0.45 | 10.9 | 13 |
| Kr/MSC-30 | 2.98 | 1.54 | 57.8 | 45.0 |

Although more difficult to validate through independent comparison, the E_i parameters give important insight into the adsorbent-adsorbate binding energies of the i^{th} isotherm, and the prefactor A_i gives insight about the relative number of adsorption sites with energy E_i . Specifically, the product of α_p , the i^{th} isotherm weighting factor, and A_i gives an overall “weight” of sites with energy E_i . For carbon dioxide, methane, ethane and krypton adsorption on MSC-30 and CNS-201, the contributions of each isotherm in the fitted superposition of isotherms are moderately well-balanced. No isotherm accounts for less than 1% of the overall “weight”, except for carbon dioxide on MSC-30. This may result from carbon dioxide adsorbing on a more limited set of MSC-30 adsorption sites than other gases, as noted on single-wall carbon nanotube bundles⁴².

For ZTC, each generalized Langmuir fit heavily favors just a single isotherm (see Table 3). This suggests that ZTC usually has a higher degree of binding-site homogeneity than MSC-30 or CNS-201, consistent with the pore-size distributions of the three carbonaceous adsorbents. Unlike MSC-30 and CNS-201, ZTC has a single sharply peaked pore width (1.2

nm). In microporous carbons, the predominant contribution to binding-site heterogeneity often results from the spectrum of pore widths. ZTC eliminates much of this heterogeneity with its micropores of approximately a constant width.

Table 3. Normalized Relative Weights of Isotherms 1 and 2 as Determined by Multiplying the Isotherm Weighting Value (α_i) by the Isotherm Prefactor (A_i)

| | Isotherm 1 Weight | Isotherm 2 Weight |
|---------------------------------------|-------------------|-------------------|
| CO ₂ /ZTC | 1.94E-14 | 1.00E+00 |
| CO ₂ /CNS-201 | 9.87E-01 | 1.32E-02 |
| CO ₂ /MSC-30 | 4.40E-04 | 1.00E+00 |
| CH ₄ /ZTC | 9.96E-01 | 3.57E-03 |
| CH ₄ /CNS-201 | 9.50E-01 | 4.96E-02 |
| CH ₄ /MSC-30 | 9.72E-01 | 2.82E-02 |
| C ₂ H ₆ /ZTC | 2.30E-05 | 1.00E+00 |
| C ₂ H ₆ /MSC-30 | 9.71E-01 | 2.92E-02 |
| Kr/ZTC | 4.28E-05 | 1.00E+00 |
| Kr/CNS-201 | 6.85E-02 | 9.32E-01 |
| Kr/MSC-30 | 9.90E-01 | 1.02E-02 |

The Clapeyron relation was used to determine the isosteric heat of adsorption:

$$q_{st} = -\Delta H_{ads}(n_a) = -T \left(\frac{\partial P}{\partial T} \right)_{n_a} (\Delta v_{ads}) \quad (5)$$

Here the isosteric heat of adsorption (q_{st}) is (by convention) a positive value when adsorption is exothermic. The coverage-dependent change in enthalpy upon adsorption is $\Delta H_{ads}(n_a)$. The change in molar volume of the adsorbate upon adsorption is Δv_{ads} .

4. Discussion

4.1. Isotheric Heat of Carbon Dioxide Adsorption

The isotheric heats of carbon dioxide adsorption on MSC-30, CNS-201, and ZTC derived according to Equation 5 are shown in Figure 3. The isotheric heat of carbon dioxide adsorption on MSC-30 differs significantly from that on a conventional activated carbon like CNS-201 in its dependence on absolute uptake. For carbon dioxide adsorption on CNS-201, the isotheric heat displays typical behavior. It is a decreasing function of occupancy. On the other hand, the isotheric heat of carbon dioxide adsorption on MSC-30 first increases as a function of occupancy before reaching a maximum, and then decreases at high occupancy. On ZTC, the isotheric heat of carbon dioxide adsorption decreases very gradually with loading, especially at low temperatures where the slope is $\sim -25\text{kJ}\cdot\text{mol}^{-2}$. This behavior is in agreement with the high degree of binding-site homogeneity expected from the pore-size distribution and fit parameters for ZTC. Carbon dioxide adsorption differs from methane, ethane, and krypton adsorption where the isotheric heats on MSC-30 decrease with occupancy, while the isotheric heats on ZTC increase with occupancy due to enhanced adsorbate-adsorbate interactions. This suggests that carbon dioxide adsorbate-adsorbate interactions are better optimized for the micropore distribution of MSC-30 than ZTC.

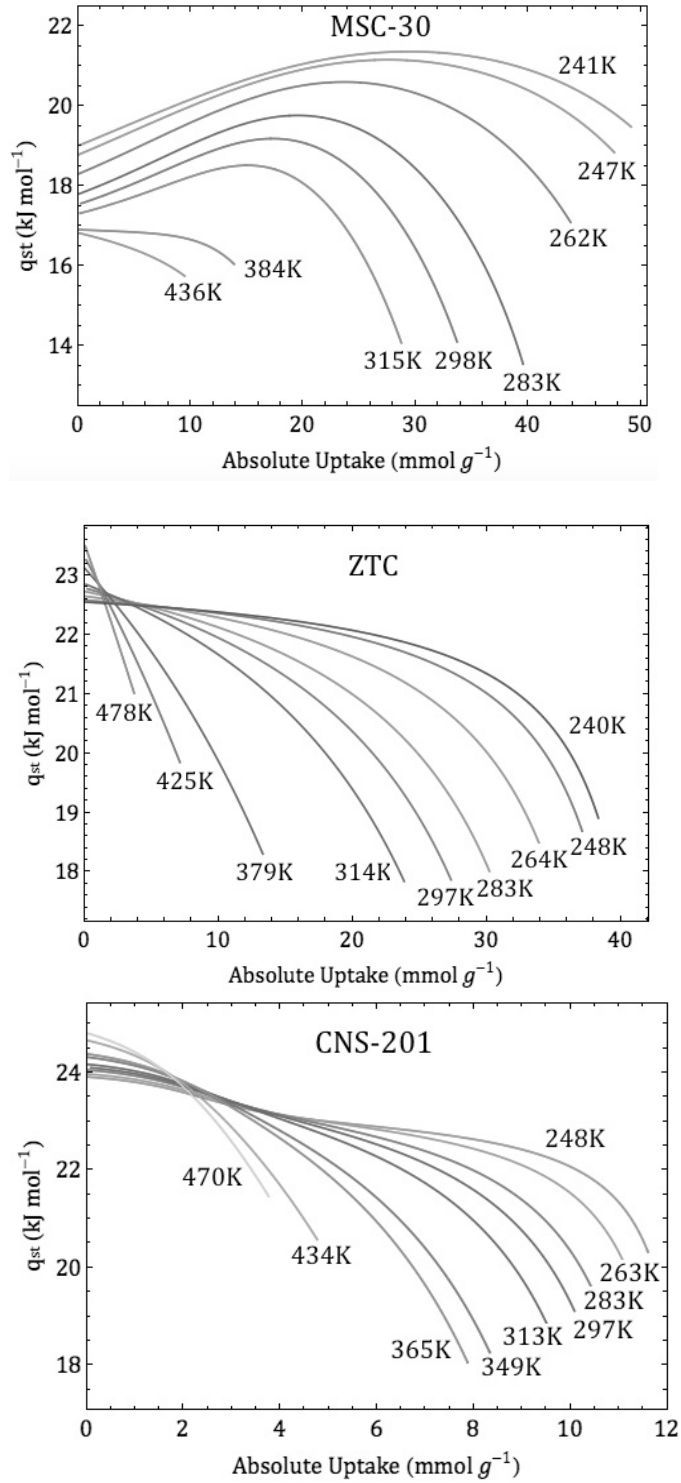


Figure 3. Isosteric heats of adsorption of carbon dioxide on CNS-201, MSC-30, and ZTC as a function of absolute uptake.

For carbon dioxide adsorbed on MSC-30, the total increase in isosteric heat (peak value minus low coverage value) is more pronounced at lower temperatures, reaching a maximum measured increase of $2.1 \text{ kJ}\cdot\text{mol}^{-1}$ at 241 K. This energy is consistent with lateral intermolecular interactions between adsorbed carbon dioxide molecules. For example, the well depth of the Lennard-Jones potential between two carbon dioxide molecules is $\varepsilon = 1.8 \text{ kJ}\cdot\text{mol}^{-1}$ ⁴³.

At low temperatures and low occupancy, the isosteric heat of adsorption of carbon dioxide on MSC-30 increases approximately linearly with occupancy. This linear increase is nearly identical for the lowest temperatures measured (e.g. $107 \text{ kJ}\cdot\text{g}\cdot\text{mol}^{-2}$ at 241 K, $111 \text{ kJ}\cdot\text{g}\cdot\text{mol}^{-2}$ at 247 K, $113 \text{ kJ}\cdot\text{g}\cdot\text{mol}^{-2}$ at 262 K and $106 \text{ kJ}\cdot\text{g}\cdot\text{mol}^{-2}$ at 283 K). Similar trends hold true for methane, ethane, and krypton adsorption on ZTC.^{25,26,27} The gases with stronger intermolecular interactions have larger slopes, consistent with the hypothesis that the increases in the isosteric heats with loading result from adsorbate-adsorbate intermolecular interactions.

The slopes of the isosteric heats with respect to fractional occupancy, $\frac{\partial(-\Delta H_{ads})}{\partial\theta}$, may be reasonably estimated with Equation 6 (see Table 4) in the low coverage regime

$$\frac{\partial(-\Delta H_{ads})}{\partial\theta} = \frac{z\varepsilon}{2} \quad (6)$$

where the coordination number, z , is posited to be 5 and ε is the well depth of the Lennard-Jones 12-6 interaction potential⁴³. This simple first approximation (Equation 6) assumes that adsorbed molecules are randomly situated and only interact with first nearest neighbors, each interaction having strength ε .

Table 4. Measured and Estimated Slopes of Increasing Isothermic Heats of Methane, Ethane, and Krypton on ZTC, and Carbon Dioxide on MSC-30 as a Function of Fractional Occupancy (at Low Coverage and Low Temperature)

| | Estimated Slope (kJ•mol ⁻¹) | Measured Slope (kJ•mol ⁻¹) |
|----------------|---|--|
| Methane | 3.0 | 3.2 |
| Krypton | 3.3 | 3.4 |
| Ethane | 4.3 | 4.0 |
| Carbon Dioxide | 4.5 | 4.5 |

A qualitatively similar increase in the isothermic heat of carbon dioxide adsorption on Maxsorb® (from Kansai Netsu Kagaku Co.) was previously noted by Himeno et al.⁴⁴, however it is unclear to what degree those results are quantitatively accurate. Himeno et al. used the Toth equation to fit three experimental isotherms (at 273, 298, and 323K). This fit was then used to calculate an isothermic heat via a reduced form of the Clausius-Clapeyron Equation (Equation 7).

$$\frac{\Delta H}{RT^2} = \left[\frac{\partial \ln P}{\partial T} \right]_N \quad (7)$$

The calculated “isothermic heat” (ΔH) was determined from the partial derivative of the logarithm of the pressure with respect to temperature at constant coverage (N). In this case, however, excess adsorption, not absolute adsorption was held constant and what was calculated may more aptly be called an “isoexcess heat of adsorption”. At low coverage, excess adsorption accurately approximates absolute adsorption, but deviations arise and become significant as the equilibrium gas-phase density increases. In our work we employ a generalized Langmuir-type fitting function that determines absolute adsorption and gives true “isothermic

heats of adsorption". We have elaborated on this methodology in prior publications^{25,26,27,29}.

Additionally, Equation 7, which is employed by Himeno et al. but not in our work, makes two idealized assumptions that break down for nonideal gas conditions. Equation 7 assumes that the volume of the adsorbed phase is zero, and further assumes the validity of the ideal gas law. These assumptions lead to significant errors under nonideal gas conditions. Furthermore, our analysis determines the temperature dependence of the isosteric heat, which is ignored by Himeno et al. Himeno et al. report an increasing isosteric heat for carbon dioxide adsorption on Maxsorb[®] with a slope of ~ 300 ($\text{kJ}\cdot\text{g}\cdot\text{mol}^{-2}$). We report a more moderate slope (~ 110 $\text{kJ}\cdot\text{g}\cdot\text{mol}^{-2}$) on the comparable superactivated carbon MSC-30 after considering isotherms taken at eight temperatures. This more moderate increase is more consistent with the strength of carbon dioxide intermolecular interactions as measured by the Lennard-Jones parameter, $\epsilon=1.8$ $\text{kJ}/\text{mol}^{43}$, Equation 6 and the trend in Table 3.

4.2 Adsorbed-Phase Enthalpies and Heat Capacities

The adsorbed-phase enthalpies for carbon dioxide adsorption on MSC-30, CNS-201, and ZTC were calculated as a function of absolute adsorption by subtracting the isosteric heats in Figure 3 from gas-phase enthalpy values determined from data tables at equivalent conditions³⁷. Figure 4 shows that MSC-30 has different behavior than CNS-201 or ZTC in that the adsorbed-phase enthalpy is not a monotonically increasing function of coverage. Rather the adsorbed-phase enthalpy on MSC-30 decreases with coverage at low temperatures and low coverages, consistent with enhanced favorable adsorbate-adsorbate interactions.

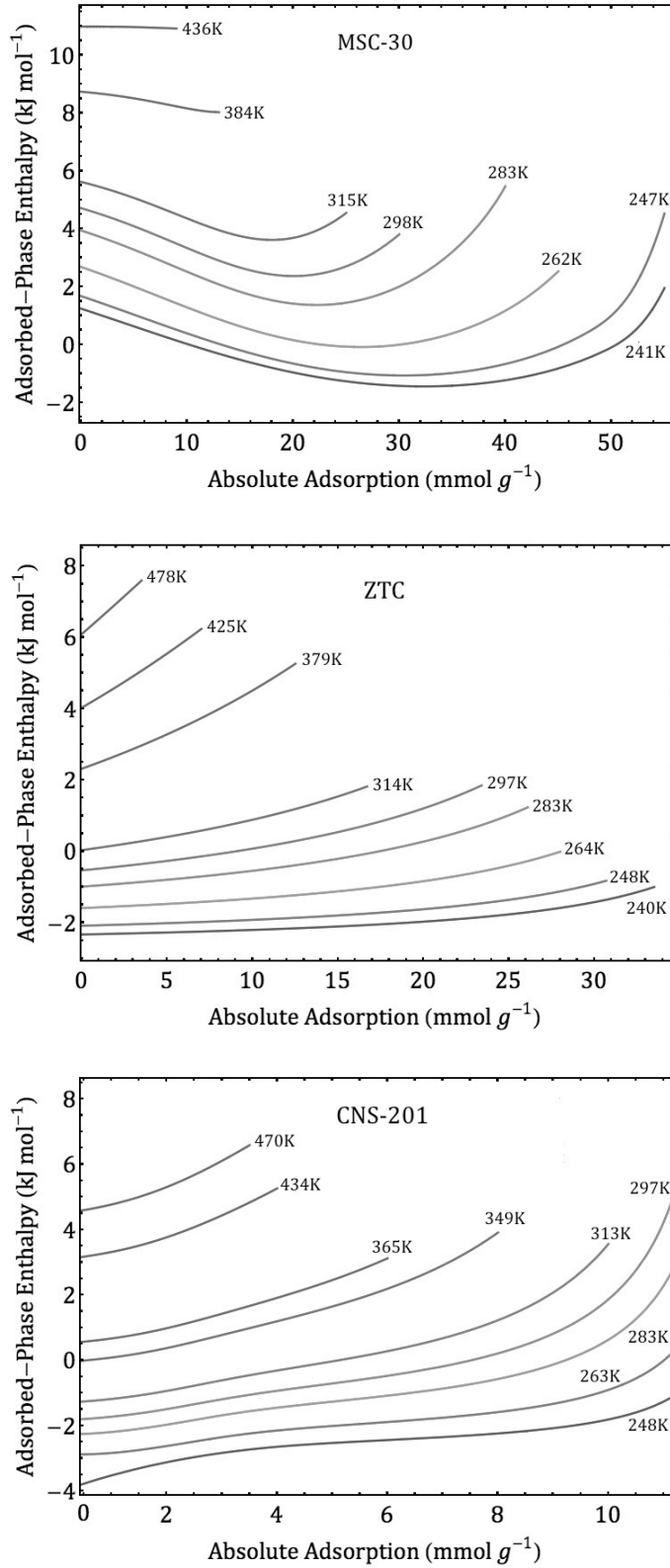


Figure 4. Adsorbed-phase enthalpies of carbon dioxide on MSC-30, ZTC, and CNS-201.

The adsorbed-phase constant pressure heat capacities of carbon dioxide on MSC-30, CNS-201, and ZTC were calculated by taking the partial derivative of the adsorbed-phase enthalpies with respect to temperature at constant pressure. Figure 5 shows the adsorbed-phase heat capacities at a constant sample pressure of 2 MPa.

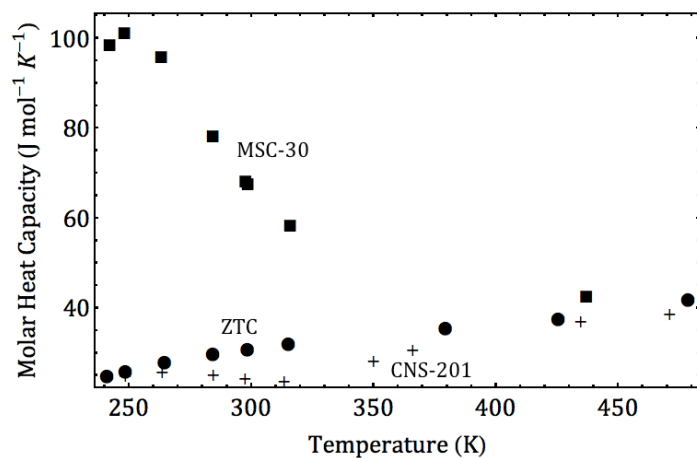


Figure 5. Adsorbed-phase molar heat capacities of carbon dioxide on MSC-30 (■), CNS-201 (+), and ZTC (●). Values are given at a constant sample pressure of 2 MPa.

Figure 5 shows that the constant pressure adsorbed-phase heat capacities of carbon dioxide on CNS-201 and ZTC gradually increase with temperature as expected for a polyatomic gas. On MSC-30 a different behavior is observed where the adsorbed-phase heat capacity rises significantly around a temperature of 250K. This is suggestive of a phase transition and indicates that the origin of the enhanced adsorbate-adsorbate interactions may be an adsorbed-phase clustering transition as previously noted in other systems.^{29,30}

4.3 Law of Corresponding States and Selectivities

It is well established that different nonideal gases behave similarly at corresponding conditions, at equal reduced temperatures and reduced pressures.⁴⁵ The reduced temperature and reduced pressure are defined as the ratios of the system temperature to the gas critical temperature, and the system pressure to the gas critical pressure, respectively. We have recently reported an extension to the Law of Corresponding States that applies to physisorbed molecules.³⁰ Specifically:

Classical gases adsorb to the same fractional occupancy on the same adsorbent at corresponding conditions.

Fractional occupancy (θ) is defined as the ratio of the absolute adsorption (n_a) to maximum possible adsorption (n_m). To facilitate comparisons in this work and others,³⁰ we instead compare the more accessible quantity, excess occupancy (θ_e), defined as the ratio of excess adsorption (n_e) to maximum possible adsorption (n_m). For each adsorbent, n_m was estimated by multiplying the adsorbent micropore volume by the liquid molar density of the adsorbate at its triple point.^{30,37} Carbon dioxide, ethane, methane, and krypton excess occupancy isotherms on ZTC and MSC-30 are compared at corresponding conditions in Figure 6.

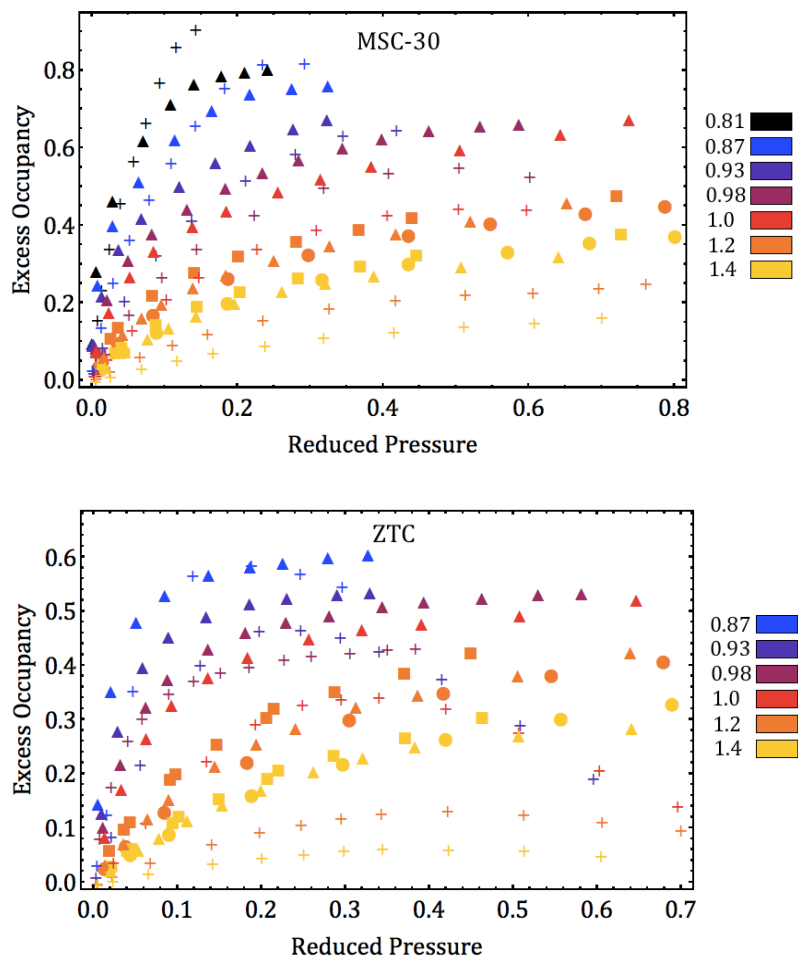


Figure 6. Comparison of carbon dioxide (+), ethane (Δ), methane (\blacksquare), and krypton (\bullet) excess occupancies at corresponding conditions (with reduced temperatures given in the key).

At low temperatures, there is reasonable agreement between carbon dioxide and ethane isotherms at corresponding conditions. At higher temperatures, however, the carbon dioxide isotherms are significantly smaller than corresponding isotherms of the other gases. This may be due in part to the large quadrupole moment of carbon dioxide⁴⁶, which is not present in the other gases considered. The large quadrupole moment accounts for $\sim 50\%$ of the cohesive energy of solid carbon dioxide.^{47,48} Notably the bulk critical temperature and isosteric heats of carbon dioxide and ethane are similar in spite of carbon dioxide's significantly

lower polarizability. This is also consistent with a strong quadrupole interaction of carbon dioxide.^{49,50,51} It is possible that the short-range quadrupole-induced dipole interactions between carbon dioxide and the adsorbent are disrupted with temperature, but further investigation is needed.

The selectivities of carbon dioxide with respect to methane, ethane and krypton were calculated as the ratio of the Henry's Law constants. Henry's Law constants were calculated directly from the excess adsorption data by extrapolating to zero coverage the logarithm of pressure divided by excess adsorption ($\ln(P/n)$).⁵² The measured room temperature Henry's Law constants and selectivities are given in Table 5. Methane and krypton have similar Henry's Law constants, as one might expect based on the similarity of the gases, particularly their similar critical temperatures. While carbon dioxide and ethane have nearly identical critical temperatures, ethane has significantly higher room temperature Henry's Law constants for each adsorbent. This is consistent with the trends noted in Figure 6.

Table 5. Henry's Law Constants ($\text{mmol g}^{-1} \text{MPa}^{-1}$) and Equilibrium Adsorption Selectivities at Room Temperature

| Henry's Law Constants | ZTC | MSC-30 | CNS-201 |
|--|------|--------|---------|
| C ₂ H ₆ | 45.7 | 51.9 | 35.1 |
| CO ₂ | 19.7 | 19.9 | 21.4 |
| CH ₄ | 7.03 | 8.99 | 6.99 |
| Kr | 6.80 | 9.03 | 6.57 |
| CO ₂ /CH ₄ | 2.80 | 2.21 | 3.06 |
| C ₂ H ₆ /CO ₂ | 2.32 | 2.61 | 1.64 |
| CO ₂ /Kr | 2.90 | 2.20 | 3.26 |
| C ₂ H ₆ /CH ₄ | 6.50 | 5.77 | 5.02 |
| C ₂ H ₆ /Kr | 6.72 | 5.75 | 5.34 |

5. Conclusions

The excess uptakes of carbon dioxide on MSC-30, CNS-201, and ZTC were measured volumetrically and fitted with a generalized Langmuir-type equation. The fitted data were used in thermodynamic analyses that show how MSC-30 exhibits an atypical, increasing isosteric heat of carbon dioxide adsorption, while CNS-201 has the thermodynamic properties of a conventional carbon. The isosteric heat on ZTC suggests a high degree of binding-site homogeneity. At near-ambient temperatures the isosteric heat on MSC-30 rises with uptake from 19 to 21 $\text{kJ}\cdot\text{mol}^{-1}$. The measured adsorbed-phase enthalpies, adsorbed-phase heat capacities, and comparisons to studies with other nonideal gases indicate that this increasing isosteric heat results from enhanced adsorbate-adsorbate interactions within the pores of MSC-30.

Acknowledgements

This work was supported as part of EFree, an Energy Frontier Research Center under Award No. DE-SC0001057. A special thanks to Christopher Gardner for his contributions in the lab.

References:

1. Climate change 2013: The physical science basis. Intergovernmental Panel on Climate Change, Ed. Cambridge: Cambridge University Press, 2014.
2. Haszeldine RS. Carbon capture and storage: How green can black be? *Science* 2009; 325: 1647-1652.
3. Boot-Handford ME, Abanades JC, Anthony EJ, et al. Carbon capture and storage update. *Energy Environ Sci.* 2014; 7: 130-189.
4. Ruthven DM. Principles of Adsorption and Adsorption Processes. New York: Wiley, 1984.
5. Sircar S. Basic research needs for design of adsorptive gas separation processes. *Ind Eng Chem Res.* 2006; 45: 5435-5448.
6. Tedds S, Walton A, Broom DP, Book D. Characterization of porous hydrogen storage materials: Carbons, zeolites, MOFs and PIMs. *Faraday Discuss.* 2011; 151: 75-94.
7. Matranga KR, Myers AL, Glandt ED. Storage of natural-gas by adsorption on activated carbon. *Chem Eng Sci.* 1992; 47: 1569-1579.
8. Jasra RV, Choudary NV, Bhat SGT. Separation of gases by pressure swing adsorption. *Separ Sci and Technol.* 1991; 26: 885-930.
9. Sircar S, Golden TC, Rao MB. Activated carbon for gas separation and storage. *Carbon.* 1996; 34: 1-12.
10. Choi S, Drese JH, Jones CW. Adsorbent materials for carbon dioxide capture from large anthropogenic point sources. *Chem Sus Chem.* 2009; 2: 796-854.
11. D'Alessandro DM, Smit B, Long JR. Carbon dioxide capture: Prospects for new materials. *Angew Chem Int Ed.* 2010; 49: 6058-6082.
12. Chen ZH, Deng SB, Wei HR, Wang B, Huang J, Yu G. Activated carbons and amine-modified materials for carbon dioxide capture – A review. *Front Environ Sci Eng.* 2013; 7: 326-340.
13. Sircar S, Mohr R, Ristic C, Rao MB. Isothermic heat of adsorption: Theory and experiment. *J Phys Chem B.* 1999; 103: 6539-6546.
14. Bhatia SK, Myers AL. Optimum conditions for adsorptive storage. *Langmuir.* 2006; 22: 1688-1700.
15. Simon CM, Kim J, Lin LC, Martin RL, Haranczyk M, Smit B. Optimizing nanoporous materials for gas storage. *Phys Chem Chem Phys.* 2014; 16: 5499-5513.
16. Lee SY, Park SJ. Determination of the optimal pore size for improved CO₂ adsorption in activated carbon fibers. *J Colloid Interface Sci.* 2013; 389: 230-235.
17. Gargiulo N, Pepe F, Caputo D. CO₂ adsorption by functionalized nanoporous materials: A review. *J Nanosci Nanotechnol.* 2014; 14: 1811-1822.
18. Bae YS, Snurr RQ. Development and evaluation of porous materials for carbon dioxide separation and capture. *Angew Chem Int Ed.* 2011; 50: 11586-11596.
19. Furukawa H, Yaghi OM. Storage of hydrogen, methane, and carbon dioxide in highly porous covalent organic frameworks for clean energy applications. *J Am Chem Soc.* 2009; 131: 8875- 8883.

20. Wang QA, Luo JZ, Zhong ZY, Borgna A. CO₂ capture by solid adsorbents and their applications: current status and new trends. *Energy Environ Sci.* 2011; 4: 42-45.
21. Wang B, Cote AP, Furukawa H, O’Keeffe M, Yaghi OM. Colossal cages in zeolitic imidazolate frameworks as selective carbon dioxide reservoirs. *Nature.* 2008; 453: 207-211.
22. Simmons JM, Wu H, Zhou W, Yildirim T. Carbon capture in metal-organic frameworks – A comparative study. *Energy Environ Sci.* 2011; 4: 2177-2185.
23. Zhou J, Li W, Zhang ZS, Xing W, Zhuo SP. Carbon dioxide adsorption performance of N-doped zeolite Y templated carbons. *RSC Adv.* 2012; 2: 161-167.
24. Al-Muhtaseb SA, Ritter JA. Roles of surface heterogeneity and lateral interactions on the isosteric heat of adsorption and adsorbed phase heat capacity. *J Phys Chem B.* 1999; 103: 2467-2479.
25. Stadie NP, Murialdo M, Ahn CC, Fultz B. Anomalous isosteric enthalpy of adsorption of methane on zeolite-templated carbon. *J Am Chem Soc.* 2013; 135: 990-993.
26. Murialdo M, Stadie NP, Ahn CC, Fultz B. Observation and investigation of increasing isosteric heat of adsorption of ethane on zeolite-templated carbon. *J Phys Chem C.* 2015; 119: 944-950.
27. Murialdo M, Stadie NP, Ahn CC, Fultz B. Krypton adsorption on zeolite-templated carbon and anomalous surface thermodynamics. *Langmuir.* 2015; 31: 7991-7998.
28. Mu B, Walton KS. High-pressure adsorption equilibrium of CO₂, CH₄, and CO on an impregnated activated carbon. *J Chem Eng Data.* 2011; 56: 390-397.
29. Stadie NP, Murialdo M, Ahn CC, Fultz B. Unusual entropy of adsorbed methane on zeolite-templated carbon. *J Phys Chem C.* 2015; 119: 26409-26421.
30. Murialdo M, Stadie NP, Ahn CC, Fultz B. A generalized law of corresponding states for the physisorption of classical gases with cooperative adsorbate-adsorbate interactions. *J Phys Chem C.* 2016; 120: 11847-11853.
31. Nishihara H, Hou PX, Li LX, et al. High-pressure hydrogen storage in zeolite-templated carbon. *J Phys Chem C.* 2009; 113: 3189-3196.
32. Brunauer S, Emmett PH, Teller E. Adsorption of gases in multimolecular layers. *J Am Chem Soc.* 1938; 60: 309-319.
33. Nguyen C, Do DD. The Dubinin-Radushkevich equation and the underlying microscopic adsorption description. *Carbon.* 2001; 39: 1327-1336.
34. Rouquerol J, Rouquerol F, Llewellyn P, Maurin G, King KSW. Adsorption by powders and porous solids: Principles, methodology and applications. 2nd ed. Oxford: Academic Press, 2014.
35. Tarazona P, Marconi UMB, Evans R. Phase-equilibria of fluid interfaces and confined fluids-nonlocal versus local density functionals. *Mol Phys.* 1987; 60: 573-595.
36. Bowman RC, Luo CH, Ahn CC, Witham CK, Fultz B. The effect of tin on the degradation of LaNi₅-ySny metal-hydrides during thermal cycling. *J Alloys Compd.* 1995; 217: 185-192.

37. Lemmon, E. W.; Huber, M. L.; McLinden, M. O. NIST Standard Reference Database 23: Reference Fluid Thermodynamic and Transport Properties, version 8.0; National Institute of Standards and Technology: Gaithersburg, MD, 2007; CD-ROM.
38. Stadie NP, Vajo JJ, Cumberland RW, Wilson AA, Ahn CC, Fultz B. Zeolite-templated carbon materials for high-pressure hydrogen storage. *Langmuir*. 2012; 28: 10057-10063.
39. Youn HK, Kim J, Chandrasekar G, Jin H, Ahn WS. High pressure carbon dioxide adsorption on nanoporous carbons prepared by zeolite Y templating. *Mater Lett*. 2011; 65: 1772-1774.
40. Sircar S. Gibbsian surface excess for gas adsorption-Revisited. *Ind Eng Chem Res*. 1999; 38: 3670-3682.
41. Mertens FO. Determination of absolute adsorption in highly ordered porous media. *Surf Sci*. 2009; 603: 1979-1984.
42. Bienfait M, Zeppenfeld P, Dupont-Pavlovsky N, et al. Thermodynamics and structure of hydrogen, methane, argon, oxygen, and carbon dioxide adsorbed on single-wall carbon nanotube bundles. *Phys Rev B*. 2004; 70: 035410(1-10).
43. Tee LS, Gotoh S, Stewart WE. Molecular parameters for normal fluids - Lennard-Jones 12-6 potential. *Ind Eng Chem Fundam*. 1966; 5: 356-363.
44. Himeno S, Komatsu T, Fujita S. High-pressure adsorption equilibria of methane and carbon dioxide on several activated carbons. *J Chem Eng Data*. 2005; 50: 369-376.
45. Guggenheim EA. The principle of corresponding states. *J Chem Phys*. 1945; 13: 253-261.
46. Graham C, Pierrus J, Raab RE. Measurement of the electric quadrupole-moments of CO₂, CO and N₂. *Mol Phys*. 1989; 67: 939-955.
47. Slusarev VA, Freiman YA, Krupskii IN, Burakhov IA. Orientational Disordering and Thermodynamic Properties of Simple Molecular-Crystals. *Phys Status Solidi B*. 1972; 54: 745-754.
48. Hirshfeld FL, Mirsky K. Electrostatic term in lattice-energy calculations - C₂H₂, CO₂, AND C₂N₂. *Acta Crystallogr Sect A*. 1979; 35: 366-370.
49. Buckingham AD, Disch RL. Quadrupole moment of carbon dioxide molecule. *Proc R Soc A*. 1963; 273: 275-289.
50. Do DD, Do HD. Effects of potential models on the adsorption of carbon dioxide on graphitized thermal carbon black: GCMC computer simulations. *Colloids Surf A*. 2006; 277: 239-248.
51. Terlain A, Larher Y. Phase-diagrams of films of linear-molecules with large quadrupole-moments (CO₂, N₂O, C₂N₂) adsorbed on graphite. *Surf Sci*. 1983; 125: 304-311.
52. Zhang SY, Talu O, Hayhurst DT. High-pressure adsorption of methane in NaX, MgX, CaX, SrX, and BaX. *J Phys Chem*. 1991; 95: 1722-1726.

Conclusions

This work has focused on fundamental aspects of gas adsorption, in particular how adsorbent nanostructured architecture affects adsorption thermodynamics. By studying a wide variety of adsorptive species (methane, ethane, krypton, carbon dioxide, etc.) we have noted similarities and differences in adsorptive features arising from differences in adsorbate size, shape, polarizability, etc. Moreover the storage and/or separation of these various gases from mixed gas streams are of critical interest to a variety of energy sectors (including transportation and nuclear). An improved understanding of these adsorptive species under various adsorption conditions, and any anomalies that arise in the nonideal regime have proven and could further prove valuable to addressing energy concerns.

Of note, we discovered anomalous thermodynamics in the adsorbed phase on zeolite-templated carbon (ZTC). At sub ambient temperatures, methane, krypton, and ethane undergo cooperative intermolecular interactions on the surface of zeolite-templated carbon. These lateral interactions between adsorbed molecules affect the adsorbed-phase enthalpy, entropy, and heat capacities, in largely beneficial ways. This is unprecedented for supercritical gases adsorbed on carbonaceous materials. The resulting increase in the isosteric heat of adsorption improves gas storage by increasing the pressure range over which gas storage and delivery is effective. These effects owe to the gas nonideality, which allows for favorable adsorbate-adsorbate interactions that are enhanced on the surface of ZTC, evidently due to its unique surface homogeneity and appropriate pore-size confinement. These cooperative interactions of the adsorbed species are highly temperature dependent and may be modeled with an Ising-type model as a first approximation. Moreover, the prospect of tuning the nanostructure of future

adsorbents to enhance the adsorption of other gases holds promise as an area of future inquiry.

Neither hydrogen nor carbon dioxide registered anomalous cooperative adsorbate-adsorbate interactions on ZTC. Hydrogen has a much smaller polarizability than methane, ethane and krypton, and likewise much weaker van der Waals interactions. This likely precludes hydrogen from exhibiting strong effects of adsorbate-adsorbate interactions under most circumstances. Carbon dioxide is distinct from the other gases studied due to its large quadrupole moment. This short-range interaction may disrupt the optimized adsorption that gases like methane and krypton experience on ZTC, though further investigation is needed. Carbon dioxide did exhibit similar (subcritical) cooperative adsorbate-adsorbate interactions on MSC-30, suggesting that carbon dioxide adsorption is better optimized in larger pores.

Furthermore, we have developed a generalized Law of Corresponding States for gas physisorption to highlight the similarities of distinct nonideal gases under specific adsorption conditions and as a means of unifying various aspects of adsorption theory. We assert and demonstrate that “distinct classical gases adsorb to the same fractional occupancy on the same adsorbent at corresponding conditions.” This generalization accounts for the distinct excluded volume of a particular molecule as well as its nonideal van der Waals interactions. First we explore the validity of this statement with our own data and with literature data. Next we show how it may be derived from multiple theories of adsorption under appropriate approximations. We develop our theoretical basis from three distinct theories, including two that are largely at odds with one another, the theory of layer-by-layer adsorption and the theory of micropore filling. Moreover, by developing a model for the anomalous thermodynamics discovered on ZTC we show that even these cooperative adsorbate-adsorbate interactions may be reasonably subsumed in the generalized Law of Corresponding States for physisorption.

Future Work

Mixed Gases

Currently we have only investigated single gas isotherms. From these we can attempt to estimate mixed-gas quantities of interest such as adsorbent selectivities. There are, however, a number of valid reasons to investigate gas mixtures as a future project. Gases of differing size, shape, intermolecular interactions, etc. may behave unexpectedly when adsorbed together in micropores that are of dimensions similar to that of the adsorptive species. Larger molecules may be sieved by the adsorbent nanostructure or lead to pore blocking. Confinement of mixed gases may lead to unexpected diffusivities or thermodynamics within the pores. In particular, it is unclear how having more than one adsorptive species would affect the anomalous cooperative adsorbate-adsorbate interactions noted in the adsorbed phases on ZTC. It is possible that adding a few highly polarizable “dopant” adsorbate molecules to the adsorbed phase could enhance (or possibly sterically hinder) cooperative interactions. This could perhaps be even further investigated by adsorbing azeotropic mixtures on microporous adsorbents. However, mixed gas adsorption is also of practical interest. Natural gas is not composed of pure methane, but contains ethane and other impurities that vary by source. Thorough testing of methane/ethane, methane/carbon dioxide, or even krypton/xenon (for nuclear applications) mixed gas adsorption is vital before moving forward with engineering applications of the adsorbents.

Electron-Rich Materials

We are presently engaged in investigating hydrogen sorption on materials with nonstandard electron densities such as porous covalent electron-rich organonitridic frameworks (PECONF). These amorphous organic materials have previously been reported to have exceptional methane and carbon dioxide thermodynamics owing to their electron-rich phenyl groups. While still under investigation, we have presently noted a higher than expected hydrogen uptake. Carbonaceous adsorbents are prone to only 1 weight percent of hydrogen excess adsorption at 77K for every 500 m² of surface area. This is a well-established and rarely broken rule of thumb known as “Chahine’s Rule”. The specific surface area of PECONF was determined by applying BET theory to nitrogen adsorption isotherms measured at 77K and argon adsorption isotherms measured at 87K. The specific surface area was established as 732 m² g⁻¹. We have measured reproducible hydrogen uptake isotherms on PECONF at multiple temperatures, the highest uptake occurring at a value of 1.9 weight percent at 77K and 2.3 MPa. This yields a ratio of 1.3 weight percent of hydrogen per 500 m² g⁻¹, in excess of Chahine’s rule. The low-pressure isosteric heat of adsorption was found to be 8 kJ mol⁻¹, in agreement with the small pore size distribution for PECONF (average pore width of 5 Å). Further investigation of this material as a hydrogen adsorbent is warranted.